Alma Mater Studiorum
Università degli Studi di Bologna

Facoltà di Scienze Matematiche, Fisiche e Naturali
Dipartimento di Astronomia
DOTTORATO DI RICERCA IN ASTRONOMIA
Ciclo XXIII

THE GASEOUS ENVIRONMENT OF RADIO GALAXIES: A NEW PERSPECTIVE FROM HIGH–RESOLUTION X–RAY SPECTROSCOPY

di
ELEONORA TORRESI

Coordinatore:
Chiar.mo Prof.
LAURO MOSCARDINI

Relatore:
Chiar.mo Prof.
GIORGIO G.C. PALUMBO

Co–Relatrice:
Dr.ssa **PAOLA GRANDI**

Settore Scientifico Disciplinare: Area 02 - Scienze Fisiche
FIS/05 Astronomia e Astrofisica
Esame finale anno 2011

This thesis has been carried out at INAF/IASF-Bologna
as part of the institute research activities

Contents

List of Figures

List of Tables

Abstract

Massive galaxies appear to have a black hole at their center obeying the black hole mass and velocity dispersion correlation (M_{BH}–σ; Magorrian et al. 1998; Ferrarese & Merritt 2000; Gebhardt et al. 2000; Tremaine et al. 2002), that simply reflects the interplay between the BH and the surrounding environment. It is known that massive black holes have a profound effect on the evolution of galaxies, and possibly on their formation by regulating the amount of gas available for the star formation. However, how black hole and galaxies communicate is still an open problem, depending on how much of the energy released interacts with the circumnuclear matter. In the last years, most studies of feedback have primarily focused on AGN jet/cavity systems in the most massive, X–ray luminous galaxy clusters. This thesis intends to investigate the feedback phenomena in radio–loud AGNs from a different perspective. Indeed it presents an X–ray study of the circumnuclear environment of isolated powerful radio galaxies, through *XMM–Newton* and *Chandra* observations. In particular, the high–resolution spectroscopy technique is exploited to search for gaseous outflows in order to better understand the physical and kinematic conditions of the gas surrounding supermassive black holes.

Specifically, one Narrow Line Radio Galaxy (3C 33) and three Broad Line Radio Galaxies (3C 382, 3C 390.3 and 3C 120), are studied in detail, searching for warm photoionized gas, both in emission and absorption, in the soft X–ray band (0.3–2 keV). As a result, I found that the soft X–ray spectrum of 3C 33 could originate from gas photoionized by the central engine, rather than from the jet emerging from the edge of the torus, as previous suggested by several authors. Moreover the high–resolution spectra revealed for the first time the presence of soft X–ray warm absorbers in both 3C 382 and 3C 390.3. On the contrary, no indication of warm absorbing gas is found in 3C 120, the BLRG of the sample with the smallest inclination angle. The observed warm absorbers have column densities, ionization parameters and outflowing velocities in the range N_H=10^{20-22} cm^{-2}, logξ=2–3

erg cm s^{-1} and v_{out} $\sim 10^{2-3}$ km s^{-1}, respectively. Such values constrain the location of the gas in the Narrow Line Region, favoring a torus wind origin. The distribution of the gas is probably not uniform. The volume filling factor has to be less than 1 otherwise the absorbers mass outflow rates turn out implausibly higher than the mass accretion rates. However, even considering upper limits on the mass outflow rate, the kinetic luminosity of the outflow is always well below 1% the bolometric luminosity as well as the jet kinetic power. Finally, the radio–loud properties are compared with those of a sample of type 1 RQ AGNs taken from the literature. The physical parameters of radio galaxy warm absorbers are found to span a range of values similar to Seyferts. In addition, a positive correlation is found between the mass outflow rate/kinetic luminosity, and the radio loudness. This seems to suggest that the presence of a radio source (the jet?) affects the distribution of the absorbing gas, i.e., the volume filling factor. Alternatively, if the gas distribution is similar in Seyferts and radio galaxies, the $\dot{M}_{out}$ vs rl relation could simply indicate a major ejection of matter in the form of wind in powerful radio AGNs.

The chapters of this thesis are organized as follows:

- Chapter 1 gives an overview of the general properties of AGNs, mainly focused on radio–loud sources which are the subject of this study. Their radio, optical and X–ray spectral characteristics are fully described, and the very recent *Fermi*–LAT results on non–blazar AGNs are also reported.

- Chapter 2 provides basic physical notions necessary for the interpretation of high–resolution X–ray spectra. The atomic transitions, and in particular the radiation–driven processes are described, together with the most important line diagnostics for a photoionized gas.

- Chapter 3 presents the analysis and results obtained from the *XMM–Newton* and *Chandra* observations of the NLRG 3C 33. In particular, photoionized gas in emission is invoked to explain the soft excess in the spectrum.

- Chapter 4 describes the high–resolution analysis performed on three BLRGs. As a result, the detection of warm absorber was obtained for the first time in two of such objects.

- Chapter 5 compares the previously found properties of BLRG warm absorbers with a sample of type 1 RQ AGNs as taken from the literature. The main result is the correlation found between the mass outflow rate (and the kinetic luminosity of the outflow) and the radio loudness parameter.

- Discussions and conclusions are presented in Chapter 6.
- The Appendices report general information on the X–ray satellites used throughout this thesis.

1 Introduction

1.1 Active Galactic Nuclei

Active Galactic Nuclei (AGNs) are among the most powerful sources of electromagnetic radiation in the Universe. They produce enormous luminosities (from 10^{42} to 10^{48} erg s^{-1}) in very small volumes (probably $<<1$ pc^3).
AGNs emit their power in the overall electromagnetic spectrum, from radio to gamma–rays, forming the so called Spectral Energy Distribution, or SED (Fig.1.1), in which different processes inside and outside the active nucleus are present.

- **Radio**: radio waves have a non–thermal origin. They are emitted through synchrotron radiation produced by relativistic electrons spiraling in a magnetic field. Electrons are forced to change direction and, as a result, they are accelerated and radiate electromagnetic energy. The frequency of the emitted radiation depends on the magnetic field strength and on the energy of the electrons (see Section 1.2.2). Radio–loud AGNs are powerful radio emitters because relativistic electrons in the jets emit synchrotron radiation (see Section 1.2.2). Conversely, radio–quiet AGNs emit weak or null radio waves.

- **Infrared**: the IR band contains re–emission from hot dust nearby the active nucleus, that has been heated by the central engine. Therefore, at least around 1–40 μm, the reprocessed nuclear optical/UV/X–ray light is dominant. Three pieces of evidence support the thermal origin (Peterson 1997).
  i) The *1 μm minimum* is a general feature in the SED of AGNs (Sanders et

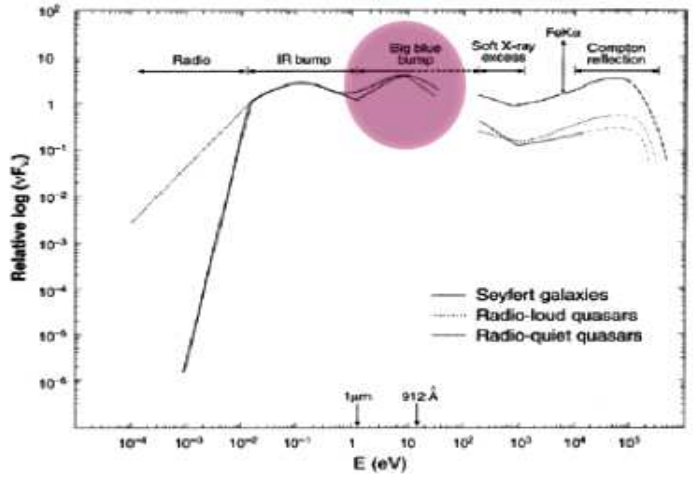

Figure 1.1 Typical SED of an AGN from radio to X–rays. The solid line represents the SED of Seyfert galaxies, the dotted line of radio–loud AGNs and finally the dashed–dot line shows the SED of radio–quiet quasars.

al. 1989). The IR emission must be thermal since the required temperatures are in the right range ($\leq$2000 K) for hot dust in the nuclear regions, while at higher temperatures dust grains sublimate.

ii) The *IR continuum variability* is a probe that the IR originates in dust far away from the central engine heated by the optical/UV radiation. The IR continuum shows the same variations as the optical/UV but with a significant time delay, meaning different distances from the nucleus.

iii) The *sub–mm break* is produced by a rapid decrease in the SED from the far–IR to longer wavelengths.

- **Optical/UV**: the optical band shows emission lines from clouds illuminated by the AGN. Broad emission lines (FWHM$\approx 10^{3-4}$ km s^{-1}) probe regions near the black hole, while narrow lines (FWHM$\approx 10^{2}$ km s^{-1}) trace larger–scale outflows. UV radiation comes from thermal plasma at 10^4–10^6 K, generating a superposition of blackbody (BB) spectra that form the "Big Blue Bump" (BBB; Fig.1.1). This excess peaks around 4000 $\AA$. Given the high absorption of the Milky Way in the EUV regime ($\nu \sim 10^{16}$ Hz) the turnover of the BBB is difficult to observe. Around 3000 $\AA$ there is a small peak, the "small blue bump", produced by the blending of Fe II iron lines together with the Balmer lines.

The following wavebands are also called *high–energy regimes*. They are of great importance to understand the AGN phenomenon and constitute the central part of this thesis.

- **X–ray**: X–rays (0.1–200 keV) account for $\sim$ 10% of the AGN bolometric luminosity. They can vary rapidly, suggesting an origin in the innermost regions of the active nucleus. The most popular model, invoked to explain these phenomena, involves accretion onto black holes, i.e. conversion of the gravitational energy of accreting material into electromagnetic radiation, as indipendently argued by Salpeter (1964) and Zeldovich (1964).
  Twenty years later, Rees (1984) theorized this phenomenon involving the accretion of matter onto a Supermassive Black Hole (SMBH), whose mass can be up to 10^9 $M_\odot$. Before accreting, the matter loses its angular momentum and forms a disk around the black hole that emits blackbody (BB) radiation in the UV band. The BB temperature decreases as the distance increases, thus the outer part of the disk, few light days across, emits in the optical regime.
  The 2–phase model of Haardt & Maraschi (1991; 1993) added the "corona" to this simple representation, in order to produce X–ray photons by Inverse Compton (IC) processes (see Section 1.2.2). The corona lies immediately above the disk (Fig.1.2) and it is composed by highly energetic thermal electrons. They boost the optical/UV photons produced by the disk up to X–ray energies. The resulting X–ray spectrum has the shape of a cutoff power law:

$$F_E \propto E^{-\Gamma(kT,\tau)} exp(-\frac{E}{E_c(kT,\tau)}) \tag{1.1}$$

  The power law is the composition of many orders of Compton scattering spectra (Fig. 1.3). A fraction of the photons of the previous scattering order undergoes another scattering amplifying the frequency, until the frequency equals the electron temperature. As photons approach the electron thermal energy, they no longer gain energy from scattering and a sharp rollover appears in the spectrum. Thus the observed high energy spectral cutoff (E_c) yields information about the temperature of the corona.($E_c \approx$kT). The relation between the spectral index and the optical depth depends on the geometry of the scattering region. The observed X–ray variability may be caused by variations in the conditions of the corona.

In detail, the typical X–ray spectrum of an AGN type 1 is shown in Fig.1.4.

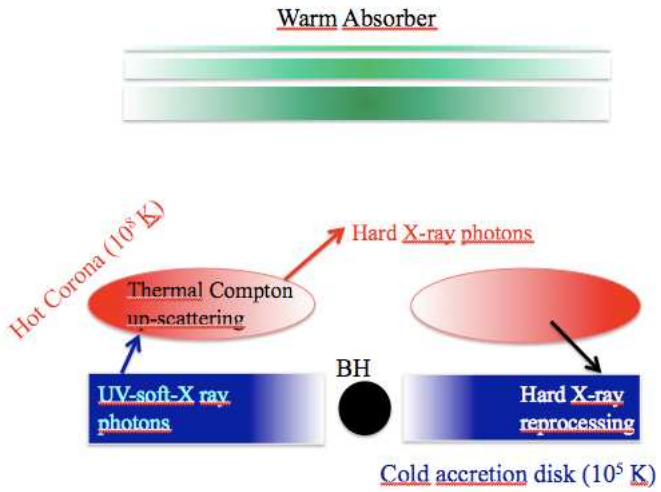

Figure 1.2 Schematic representation adapted from Haardt, Maraschi & Ghisellini (1994) of the 2–phase model. The accretion disk lies very close to the BH. It is the region where UV/soft–X–ray photons are produced. Successively, they are up–scattered by the hot corona through thermal Comptonization. In this sketch an accretion disk wind (warm absorber) is also represented.

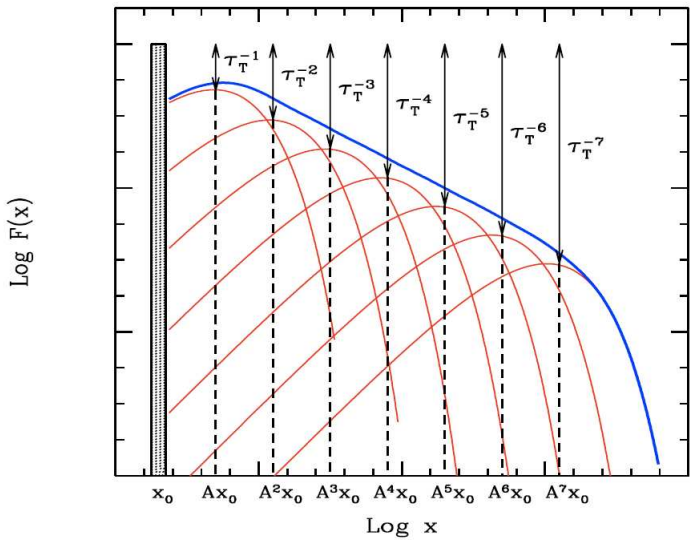

Figure 1.3 Example of a power law continuum as a result of the superposition of many orders of Compton scattering spectra. From Ghisellini lessons, September 13, 2008.

I will briefly describe the most important features.

1. The *soft excess* (E<1 keV) is observed in many AGNs and its origin is not clear. It has been argued that it is the Comptonized Wien tail of the BBB, however this seems to be unlikely because it would require $T_{BBB} \sim 2 \times 10^5$ K, too high for an accretion disk (for more details see Section 1.2.1). Moreover this component shows a fixed temperature around 0.2 keV indipendently on the BH mass. This constancy of the temperature indicates a relation between soft excess and atomic transitions (Netzer 1996; Gierlinski & Done (2004).
   An alternative interpretation of the soft excess was involves the warm absorber.
2. The *warm absorber* is a recurrent characteristic in Seyfert 1 galaxies (see Chapter 4), e.g. face–on AGNs. It is ionized gas, positioned along the line–of–sight, that absorbs the nuclear radiation, hence producing absorption lines over the soft X–ray and UV continua. It is generally characterized by a large range of ionization parameters, ξ ($\xi = \frac{L}{nR^2}$, for more details see Chapter 2), and column densities, N_H, and typically it is outflowing at velocities ranging from several hundreds to thousands km s^{-1}, depending on where this wind is launched.
3. The *Fe Kα line* is produced by fluorescence (see Chapter 2). When the lines are produced very close to the BH, they are shaped by the effects of Doppler shifts and gravitational effects (see Fig.1.5). Narrow lines can be produced in the BLR and in the torus.
4. The *reflection hump*: half of the X–rays escape from the corona and are reflected back to the accretion disk, producing the reflection component (Fig.1.4) which can give rise to the "Compton hump" peaking at 20–50 keV.

- **Gamma–rays**: γ–rays (E>100 MeV) have the smallest wavelength and the greatest energy of any other waveband. In this regime non–thermal processes dominate and it is possible to study the behaviour of some of the most energetic and extreme objects in the Universe (see also Section 1.3).
  There are several important mechanisms producing γ-rays in astrophysical objects. Among them there is the IC scattering (Fig.1.18). This process takes place when high–energy relativistic electrons scatter low energy photons to

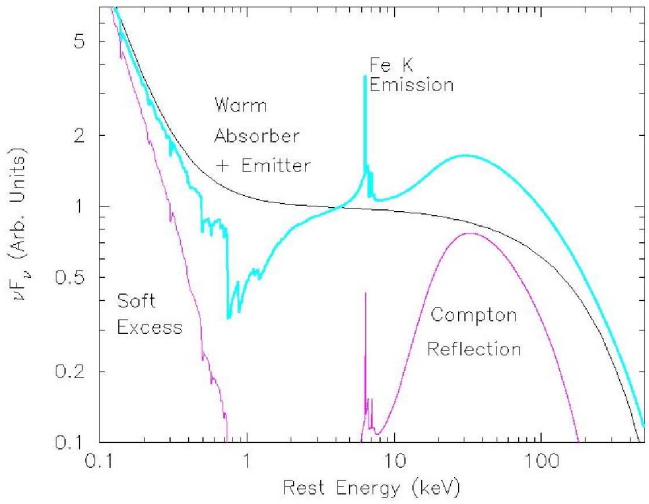

Figure 1.4 Typical Seyfert 1 X–ray spectrum in the 0.1–200 keV band.

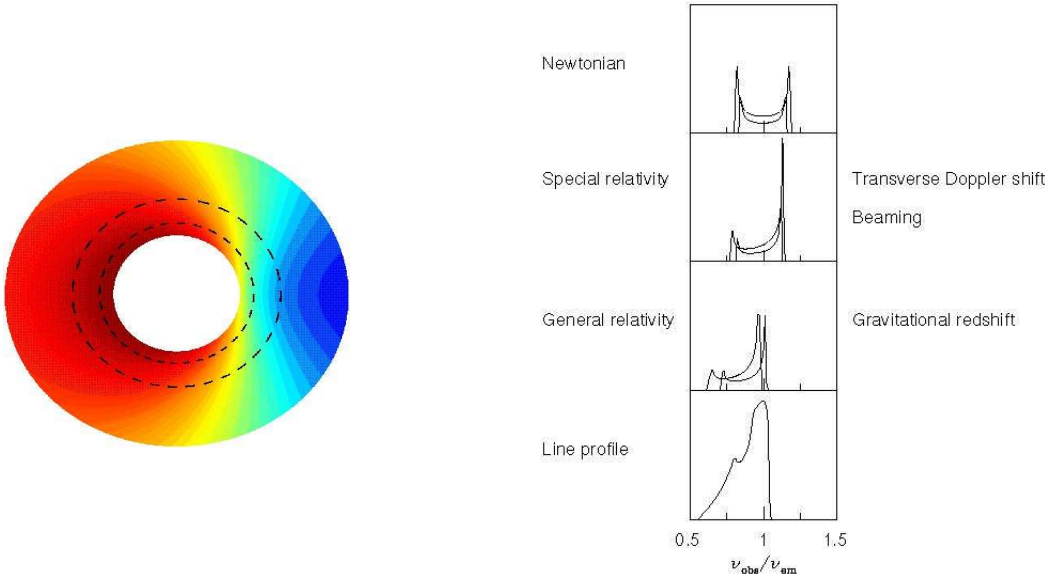

Figure 1.5 *Left panel*: symmetric double peaked profiles from two narrow annuli on a non–relativistic disk ("Newtonian" in the upper panel on the right). *Right panel*: kinematic and gravitational line distortion (from `http://nedwww.iapc.caltech.edu/level5/Fabian4/Fab2_2.html`). The Doppler shifting (second panel) and the gravitational redshift (third panel) are included. The resultant line profile (bottom panel) is broad, skewed and highly redshifted.

higher energies (e.g. in the jets). The frequency of the up–scattered photons is proportional to $\gamma_e^2\nu$ where γ_e is the Lorentz factor of the electron, and ν is the initial photon frequency.

1.1.1 AGN classification and the Unified Model

AGNs emit over the entire electromagnetic spectrum, consequently they were discovered and classified separately at different wavelenghts. Therefore the classification of AGNs is complex and employes many different methods (Tadhunter 2008) such as the presence or absence of broad emission lines in the optical spectra, the optical morphology, the radio morphology, the variability, the luminosity or the spectral shape.
Another important property is the *radio loudness*. An object is defined "radio–loud" (RL) if the ratio between the radio emission at 5 GHz and the optical flux in the B band is equal or higher than 10 (Kellermann et al. 1989):

$$\frac{F_{5GHz}}{F_B} \geq 10 \tag{1.2}$$

otherwise the object is called "radio–quiet" (RQ).
A more recent definition of *radio loudness* was introduced by Terashima & Wilson (2003):

$$R_X = \frac{\nu L_\nu(5GHz)}{L_X} \tag{1.3}$$

where L_X is the unabsorbed luminosity in the 2–10 keV band. The advantage with respect to the usual definition is that R_X can be applied to heavily obscured nuclei ($N_H \geq 10^{23}$ cm^{-2}, $A_V > 50$ mag).
Only a small fraction (15–20 %) of AGNs is RL (Urry & Padovani 1995).
RQ AGNs lie generally in spiral galaxies (Floyd et al. 2004) while RL AGNs are hosted exclusively in elliptical galaxies. Antonucci (2011) shows that, in the low–z Universe, there is a near–perfect correspondence between RL objects and elliptical hosts.

The very first classification of AGNs was made in the optical band on the basis of the presence and relative strength of emission lines. This classification can be adopted for both RL and RQ sources (Fig.1.6):

- **Type I AGNs**: they are characterized by a bright continuum and strong broad (permitted) and narrow (forbidden) emission lines. Broad lines (FWHM≈

several 10^{3-4} km s^{-1}) are produced by clouds of hot gas near the BH (<1 pc), in the *Broad Line Regions* (BLR), while the narrow lines (FWHM$\approx 10^2$ km s^{-1}) are emitted far from the BH in the *Narrow Line Regions* (NLR). RQ sources belonging to this class are Seyfert 1s and RQ QSOs, while RL sources are Broad Line Radio Galaxies (BLRG), Steep Spectrum Radio Quasars (SSRQ) and Flat Spectrum Radio Quasars (FSRQ). Few high–luminosity AGNs showing broad optical/UV absorption lines are called BAL QSOs.

- **Type II AGNs**: they show a weaker continuum and only narrow emission lines. A possible explanation for the lack of broad lines is that either the BLR are missing or, most likely, the central engine is obscured by an intervening medium, i.e. the dusty torus. RQ sources are Seyfert 2s, and RL sources are High Excitation Galaxies (HEG; Jackson & Rawlings 1997) Narrow Line Radio Galaxies (NLRG).

- **LINERs**: at the lower end of the luminosity scale there are the Low–Ionization Nuclear Emission–Line Region galaxies (Heckman, 1980) with the continuum dominated by the host galaxy. Spectroscopically they resemble Seyfert 2s, except that the low–ionization lines, (e.g., [OI]λ6300, [NII]$\lambda\lambda$6548,6583) are relatively strong. RL AGNs, similar to LINERs, are the Weak Line Radio Galaxies (WLRG), also called Low Excitation Galaxies (LEG). They are characterized by low EW (<10 $\AA$; Tadhunter et al. 1998) or [OII]/[OIII]>1 (Jackson & Rawlings 1997) and low ionization.

- **BL Lac objects**: the spectrum is dominated by non–thermal continuum emission and no, or weak, emission lines (EW<5 $\AA$) are present. Together with FSRQs, BL Lac objects form the *Blazars* class. These sources are viewed nearly along the jet axis, therefore the non–thermal jet radiation is amplified by relativistic effects giving rise to flat radio spectra, large polarization and strong variability. Blazars generally show two–peaked broad–band SEDs from radio to γ–rays. Synchrotron radiation forms the lower–energy part of the SED from radio to optical/UV. Sometimes it can extends up to the X–ray band. The Compton processes make the X–ray/γ–ray radiation. Blazars are the largest population of AGNs observed in the γ–ray sky (Hartman et al. 1999; Abdo et al. 2010a,b).

The Unified Model (Antonucci 1993; Urry & Padovani 1995) explains the variety of AGNs in terms of orientation, i.e., different AGN types all belong to the same

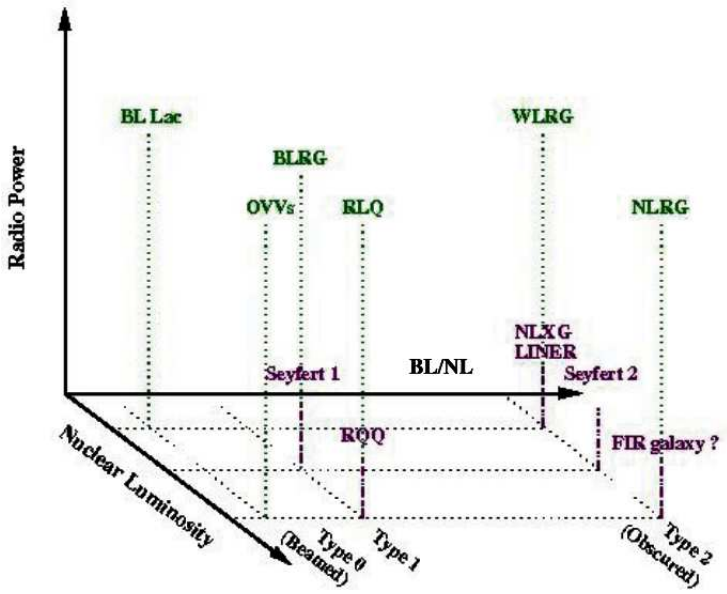

Figure 1.6 Three dimensional classification for AGNs from Tadhunter (2008). The three major divisions among the various classes are represented: the presence (absence) of broad permitted lines, AGN luminosity, radio loudness.

parent population of AGNs having similar intrinsic properties. The differences in the observed characteristics are due to anisotropy effects (Tadhunter 2008). For RQ AGNs the main cause of anisotropy is the presence of obscuring matter. Seyfert 1s are viewed face–on, the continuum is unobscured and broad emission lines are detected. Seyfert 2s are observed egde–on with the central engine obscured by the dusty torus. For RL AGNs the causes of anisotropy are two: i) the dusty torus, ii) the effect of beaming in relativistic jets (Fig.1.7). Blazars are radio sources observed close to the jet axis (low inclinations) and consequently the jet emission is strongly beamed. For larger angles of view (higher inclinations) the source is seen as a BLRG, conversely when the angle of view is quite perpendicular to the jet axis, the source appears as a NLRG.
Fig.1.8 schematically represents the Unified Model of AGNs. The black hole and the accretion disk are in the center of a wider environment. The distance scales within this environment depend upon the black hole mass, i.e., the more massive the BH, the larger the distances. Assuming an AGN with $M_{BH} \sim 10^7 M_{\odot}$, the BLR is far few light days from the nucleus (see Chapter 4).
At a distance of $\sim$1 pc away from the nucleus there is the dusty torus having a diameter of about a hundred light years. The torus is heated by the nuclear radiation and re–emits IR photons. To date this component was observed only in a handful of sources: NGC 4261 observed with HST (Jaffe et al. 1993), NGC 1068 with the VLBA at 8.6 GHz (Gallimore et al. 1997) and finally Mrk 231 (Klöckner et al. 2003) through OH maser emission.
Hundreds of light years away from the central engine there is the NLR. Its clouds are less dense than BLR (n$\sim 10^{3-6}$ cm^{-3}) and can form ionization cones extending up to kpc distances.

As pointed out by Tadhunter (2008), the orientation–based unified models are highly successfull in explaining some aspects of the AGN classification, particularly the relationship between narrow and broad line AGNs. However, much is still unexplained such as the RL/RQ dichotomy. Why RL sources contain relativistic jets which are missing or very weak in RQ objects, is yet an unanswered question.

1.1.2 Radio galaxies

The main structural components of a radio galaxy are (see Fig.1.9):

- **The core**: compact region with flat radio spectrum ($\alpha \sim 0$). It is still very difficult resolve the central even with a 10 mas VLBI resolution.

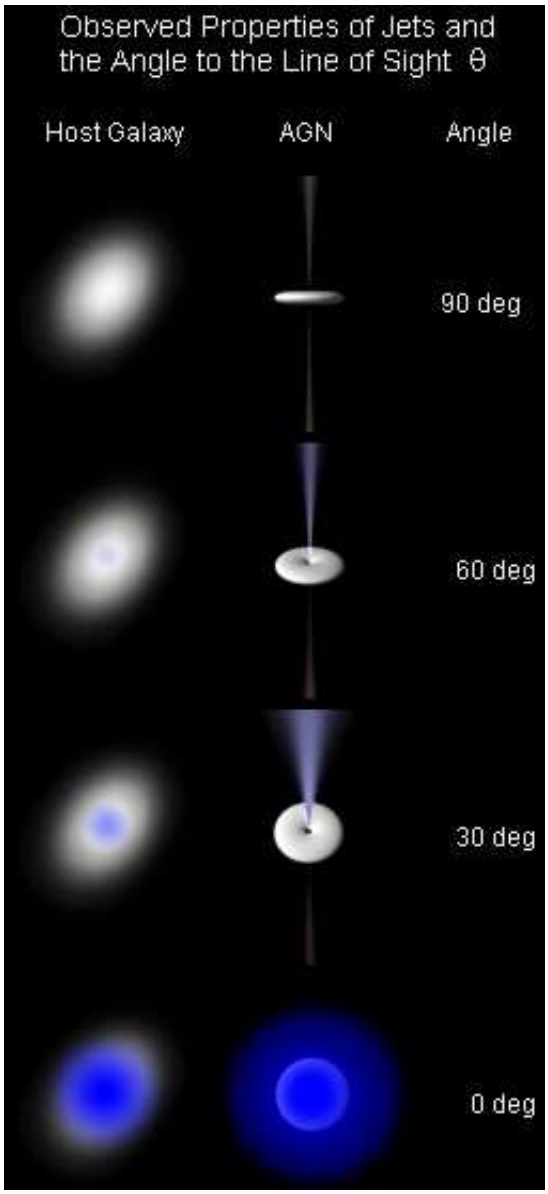

Figure 1.7 The causes of anisotropy in a RL AGN are two, the torus and the jet. As shown in this sketch, the relative disk–jet strength depends on the viewing angle. When the jet is pointing at large angles ($\theta \geq 45°$) with respect to the observer line–of–sight, the disk is completely hidden by the circumnuclear torus and the object is classified as NLRG. If the jet is pointing closer to the line–of–sight, the AGN becomes directly visible and it is classified as quasar or as BLRG. At even smaller angles the AGN spectrum is dominated by the inner jet emission, and the object is classified as a FSRQ. The left column shows how the host galaxy appears for different inclination angles of the jet.

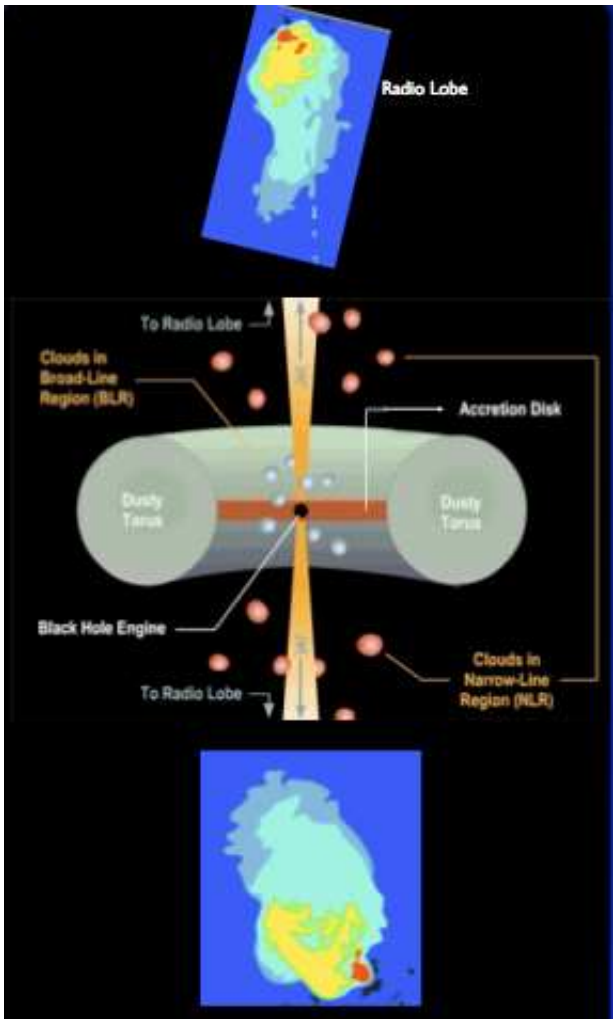

Figure 1.8 Schematic representation of the Unified Model of AGNs. The black hole is surrounded by a luminous accretion disk, and the broad line region clouds enclosed within the dusty torus. The NLR is outside the torus, farther from the central source than BLR. The radio jet travels along the axis of the system until it impacts with the IGM and feeds particles and magnetic energy into the radio lobes (from `www.astronomyonline.org`).

- **The jets**: collimated outflows of relativistic plasma that originate in the central region of the AGN and reach kpc or even Mpc distances. In the radio band jets emit synchrotron radiation, and the resultant spectrum is a power law, $S_\nu \propto \nu^{-\alpha}$, with $\alpha \sim 0.6$ (Muxlow & Garrington 1991). Jets are also visible in the optical and X–ray bands (Harris & Krawczynski 2006). At high energies the involved physical processes are synchrotron or inverse Compton. For more details see Section 1.2.2.

- **The hot–spots**: bright compact regions located at the end of the jets. They are produced when the jet impacts the ISM generating shocks. The X–ray emission from the hot–spots of several radio sources, for example Cygnus A, conform to a Synchrotron Self–Compton (SSC) model (see section 1.2.2) with a magnetic field close to equipartition [1] (Wilson et al. 2001). However in other cases, for example Pictor A, the X–ray emission cannot be explained by SSC model (Wilson et al. 2001), unless relaxing the equipartition condition.

- **The lobes**: extended structures lying in opposite directions, reaching even Mpc distances from the nucleus. They are filled with plasma passed along the jet and through the hot–spots. The radiation emitted by lobes has non–thermal origin. Specifically, the radio emission is due to synchrotron, while in the X–ray band the emission process is usually Inverse Compton scattering of the microwave background radiation (CMB; Kataoka & Stawarz 2005; Migliori et al. 2007). Very recently γ–ray emission from the lobes of the radio galaxy Centaurus A has been discovered by the *Fermi* collaboration (Abdo et al. 2010d).

Radio galaxies have been historically classified by Fanaroff & Riley (1974) in FR type I and II, depending on their extended radio morphology that changes over, or under, a critical radio power at 178 MHz, $P_{178\ MHz} \sim 10^{25}\ W\ Hz^{-1}\ sr^{-1}$.

- **FRI** are weak radio sources, characterized by turbulent decelerating jets and kpc scale relaxed lobes (Fig.1.10 *left panel*). Their host galaxies are generally brighter than those of FRIIs, and are usually found at the centre of clusters (Prestage & Peacock 1988) and have a dominant cD morphology. Their optical spectra show weak emission lines.

[1] The minimum energy or equipartition is given when the energies are nearly equally distributed between relativistic particles and the magnetic field.

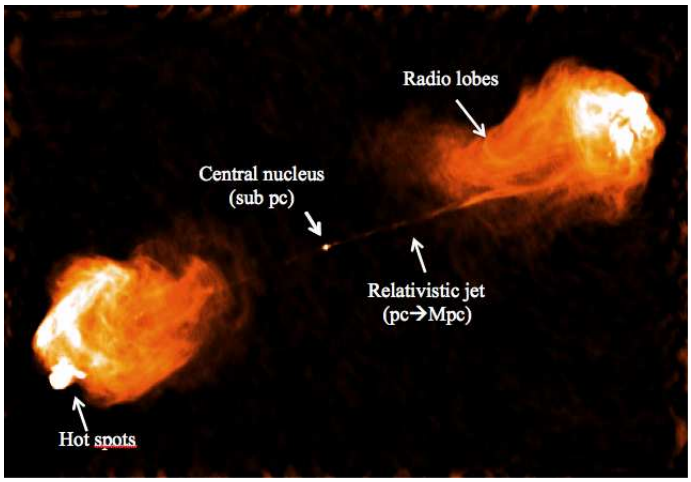

Figure 1.9 Radio image at 6 cm of the powerful radio galaxy Cygnus A (3C 405) from Perley et al. (1984). The structural components described in the text are reported.

- **FRII** or "classical double" are bright radio sources with relativistic jets, edge–brightened lobes and bright hot–spots far from the nucleus (Fig.1.10 *right panel*). FRII hosts are generally isolated (Prestage & Peacock 1988) and avoid cD galaxies. Their optical spectra usually show strong emission lines.

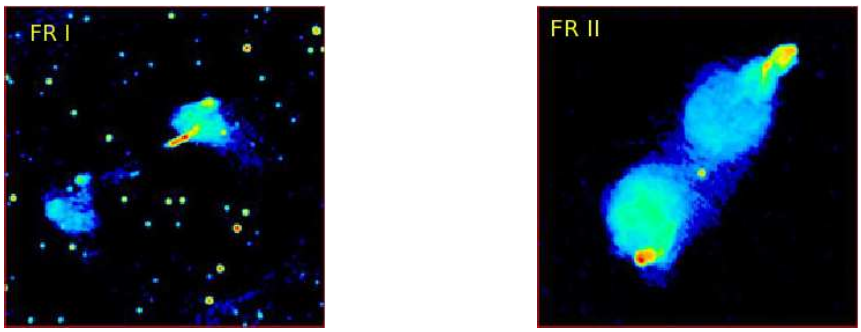

Figure 1.10 *Left panel*: the FRI radio galaxy NGC 6251. *Right panel*: the FRII 3C 390.3. The different morphologies are evident.

Two accredited hypothesis try to explain the different radio morphology of FRIs and FRIIs: 1) the interplay between the jet energy and the density of the environment; in this scenario FRIs and FRIIs are different manifestations of the same phenomenon. 2) Different accretion modes onto the SMBH; for FRIIs a standard Shakura & Sunyaev (1973) radiatively efficient accretion disk is invoked (see Section 1.4), instead for FRIs low accretion rates and low radiation efficiencies (ADAF, ADIOS,...) are proposed. The transition from FRIs to FRIIs would be due to a change in the accretion mode and can be related to an evolutionary scenario (Ghisellini & Celotti 2001; Marchesini et al. 2004). It is possible that all AGNs pass through a jet phase (FRII), then when the accreted gas is exhausted the AGN turns into low–power FRIIs and successively FRIs.
In a very recent review, Antonucci (2011) divides radio galaxies in *thermal* and *non–thermal* sources depending on their accretion modes. Thermal RGs contain hidden (by the torus) quasar nuclei, while non–thermal ones are weakly accreting galaxies (but powerful synchrotron emitters) characterized by weak low–ionization lines.

Besides FRIs and FRIIs, there is also another class of objects, the *Compact Sources*, that are powerful radio emitters peaking at MHz–GHz frequencies. They are very small, generally in the size range 1–20 kpc, i.e., smaller than typical host galaxies. To date there are two possible explanations for their compactness: i) they are young AGNs in expansion through interactions with the ISM, and this is supported by estimates on the jets ages around 10^4–10^6 yr through VLBI proper motions (Giroletti 2008); ii) they are frustated AGNs confined by the ISM and so not evolved in full–size AGNs. However, this latter scenario is less plausible since the densities and properties of the surrounding gas are comparable with those in extended AGNs (O'Dea 1998). There are two main types of compact sources: the Compact Steep–Spectrum (CSS) sources and the Gigahertz Peaked Spectrum (GPS) sources. CSS are miniature classical double radio galaxies with more pronounced asymmetries. They are extended on kpc scales with an estimated age around 10^6 yr and have steep spectra ($\alpha > 0.5$). GPS are powerful radio sources, peaking at GHz frequencies (smaller galaxies peak at higher frequencies). They are smaller than CSS, infact their extension is contained within the NLR ($\leq$1 pc).
Finally, RL quasars are subdivided into two different groups depending if they are steep radio spectrum dominated (SSRQs, $\alpha_r > 0.5$) or flat radio spectrum dominated (FSRQs, $\alpha_r > 0.5$). SSRQs tend to have lobe–dominated radio morphologies, while

FSRQs often have core–dominated radio structures and are highly variable.

1.2 Accretion and jet link

A common characteristic that is shared by all radio–loud AGNs is the presence of two competitive components, the disk and the jet, which are usually mixed when arrive to the observer. Although in some cases one component dominates over the other one (e.g., in Blazars the jet radiation is dominant), generally the resultant spectrum is a combination of both and the challenge is to distinguish between them.

1.2.1 Accretion

Black holes aggregate matter from their surroundings through accretion. The efficiency of this process is measured in terms of the released luminosity

$$L_{acc} = \eta \dot{M} c^2 \tag{1.4}$$

where η is the efficiency of conversion of the rest mass energy of the accreting material into radiation, and $\dot{M}$ is the accretion rate in $M_\odot$ yr^{-1}.
Differently from other astrophysical objects like the stars, accreted matter falling into the black hole after crossing the Schwarschild radius (or event horizon) [2] cannot escape anymore (Fig.1.11). The Schwarschild radius is defined as:

$$R_S = \frac{2GM}{c^2} \sim 3 \times 10^{13}\ M_8 \text{ cm} \tag{1.5}$$

Another important quantity that must be considered when dealing with AGNs, is the Eddington luminosity (L_E). L_E is the luminosity at which the outward force of the radiation pressure is balanced by the inward gravitational force:

$$L_E = \frac{4\pi G m_p c M}{\sigma T} \sim 1.3 \times 10^{38} (M/M_\odot) \text{ erg s}^{-1} \tag{1.6}$$

Accretion processes involve rotating gas flow. To determine the accretion flow structure is necessary to solve simultaneously four conservative equations:

[2] According to the Penrose process it is possible to extract energy from a rotating BH because the rotational energy of the BH is located outside the event horizon, precisely in the ergosphere. In the process, the BH loses part of its angular momentum that is converted into exctracted energy.

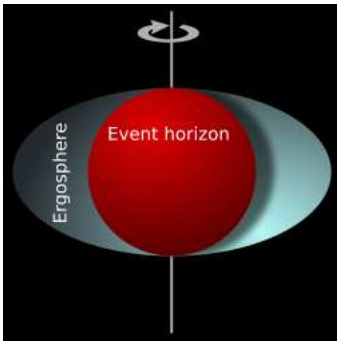

Figure 1.11 Schematic representation of a rotating black hole with the two relevant surfaces: the spherical event horizon and the oblate ergosphere. Within the ergosphere the spacetime is dragged along in the direction of the BH rotation at a speed greater than the speed of light. Since the ergosphere is located outside the event horizon, the Penrose process theorized that it is still possible to exctract energy from a rotating BH.

1. conservation of vertical momentum
2. conservation of mass
3. conservation of energy
4. conservation of angular momentum

There are four different solutions to these equations and consequently four models. The most famous are: the Shakura & Sunyaev (1973) geometrically thin optically thick accretion disk, or the standard model, and the optically thick advection dominated accretion flow, or ADAF (Ichimaru 1977; Narayan & Yi 1994; 1995; Abramowicz et al. 1995). Both solutions invoke viscosity as the source of heat that is radiated away. It transports angular momentum outward allowing the accretion gas to spiral toward the black hole.

- In the standard model (Shakura & Sunyaev 1973) the local emission of the disk can be approximated to a blackbody. The effective temperature (T_{eff}) of the photosphere is:

$$T_{eff}(r) \sim 6.3 \times 10^{-5} (\frac{\dot{M}}{\dot{M}_E})^{1/4} M_8^{-1/4} (\frac{r}{R_S})^{-3/4} \mathrm{K} \tag{1.7}$$

For an AGN with M_{BH}=10^8 $M_\odot$, T_{eff} is in the range 10^5–10^7 K and the peak occurs at UV–soft–X–ray region (the Big Blue Bump), ν_{max}=2.8kT/h$\sim 10^{16}$ Hz.

- In the advection dominated accretion flow solution (ADAF), the accreting gas has a very low density and is unable to efficiently cool. The viscous energy is stored in the gas and advected onto the black hole instead of being radiated as in the previous model (Fig.1.12). As a consequence, ADAF is very hot, T_i $\sim 10^{12}$ K (R_S/R) and T_e $\sim 10^{9-11}$ K, geometrically–thick but optically–thin (low density). The ADAF spectrum extends from $\sim 10^9$ Hz to $\geq 10^{23}$ Hz (Fig.1.13): radio to X–ray band radiation is produced through synchrotron, bremmstrahlung and Inverse Compton, while γ–rays are produced by pion decay after proton–proton collisions (Mahadevan, Narayan & Krolik 1997). The ADAF solution exists only for $\dot{M}/\dot{M}_E$ [3] less than a critical value $\dot{M}_{crit} < \alpha^2$, where α is the viscosity parameter. ADAF is a simple solution, however accretion flows are probably more complex, for this reason other models have been proposed. Among them we mention the Advection Dominated Inflow–Outflow solution, ADIOS (Blanford & Begelman (1999); Fig.1.14) and the radiatively inefficient accretion flow (RIAF) plus truncated disk (Ho 2008 and references therein; Fig.1.15).

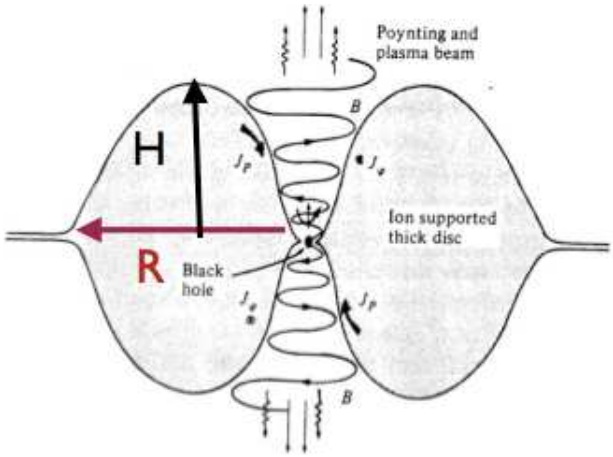

Figure 1.12 Schematic representation of the ADAF solution. The accreting gas has a very low density and is unable to cool efficiently. The viscous energy is stored in the gas as thermal energy instead of being radiated and is advected onto the BH.

[3] $\dot{M}_E$=$L_E/\eta c^2$ is the Eddington mass.

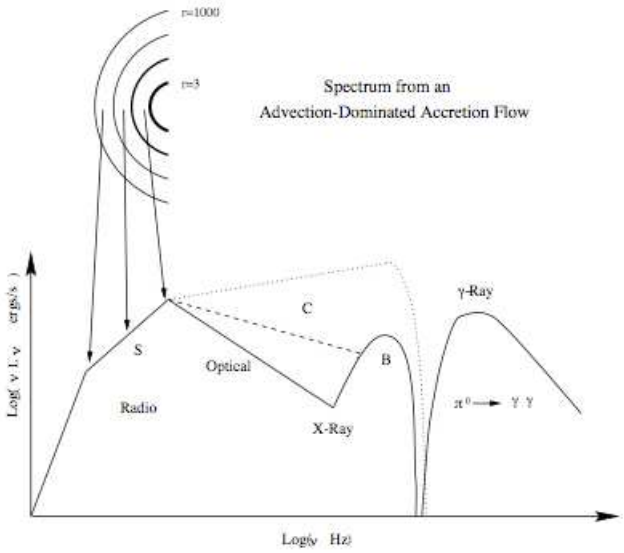

Figure 1.13 Typical ADAF spectrum: radio to X–rays radiation is produced through synchrotron, bremsstrahlung and IC. γ–rays are produced by pion decay after proton–proton collisions.

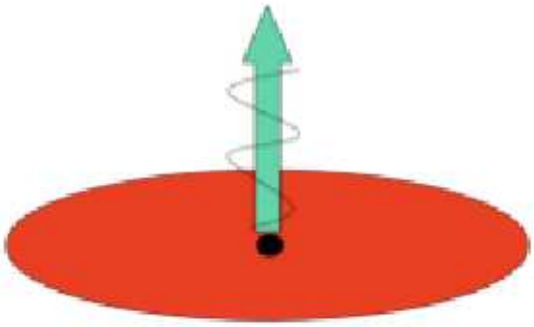

Figure 1.14 In the ADIOS solution only a small fraction of the gas falls onto the black hole. The binding energy released is transported radially outward by the torque and the remainder of the energy is driven away in the form of a wind or jet.

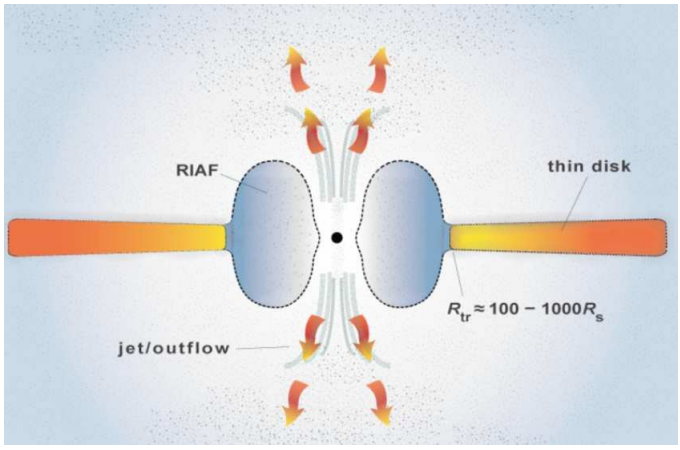

Figure 1.15 Cartoon of the central engine of an AGN with radiatively inefficient accretion flow (RIAF), a truncated accretion disk and a jet or ouflow (from Ho 2008).

1.2.2 Jets

Many of the following equations and figures are taken from Urry & Padovani (1995) and references therein.

Jets are giant plasma outflows through which the black hole tranfers huge amount of energy, momentum and angular momentum at very large distances to the environment. A key parameter to study jets is the Doppler factor:

$$\delta = [\gamma(1 - \beta cos\theta)]^{-1} \tag{1.8}$$

where $\beta = \frac{v}{c}$ is the bulk velocity, $\gamma = (1 - \beta^2)^{-1/2}$ is the Lorentz factor and θ is the angle between the jet axis and the line of sight. The Doppler factor relates intrinsic and observed flux for a moving source at relativistic speed v=βc. It stronlgy depends on the angle of view, and increases as the Lorentz factor increases (Fig.1.16). When θ=0° $\rightarrow$ δ_{max}=(1+β)γ $\sim$2γ for $\gamma \gg$1, the observer will see a superluminal source, i.e, the apparent velocity is greater than the speed of light. When θ=90° $\rightarrow$ δ_{min}=γ^{-1}, the source appears as a classical double.

The evaluation of the amplification factor can be affected by several assumptions, all included in the single parameter ρ. For example, the observed luminosity, L_j, of a relativistic jet is related to its intrinsic luminosity, L_j, via the relation:

$$L_j = \delta^{\rho} L_j \tag{1.9}$$

the exponent of the Doppler factor ρ can be set ρ=3+α if we consider a moving isotropic source, or ρ=2+α if a continuous jet is taken into account (Urry & Padovani 1995).

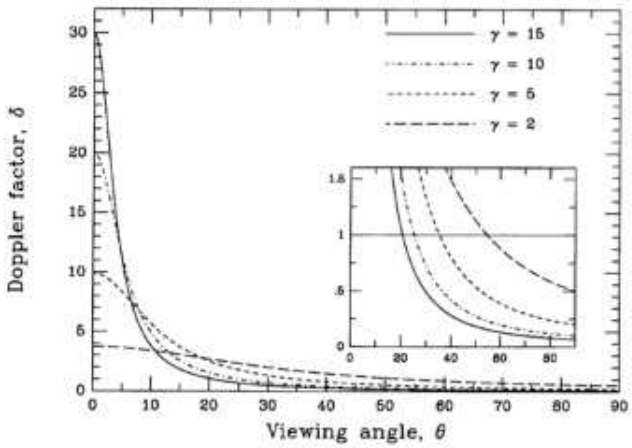

Figure 1.16 Dependence of the Doppler factor on the angle to the line of sight (from Urry & Padovani 1995). Different curves correspond to different Lorentz factors. In the expanded scale angles for which δ=1 are shown.

1.2.3 Physical processes in jets

Jets emit non–thermal radiation principally through synchrotron and Inverse Compton physical processes. In Section 1.1 it was already mentioned that synchrotron radiation is produced by relativistic electrons spiraling in a magnetic field (Fig.1.17). Assuming a power law energy distribution for the relativistic electrons:

$$N(\gamma_e) = K\gamma_e^{-p} = N(E)\frac{dE}{d\gamma} \tag{1.10}$$

for $\gamma_{min} < \gamma_e < \gamma_{max}$ and p=1+2α.

If the above equation represents a density, to obtain the emissivity (i.e., the power per unit solid angle produced within 1 cm^3), N(γ) times the power produced by a single electron of a given γ, P(γ, ν, θ), should be integrated over γ and divided for 4π (if the emission is isotropic). As a result, the emissivity in an approximate

range of frequencies is obtained:

$$\epsilon_{sin}(\nu) \propto K B^{\alpha+1} \nu^{-\alpha} \text{ [erg cm}^{-3} \text{ s}^{-1} \text{ sr}^{-1}\text{]} \tag{1.11}$$

Notice that the value p=1+2α derives from the fact that a power law electron distribution produces a power law spectrum and the two spectral indices (α and p) are related (Rybicki & Lightman 1979).

Inverse Compton (IC) generates when the electron energy is greater than the photon one, and a transfer of energy from the electron to the photon can occurr (Fig.1.18). There is a strong link between the scattered frequency ν_c and the electron energy producing it:

$$\nu_c = \frac{4}{3}\gamma^2 \nu_0 \tag{1.12}$$

The IC emissivity (ϵ_c) can be deduced in the same way of the synchrotron emissivity (ϵ_{sin}) assuming a power law distribution for the relativistic electrons (eq. 1.9). It is possible to derive the emissivity that is again a power law, with the same link between α and p, α=(p-1)/2:

$$\epsilon_c(\nu_c) \propto K \nu_c^{-\alpha} \int \frac{U_r(\nu)\nu^{\alpha}}{\nu} d\nu \text{ [erg cm}^{-3} \text{ s}^{-1} \text{ sr}^{-1}\text{]} \tag{1.13}$$

where $U_r(\nu)$ is the specific radiation energy density describing the upscattered photon field. When the same electrons producing synchrotron radiation are scattered, the resultant process is called *Synchrotron–Self Compton* (SSC), while when the scattered ($U_r(\nu) \propto \nu^{-\alpha}$) photons come from external regions like the disk or the BLR, the torus, the NLR, the process is called *External Compton (EC)*. The Cosmic Microwave Background (CMB) can be also the "seed" photons for the IC in jets or lobes.

1.2.4 Jet orientation

The jet inclination angle is a fundamental (but difficult to constrain) parameter to understand the physical properties of relativistic sources. It can be estimated by different observational quantities:

- the jet/counterjet ratio, J=$(\frac{1+\beta cos\theta}{1-\beta cos\theta})^{\rho}$, again ρ=2+α for a continuous jet, and ρ=3+α if a moving isotropic source is adopted;

- the VLBI apparent velocity $\beta_a = v_a c$ of the jet knots that is related to β and

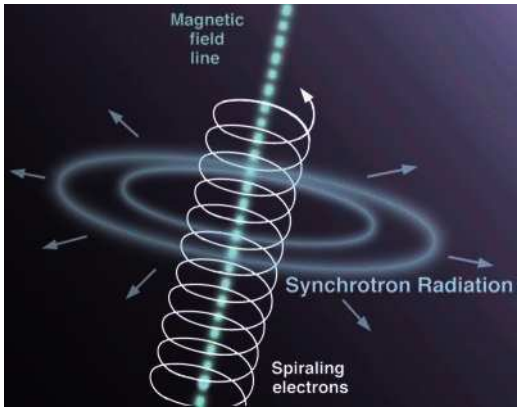

Figure 1.17 Schematic representation of the synchrotron physical process.

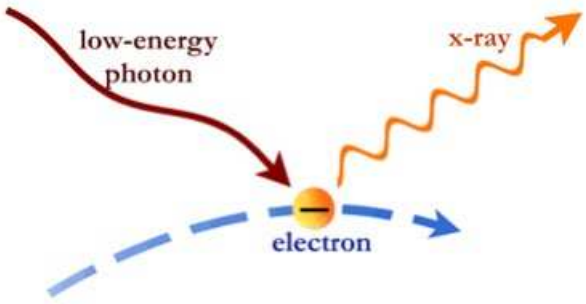

Figure 1.18 Representation of the Inverse Compton process.

θ via $\beta_a = \frac{\beta sin\theta}{1-\beta cos\theta}$ (Urry & Padovani 1995);

- the general correlation between the radio core power at 5 GHz (P_c) and the total power (P_{tot}) at 408 MHz in radio galaxies found by Giovannini et al. (1988; 2001). This relation LogP_c= 0.62 LogP_{tot}+7.6 (i), obtained using a large sample of radio galaxies selected at low frequency and therefore with jet directions uniformly distributed in the space, corresponds to the average orientation angle (60°) with respect to the line–of–sight. Considering that the radio core power of a source oriented at an angle θ is amplified by a quantity P_c=P_i (1-β cos θ)$^{-(2+\alpha)}$ (ii), where P_i is the intrinsic power and α is the core radio spectral index , combining (i) and (ii) can be easily derived the relation $\beta = \frac{(k-1)}{(kcos\theta-0.5)}$ that allows to directly express β as a function of θ;

- a less robust but useful indicator of the jet orientation is the core dominance CD=Log($\frac{S_{core}}{S_{tot}-S_{core}}$) (Scheuer & Readhead 1979), where S_{core} (S_{tot}) is the core (total) flux density referred to the source rest–frame.

1.3 Radio Loud AGNs in the Fermi era

The γ–ray satellite *Fermi*, launched on June 2008, has shown that non–blazar (i.e. misaligned) AGNs can be GeV emitters. With the term misaligned AGNs (MAGNs) we define radio–loud sources whose jet is pointed away from the observer, i.e., without strong Doppler boosting, with steep radio spectra (α_r >0.5) and resolved and possibly symmetrical radio structures. Given the large inclination angle of the jet, MAGNs were not considered possible GeV emitters, but the *Fermi Large Area Telescope* (LAT; Atwood et al. 2009) detection of 11 MAGNs in 15 months has changed this view and confirmed MAGNs as a new an interesting class of γ–ray emitters. Note that three MAGNs have been also discovered in the TeV band: M87 (Aharonian et al. 2003), Centaurus A (Aharonian et al. 2009), NGC 1275 (Mariotti et a. 2010). In this part of the thesis I briefly report on the recent *Fermi* results decscribed in the papers Abdo et al. (2010c; Contact authors: P. Grandi, G. Malaguti, G. Tosti, C. Monte) and Migliori, Grandi, Torresi et al. (2011). I was involved in these works as an affiliated member of the *Fermi–LAT* collaboration.

1.3.1 Misaligned AGNs as a new class of GeV emitters

In 15 months, the *Fermi* LAT telescope could detect 11 MAGNs, all belonging to the flux limited catalogues 3CR (Bennett 1962; Spinrad et al. 1985), 3CRR (Laing et al. 1983) and the Molonglo Southern 4 Jy sample (MS4; Burgess & Hunstead 2006a,b).

Spectral analysis

For each source the LAT data collected from August 4, 2008 to November 8, 2009 were analyzed using the standard *Fermi–LAT Science Tools* software package. The spectral study was performed using the unbinned maximum–likelihood analysis in the *gtlike* tool which provides the best–fit parameters for each source.
The likelihood L is the probability of obtaining the observed data given an input model (i.e. the distribution of gamma–ray sources on the sky together with their intensity and spectra). L will be maximized to get the best match of the model to the data. Every set of data can be binned in multidimensional bins. The observed number of counts in each bin is characterized by the Poisson distribution, thus L is the product of the probabilities of observing the detected counts in each bin, n_k, while m_k counts are predicted by the model:

$$L = \prod_k \frac{m_k^{nk} e^{-m_k}}{n_k!} \tag{1.14}$$

that can be rewritten as:

$$L = e^{-N_{pred}} \prod_k \frac{m_k^{nk}}{n_k!} \tag{1.15}$$

The *unbinned likelihood* is obtained when the bin sizes get infinitesimally small, n_k=0 or 1, and consequently it remains the product running over the number of photons:

$$L = e^{-N_{pred}} \prod_i m_i \tag{1.16}$$

or

$$LogL = \sum_i (m_i) - N_{pred} \tag{1.17}$$

The significance of each source is given by the test statistic (TS), that is defined as:

$$TS = -2log(\frac{L_{max,0}}{L_{max,1}}) \tag{1.18}$$

where $L_{max,0}$ is the maximum likelihood value for a model without an additional source ("null hypothesis") and $L_{max,1}$ is the maximum likelihood value for a model with the additional source at a specified location. For a large number of counts, TS for the null hypothesis is asymptotically distributed as χ^2_n (n being the number of parameters characterizing the source). Basically, the square root of the TS can be considered equal to the detection significance for a given source. When TS$\leq$10, the flux values at F>100 MeV are replaced by 2σ upper limits. These upper limits are derived by finding the point at which 2Δlog(likelihood)=4 when increasing the flux from the maximum–likelihood value. All the sources of the MAGN sample have TS>30, implying $\geq 5\sigma$ detection.

Time variability

For our sources the likelihood analysis was performed on the entire 0.1–100 GeV energy band. Time variability was also searched for each MAGN. In order to generate the light curve of each source, the total observation period was divided into 15 and 5 time intervals of 1 month and 3 months duration, respectively. The likelihood analysis was repeated for each interval keeping the spectral index fixed to the best–fit value. A standard χ^2 test was applied to the average flux in each light curve. A source is variable if the probability that its flux is constant is less than 10^{-3}. No evidence for time variability is found for any sources with the exception of NGC 1275 that shows variability on timescale of months (Fig.1.19). However, given the low γ–ray fluxes for 7 out of 11 MAGNs, variability could also not be measured even when present.

Results

Table 1.1 summarizes the results of the Fermi–LAT analysis. Seven out of eleven LAT sources have spectral indices softer than 2.3 (most of the photon energies lie between 100 MeV and 10 GeV). 3C 120 is the softest case, emission is detected only in the 100 MeV–1 GeV energy band. As shown in the count map of 3C 120 (Fig.1.20), this source can be contaminated by the nearby FSRQ 1FGLJ0427.5+0515. However the two sources are 1.4° apart and, if there is an effect, it is negligible. 3C 78 and

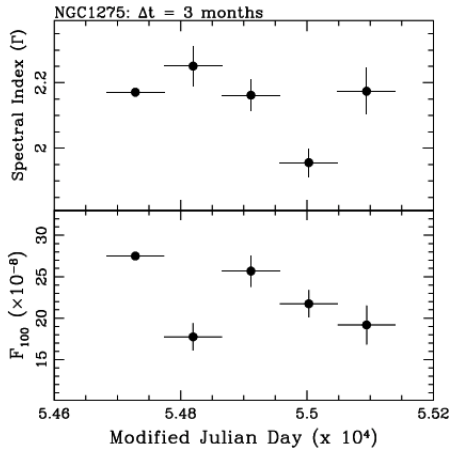

Figure 1.19 Flux and spectral slope variations of NGC 1275. Each bin corresponds to 3 months of observations in the 100 MeV–100 GeV energy band.

PKS0625–34 are the only two FRIs not detected at energies ≤300 MeV and are the weaker sources of the sample.

The comparison of MAGN results along with the corresponding values for FSRQs and BL Lacs is shown in Fig.1.21, where the spectral slope Γ is plotted against the 100 MeV–10 GeV γ–ray luminosity L_γ. MAGNs and Blazars occupy different regions of the plot, with MAGNs generally characterized by lower luminosity. This is in agreement with the unified scenarios as jets that are not directly pointed towards the observer are expected to be fainter as a consequence of the smaller Doppler

Table 1.1 The MAGN Sample

Object	Redshift	Class Radio/Optical	Log (CD) at 5GHz	TS	Γ	Flux[a] (>100MeV)	LogLum[b] (0.1-10 GeV)
3C 78/NGC 1218	0.029	FRI/G	-0.45	35	1.95±0.14	4.8±1.8	42.84
3C 84/NGC 1275	0.018	FRI/G	-0.19	4802	2.13± 0.02	222 ±8	44.00
3C 111	0.049	FRII/BLRG	-0.3	34	2.54 ±0.19	40 ±8	44.00
3C 120	0.033	FRI/BLRG	-0.15	32	2.71±0.35	29 ±17	43.43
PKS 0625-354	0.055	FRI/G	-0.42	97	2.06±0.16	4.8±1.1	43.7
3C 207	0.681	FRII/SSRQ	-0.35	79	2.42 ±0.10	24 ±4	46.44
PKS 0943-76	0.27	FRII/G	< -0.56	65	2.83 ± 0.16	55 ±12	45.71
M87/3C 274	0.004	FRI/G	-1.32	194	2.21 ± 0.14	24 ± 6	41.67
CENA	0.0009	FRI/G	-0.95	1010	2.75± 0.04	214 ±12	41.13
NGC 6251	0.024	FRI/G	-0.47	143	2.52 ±0.12	36 ±8	43.30
3C 380	0.692	FRII/CSS/SSRQ	-0.02	95	2.51 ±0.30	31 ±18	46.57

(a) - 10^{-9} Phot cm^{-2} s^{-1}

(b) - erg s^{-1}

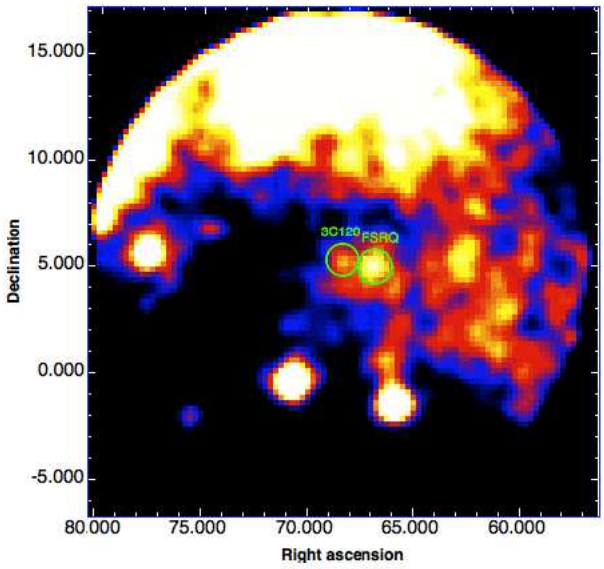

Figure 1.20 3C 120 count sky map between 100 MeV and 100 GeV

boosting. This plot shows a well defined separation between FRIs and BL Lacs, their putative parent population, with FRIs significantly less luminous than BL Lacs, while FRIIs lying in the outskirts of FSRQs distribution could possibly reflect different beaming factors for the γ–ray emission.

The core dominance (CD; see Section 1.2.3) study of the 3CRR sample as a function of the total flux at 178 MHz (Fig.1.22) indicates that *Fermi* preferentially detects radio sources intermediate between blazars and radio galaxies with large CD values and small inclination angles. FRIs with large inclination angles and small CDs are observed only if nearby. MAGNs at larger distances have larger CD values. Therefore the small number of FRIIs detected with the LAT, in comparison to FRIs, could be due to the fewer nearby FRIIs, or to different jet structures.

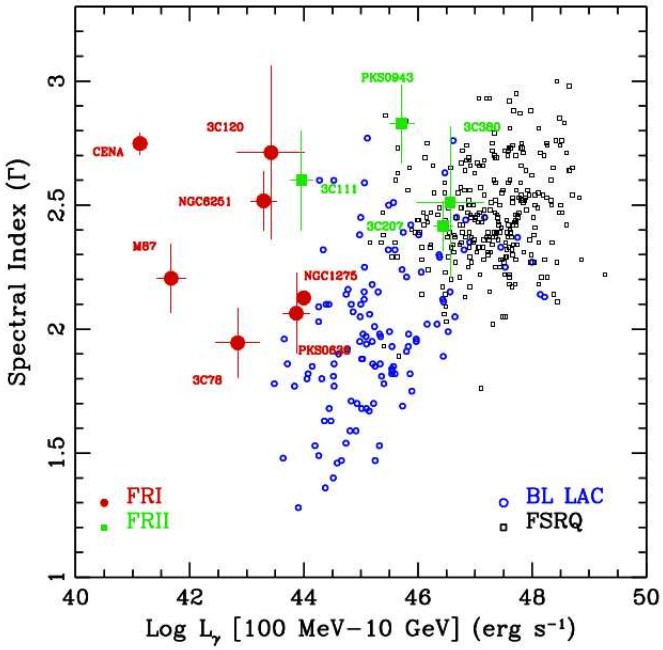

Figure 1.21 The spectral slopes of FRI radio galaxies (*red circles*), FRII radio sources (*green squares*), BL Lacs (*open blue circles*) and FSRQs (*open black squares*) are plotted as a function of the γ–ray luminosity (100 MeV–10 GeV). MAGNs and Blazars occupy different regions of the plot, instead the two more distant SSRQs fall within the range of FSRQs γ–ray luminosities.

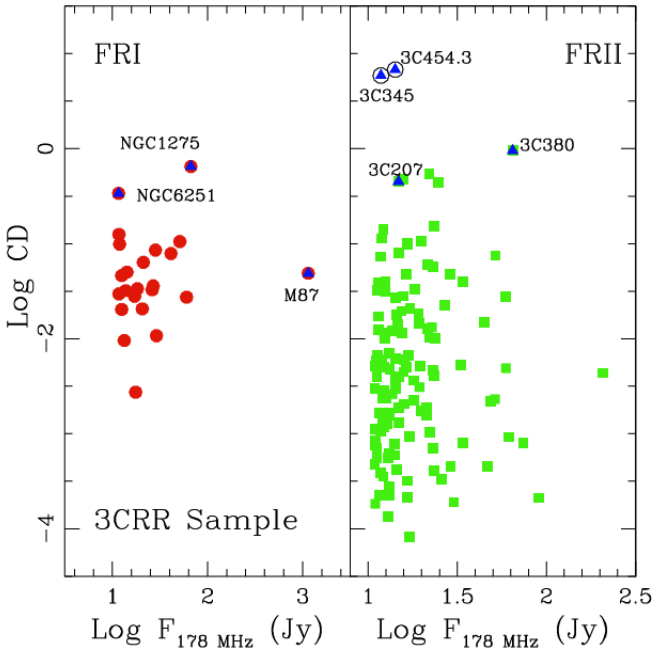

Figure 1.22 Core dominance plotted against the total flux at 178 MHz of all the sources of the 3CRR sample: *red circles* represent FRIs and *green squares* FRIIs. The *blue triangles in circles/squares* are the MAGNs detected by *Fermi* and are characterized by large CD values. The *blue triangles in empty black circles* are the two FSRQs detected by LAT and have much larger CDs than MAGNs.

1.3.2 The jet structure of NGC 6251

The successive step, after having defined the MAGN sample, was to study in detail one of the brightest radio galaxy in the sample: the FRI NGC 6251. In Migliori et al. (2011) the study of the SED of the core is presented and the one zone synchrotron/SSC framework is explored.

NGC 6251 is a luminous FRI, the fifth–brightest among the MAGNs, located at z=0.0247. As other sources of the sample (Cen A, 3C 111, NGC 1275 and M87) it was already detected by EGRET (Mukherjee et al. 2002). To construct the broad–band nuclear SED, the radio to optical/UV data were collected from literature, while for the high energy points, all available archival data, from *XMM–Newton*, *Swift* and *Chandra* satellites, were re–analyzed. The *XMM–Newton* observation of NGC 6251 (March 2002) was reduced using the SAS v.9.0 software and available calibration files. Events affected by high flaring activity were discarded. The resulting net exposure was 8.7 ks for the pn, 13.9 ks for the MOS1 and 13.5 ks for the MOS2. The source and background spectra were extracted from circular regions of 27″ radius, and the response matrices created using the SAS commands RMFGEN and ARFGEN. The nuclear data are not affected by pile–up. Data were grouped to 25 counts per bin in order to apply the χ^2 statistics. The best fit (χ^2/d.o.f.=410/372) for the pn spectrum (0.3–10 keV) consists of an absorbed power law ($N_{H_{Gal}}$=5.4×10^{20} cm^{-2}; Kalberla et al. 2005) plus an APEC component (kT∼0.6). There is no significant evidence for a Fe Kα emission line. These parameters are in agreement with those found by Evans et al. (2005). The same results were obtained using the MOS data.

The *Swift*/X–Ray Telescope (XRT) observed NGC 6251 three times from April 2007 to May 2009. The X–ray data of the three observations were reduced using the on–line XRT data analysis tool provided by the ASDC. [4] Source spectra were extracted from a circular region of 20″ radius, while background spectra were taken from an annulus with an inner radius of 40″ and outer radius of 80″. Data were grouped to 20 counts per bin in order to apply the χ^2 statistics. All spectral fits were performed in the 0.5–10 keV band. The best–fit model is an absorbed power law with column density slightly in excess of the Galactic value. The XRT spectra do not require the addition of a soft thermal component, however notice that they are characterized by low signal–to–noise ratio. Interestingly, during the *XMM–Newton* observation the source appeared in a higher state (40% higher than *Swift*). A further change

[4] `http://swift.asdc.asi.it/`

in flux of about 15% was observed by *Swift* from 2007 to 2009 (see Fig. 1.23). This ∼2 years represent the shortest period during which X–ray flux variability has been detected, offering observational constraints on the nuclear origin of the γ–ray emission. Instead, the fast (hour–scale) temporal variability is excluded from the 0.5–10 keV lightcurves of the four datasets.

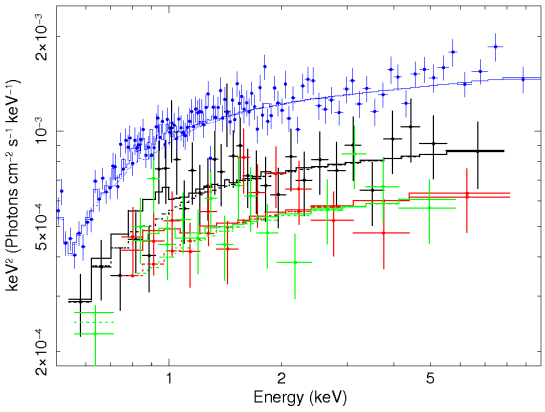

Figure 1.23 Unfolded spectral model of the combined *XMM–Newton* and *Swift* datasets. *Blue*: *XMM–Newton* observation of March 2002; *black*: *Swift* observation of April 2007; *red*: *Swift* observation of May 2009; *green*: *Swift* observation of June 2009.

The most recent (November 2003) and longest (49 ks) *Chandra* observation of NGC 6251 was also analyzed. However the nuclear data were affected by pile–up, estimated to be ≈13% using PIMMS [5], thus the *Chandra* nuclear fluxes were not considered in the SED.

The nuclear SED from radio to gamma is dominated by non–thermal emission. It was modeled with both a single–zone SSC and a structured jet model (Fig.1.24). When the SSC model is applied to the SED, it predicts lower Lorentz factors (Γ ∼2.4) with respect to BL Lacs (Γ ∼10), implying that a simple extension of BL Lac models to lower γ–ray luminosities FRI does not work. This poses serious problems to the unified models. Indeed the jet structure can be different in FRIs, as theorized by Ghisellini et al. (2005), with a fast inner component (the spine)

[5] `http://cxc.harvard.edu/toolkit/pimms.jsp`

and slower layer (the jet). The spine–layer model applied to NGC 6251 SED gives a good fit, solving at the same time any disagreement with the unified models.

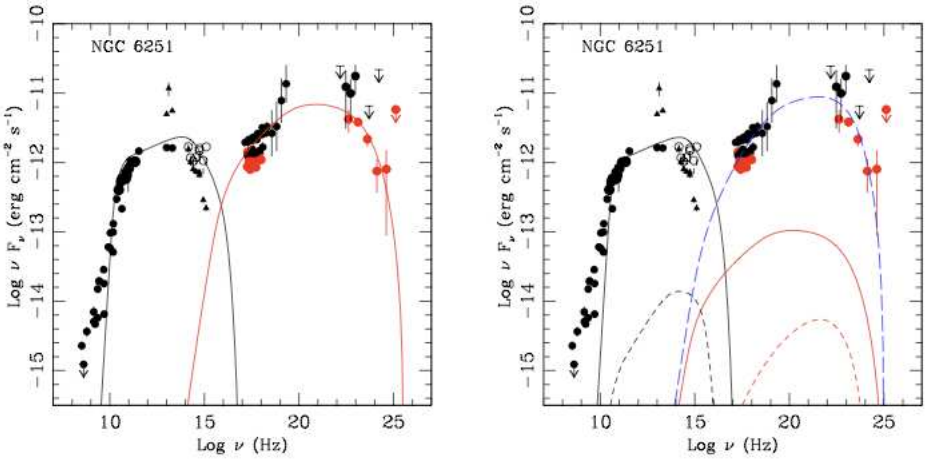

Figure 1.24 Nuclear broadband SED of NGC 6251 modeled with a one–zone SSC model in the *left panel* (solid black line: sychrotron curve; solid red line: IC emission) and the spine–layer model illustrated in Ghisellini et al. (2005) in the *right panel* (solid black and red lines: SSC emission of the layer; dashed black and red curves: SSC model for the spine; long dashed blue line: IC emission of the spine synchrotron photons off the layer relativistic electrons).

2

High resolution X–ray spectroscopy

X–ray astronomy was born between 1949, when X–ray radiation from the Sun was revealed with detectors onboard sub–orbital rockets (Friedman et al. 1951), and 1962, when the very first extra–solar source, i.e. Scorpius X–1, was discovered by Giacconi et al. (1962). During this half century life, huge steps forward were made in improving the sensitivity of X–ray observatories. Until recently, detailed images and spectra of cosmic sources were unavailable due to instrumental limitations. The first X–ray satellites carried onboard gas proportional counters providing limited spectral resolution ($E/\Delta E\sim$ few). The Japan mission *ASCA (Advanced Satellite for Cosmology and Astrophysics)* launched in 1993, was the first observatory that, carrying onboard Charge Coupled Devices (CCD) at the focus of the telescope, significantly improved the spectral resolution ($E/\Delta E\approx 10$). The astrophysical world had to wait *Chandra* and *XMM–Newton* satellites, NASA and ESA missions, respectively, both launched in 1999 and still operating, to achieve an impressive spatial and spectral resolution. A summary of what is the heritage of these two extraordinary missions can be found in Santos–Lleo et al. (2010).

Chandra and *XMM–Newton* were the first observatories incorporating diffraction grating spectrometers with $E/\Delta E\geq 200$ over the X–ray band 0.3–10 keV. Despite being a relatively new research field, high–resolution X–ray spectroscopy provided a wealth of information about cosmic X–ray sources, thanks to X–ray spectra with unprecedented precision, allowing to study the physics of such objects.

The advent of high–resolution grating spectrometers made X–ray spectroscopy the

most powerful tool for investigating the ionized components of the gaseous AGN environment. Indeed in many cases the gas temperature falls in the X–ray regime because the virial temperature kT$\sim$GMm$_p$/R is in the range 10^6–10^8 K (e.g. elliptical galaxies, cluster of galaxies) or because of shocks heating the gas (e.g. supernova remnants, binaries). The relative prominence of emission lines depends upon the abundances of different elements, and the location of K–shell and L–shell transitions associated with these elements within the X–ray band. The energies for the K– and L–shell transitions can be roughly approximated (from Moseley's formulae) as:

$$E_K \sim (10eV)Z^2 \tag{2.1}$$

and

$$E_L \sim (1.5eV)Z^2 \tag{2.2}$$

Thus the X–ray regime includes the K–shell features of Be (Z=4) through Ga (Z=31) and the L–shell transitions of O (Z=16) through Tl (Z=81). However looking at the standard cosmic abundances as represented in Fig. 2.1, it is evident that abundances of elements like lithium, beryllium and boron are very low. In addition, at high Z there is a very prominent abundance of iron (Z=26) that is a consequence of nuclear stability. Infact ^{56}Fe has the highest binding energy per nucleus of any nucleus and acts as a divide between *exothermic* fusion reactions (low Z) and *endothermic* ones. The X–ray band is therefore rich in discrete spectral features, mainly due to: the K–shell (n=2$\rightarrow$1) transitions of carbon though iron and the L–shell (n=3$\rightarrow$2) transitions of silicon through iron. Different charge states are visible in an X–ray spectrum, unambiguously interpretable. Due to the high radiative decay rate of X–ray transitions, astrophysical emitting plasmas are generally assumed not to be in local thermodynamic equilibrium (LTE), i.e. when the particle distributions and level populations are in equilibrium but not the radiation field. As a consequence, the derived spectra are sensitive to the physical conditions in the source, in particular are strongly dependent on the mechanisms by which the atomic levels are populated. In conclusion, investigating the single atomic features in the X–ray spectrum means to make the physics of the plasma, measuring the most important parameters without invoking any assumptions about the thermal state of the gas.

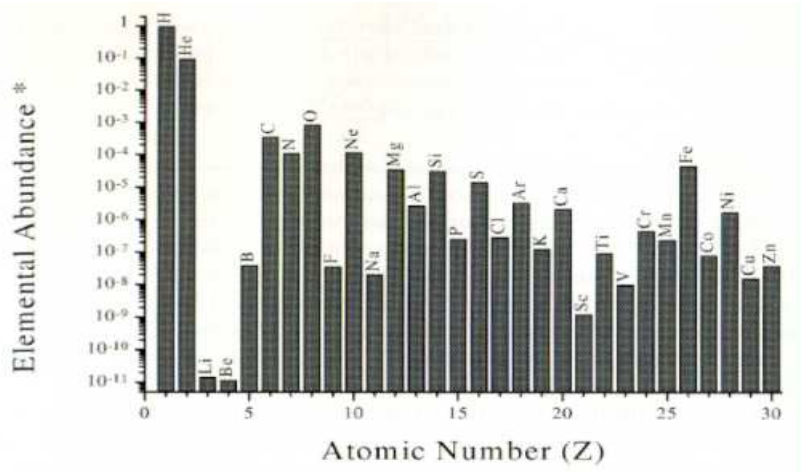

Figure 2.1 Cosmic elemental abundances as a function of the atomic number Z (from Kahn 2002). The elemental abundances are taken from Anders & Grevesse (1989).

2.1 Atomic processes and line diagnostics

In this section the most relevant atomic processes and the most useful plasma diagnostics are described. This discussion owes much to Kahn (2002), Porquet et al. (2000: 2001), Kinkhabwala et al. (2002), Blustin (2004) and Kaastra et al. (2008).

There are two main types of X–ray emitting and absorbing plasmas, *collision–driven* and *radiation–driven*.

1. *Collision–driven* plasmas are hot and mechanically heated through collisions: free electrons collide with the ions in the plasma transferring energy to electrons in the outer shells of the ions. X–ray emission lines are produced through radiative decay following electron impact excitation ($T_{sys} \sim E_{line}$). Generally, the collisional gas is thin to its own photons. However there are some cases in which this condition has to be relaxed to have a complete description of the phenomena. Hot plasmas are commonly found in the coronae of stars, in shock heated environment and in the ICM of clusters of galaxies. Among the most important collision–driven processes we mention: (i) collisional excitation and its quantum mechanical inverse de–excitation; (ii) collisional ionization and its inverse 3–body recombination. More details and deep explanations can

be found in the following papers: Raymond & Smith (1977), Mewe et al. (1985,1986), Kaastra (1992), Liedahl et al. (1995), Smith et al. (2001).

2. *Radiation–driven* photoionized plasmas are irradiated by a powerful external source. X–ray emission lines are produced through recombination/radiative cascade following photoionization, and radiative decay following photoexcitation. The plasma temperature is lower with respect to collisional gas, consistent with that necessary for photon heating. Photoionized plasmas have been found in X–ray binaries, AGN outflows, cataclysmic variables, etc.

2.1.1 Radiation–driven processes

Since radiation–driven processes are the most important mechanisms in the intense field of an AGN, in this Section they are described in detail. Fig. 2.2 shows the two principal radiation–driven processes, photoexcitation followed by radiative decay and photoionization followed by recombination/radiative cascade. Both involve the excitation of an electron that moves to a higher energy state, but in photoexcitation the energy of the absorbed photon is too low (E_{ph} <e$^-$ binding energy) to remove the electron from the ion. In such case the electron transfers enough energy to a bound electron to enable it to move to a higher energy level. For this reason we refer to photoexcitation as a *bound–bound* transition because the electron remains bound to the ion. In photoionization the photon has sufficient energy to remove one or more electrons from an atom and to ionize it (*bound–free* transition). The photon energy over and above the ionization energy, i.e., the energy threshold needed to remove the electron, becomes the kinetic energy of the removed electron. UV photons could be sufficient to remove outer–shell electrons, while X–rays are required to remove the inner shell electrons of a high–Z element like iron.

In general, for astrophysical plasmas the cross–section of photoexcitation resonant transitions can be expressed as:

$$\sigma_{PE}(\omega) = \frac{\pi e^2}{m_e c}\phi(\omega) \tag{2.3}$$

that is obtained from the photoexcitation cross–section assuming only natural quantum–mechanical line broadening plus thermal and/or bulk velocity broadening. Thus $\phi(\omega)$ is the natural linewidth convolved with the additional velocity broadening. After the ion is photoexcited it relaxes through radiative decay. The radiative de-

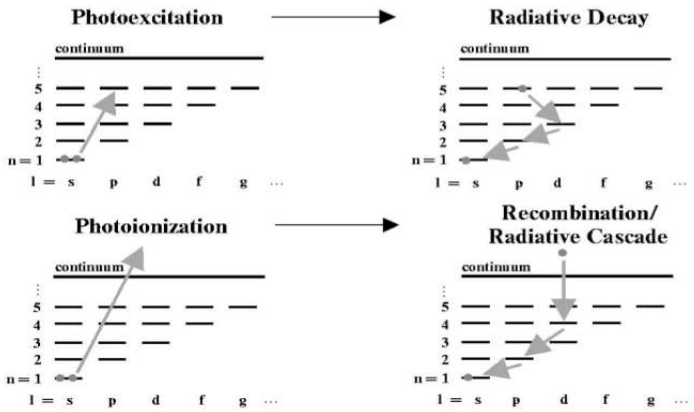

Figure 2.2 Representation of the two main radiation–driven processes, photoexcitation and photoionization, with their inverse processes, radiative decay and recombination/radiative cascade, respectively. Radiative decays generally occur directly to the ground state but other paths are possible. In radiative recombinations a free electron in a continuum state decays into a bound discrete state and emits a photon.

cay rate is:

$$A_{i\rightarrow f} = \frac{2}{3}\frac{e^2\omega_{if}^2}{m_e c^3} f_{i\rightarrow f} \tag{2.4}$$

where ω_{if} is the resonance frequency and $f_{i\rightarrow f}$ is the oscillator strength of the transition, i.e., the probability that a transfer occurs. Given the direct proportionality of $A_{i\rightarrow f}$ to the frequency squared of the transition, it is evident that higher energy transitions decay faster than lower energy transitions, i.e., X–ray transitions decay much faster than other processes. Thus ions can be assumed to be in their ground state configuration. The same is not generally true for longer wavelength regimes (UV, optical, IR) where transitions decay slower and excited state ions are non–negligible.

In photoionized plasmas the cross–section (for the n^{th} shell) is:

$$\sigma_{PI}^{n}(E) = \frac{64\alpha}{3^{3/2}}\frac{Z^4}{n^5}(\frac{Ry}{E})^3 \pi a_0^2 g \tag{2.5}$$

where g is the (free–free) Gaunt factor and E is given in Rydbergs (1 Ry=13.6 eV). Since there is only one energy value (ionization energy) at which a transition can occur, this leads to the formation of an absorption line in a narrow energy range. In

case of photoionization when a bound–free transition takes place, the electron can be removed by any photon with an energy greater than the threshold. Consequently, the absorption feature produced by a bound–free transition is very spread–out: it is deepest at the ionization energy and becomes weaker with increasing energy (Blustin 2004).
The inverse process to photoionization is *radiative recombination*. A free electron in a continuum state decays into a bound discrete state through the emission of a photon:

$$e^- + ion \rightarrow photon \tag{2.6}$$

If the distribution is thermal (Maxwellian), the shape of the resulting *radiative recombination continua* (RRC) is determined by the electron temperature T_e. From the width of RRC features, it is possible to derive a direct measurement of the recombining electron temperature (Liedahl & Paerels 1996) as shown in Fig. 2.3. In a collisional plasma electrons have high temperatures, so the RRC will be broad and shallow, difficult to distinguish from the underlying thermal continuum. On the other hand, when the plasma is photoionized, the electrons are at a lower temperature for the same level of ionization with a narrower distribution of energies. Thus the RRC are narrow and prominent features at the ionization energy (i.e. absorption edge position) of a given ion.

Other two radiation–driven processes have to be mentioned: the *fluorescence* and the *autoionization*. The fluorescence process involvs two steps. In the first step a photon with an energy above the K–shell photoionization threshold energy ionizes a 1s electron. In the second step the excited state can decay through the emission of a photon (fluorescence). In the radiative decay a bound electron fills the 1s hole leaving a vacancy in another shell.The most probable radiative decay involves a n=2 $\rightarrow$ n=1 transition (K_α) . It is appreciable for high Z–elements since the radiative decay scales like Z^4 (see Section 2.1.2 for details).

More often states with holes in the K–shell will autoionize (autoionization) ejecting a second electron (the *Auger effect*), leaving the atom in the next highest stage of ionization. If the atom is not stabilized it can undergo further Auger decays. This process dominates for low–Z elements. Autoionization of an atom can also occur without the capture of radiation. It occurs when an ion captures a free electron, that expends the lost energy in exciting a core electron. The resulting atom is doubly excited. It can decay by autoionization ejecting the electron into the continuum (in this case there is no change of charge in the level of ionization

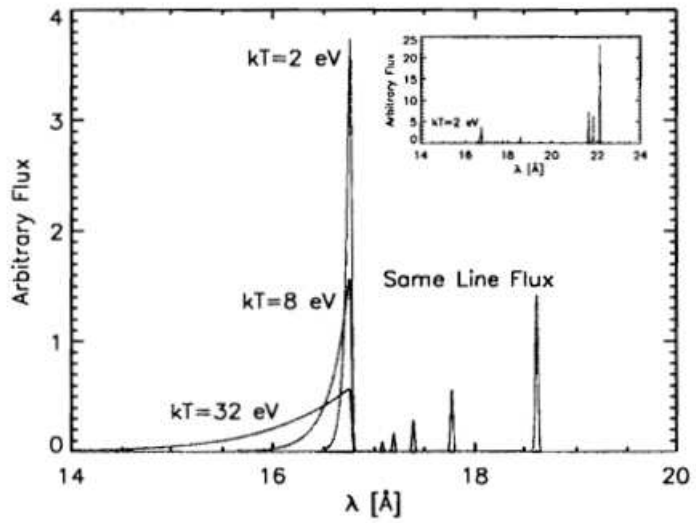

Figure 2.3 Radiative recombination continua (RRC) for He–like O. The relative line strengths do not change as a function of temperature, but the shape does, providing a measure of the plasma temperature. Indeed for low–T photoionized plasmas the RRC is a narrow and prominent feature. *Top right:* the whole range of OVII soft X–ray emission features at the recombining temperature of 2 keV. The RRC and the He–like triplet (r, i, f) are visible (see Section 2.1.3).

of the atom) or the atom can decay radiatively (the atom remains with an extra electron). The complete process, i.e., electron capture and radiative decay is called *dielectronic recombination*. It is possible that in an AGN both radiation–driven and collision–driven mechanisms are important (Kinkhabwala et al. 2002), i.e., *hybrid plasmas*. The X–ray spectra contain a combination of separate components of warm plasma (whose emission is dominated by photoionization and photoexcitation) and hot plasma (whose emission is dominated by electron impact excitations), and this is particularly true for radio galaxies that we know are quite often surrounded by collisional thermal gas. Since both plasmas produce the same ionic transitions, distinguishing between them is very hard and needs high–resolution X–ray spectroscopy.

2.1.2 Properties of photoionized plasmas

In photoionization equilibrium, the physical conditions of the gas are controlled (in part) by the radiation. The recombination rates depend on the ionization parameter ξ, that can be parametrized by the ratio of the ionizing flux to the electron density times the square of the distance of the source from the gas (Tarter Tucker and Salpeter 1969):

$$\xi = \frac{L}{nR^2} \text{ [erg cm s}^{-1}\text{]} \tag{2.7}$$

where L is the 1–1000 Rydberg ($\sim$13.6 eV–13.6 keV) source luminosity. Throughout this thesis I refer to ξ as the ionization parameter. The other definition of ionization parameter is U (Netzer 1996):

$$U = \frac{\int_{\nu}^{\infty} L_{\nu}/h\nu}{4\pi nR^2 c} d\nu \tag{2.8}$$

where c is the speed of light and is introduced to make U dimensionless. The relationship between ξ and U is:

$$\xi = U \frac{Lhc}{R_L^2 \int_{\nu}^{\infty} \frac{f_{\nu}}{\nu} d\nu} \tag{2.9}$$

In photoionization equilibrium the ionization structure is obtained by the balance between photoionization and recombination. The temperature is determined by solving the equation of the energy balance between heating and cooling processes. The self–consistent solution of the ionization and energy balance equation provides the fractional ionic abundances as a function of ξ and T(ξ). Fig. 2.4 represents

the fractional abundances of all the ions as a function of the ionization parameter. Besides H and He that are the principal elements the Universe is made of, all higher–Z elements (or "metals") that are important in astrophysics (see Fig. 2.1) are reported. Despite being only a small fraction of the mass, the radiative and thermodynamic properties of plasmas are highly dependent on the metals.
Fig. 2.5 shows the temperature as a function of the ionization parameter ξ. In both cases, the continuum was assumed to be a power law with a photon index $\Gamma = 2$. H defines the net heating rate. In equilibrium H=0. X–ray photoionized plasmas can be thermally unstable in certain regions of the ionization parameter space. The equilibrium curve separate regions for which H<0 and H>0. A negative slope in the equilibrium curve implies instability. This is better explained in Fig. 2.6, also known as the "S curve", that represents the same results of Fig. 2.5, but on the x–axis the ionization parameter is defined as $\Xi = \xi/4\pi ckT$.

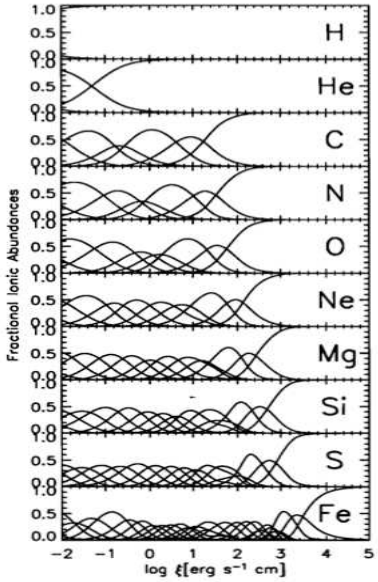

Figure 2.4 Fractional ionic abundances vs. ionization parameter (ξ) (Kinkhabwala 2003). At low values of ξ the neutral species dominate, whereas at high values the bare species approach unity.

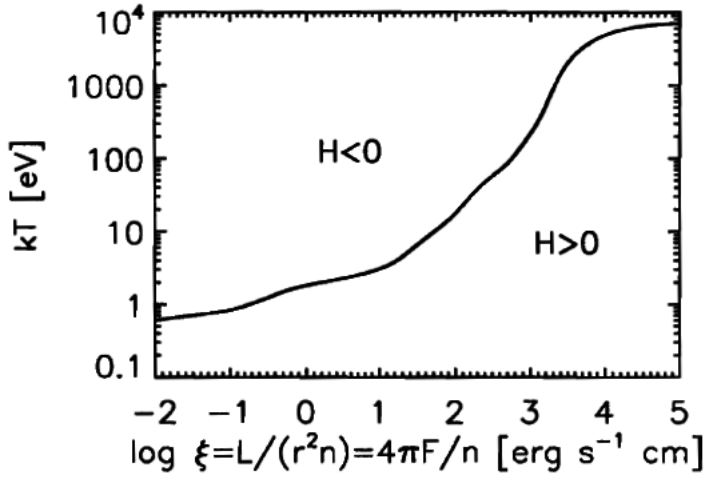

Figure 2.5 Temperature as a function of the ionization parameter ξ (from Kinkhabwala 2003). H is the net heating rate, when the plasma is in equilibrium H=0. In both cases, the continuum was assumed to be a power law with a photon index $\Gamma = 2$.

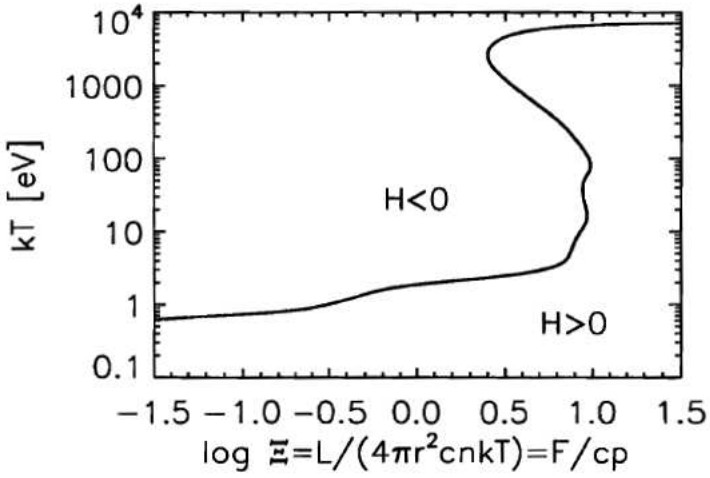

Figure 2.6 Temperature as a function of the ionization parameter Ξ, the "S–curve" (from Kinkhabwala 2003).

2.1.3 Plasma diagnostics

The spectral features formed are sensitive to the physical conditions in the gas. Thus they can be used as density and temperature diagnostics to discriminate between collisional or photoionized gas. However, as it is described below, not all the transitions have the same diagnostic utility.
The most prominent emission lines in the spectrum of X–ray emitting plasmas are:

1. the Lyman series transitions of H–like ions;
2. the He–like K–shell transitions;
3. the Fe L–shell transitions.

1) The Lyman series transitions ($n \geq 2 \rightarrow n=1$) are typical of low–Z abundant elements found in their H–like charge state (one electron left). These are degenerate transitions depending on the fine structure of the level:
Lyα_1: 1s–2p $^2P_{3/2}$; Lyα_2: 1s–2p $^2P_{1/2}$
Lyβ_1: 1s–3p $^2P_{3/2}$; Lyβ_2: 1s–3p $^2P_{1/2}$
Lyγ_1: 1s–4p $^2P_{3/2}$; Lyγ_2: 1s–4p $^2P_{1/2}$

all produced through electric dipole transitions. Despite their prominence, the diagnostic utility of Lyman series transitions is limited. The line ratios are only slightly different for collisional and photoionized plasmas, making challenging a solid conclusion on the driving mechanism (Fig. 2.7).

2) The He–like (two electrons left) K–shell transitions are of great importance in the soft X–ray band. These are triplets of emission lines whose ratios are sensitive to the density, temperature and ionization mechanism of the plasma. Being He–like charge state a very tight closed shell this is the dominant ion species over a wide range in temperature. The most important He-like transitions, also called He–like triplets, are:
R(or W): $1s^2\ ^1S_0$–1s2p $^1P_1$ *resonance line*
I(or X+Y): $1s^2\ ^1S_0$–1s2p $^3P_2$; $1s^2\ ^1S_0$–1s2p $^3P_1$ *intercombination line*
F(or Z): $1s^2\ ^1S_0$–1s2p $^3S_1$ *forbidden line*

The resonance line is an allowed electric dipole transition, while the forbidden line is a relativistic magnetic dipole transition characterized by a very low radiative

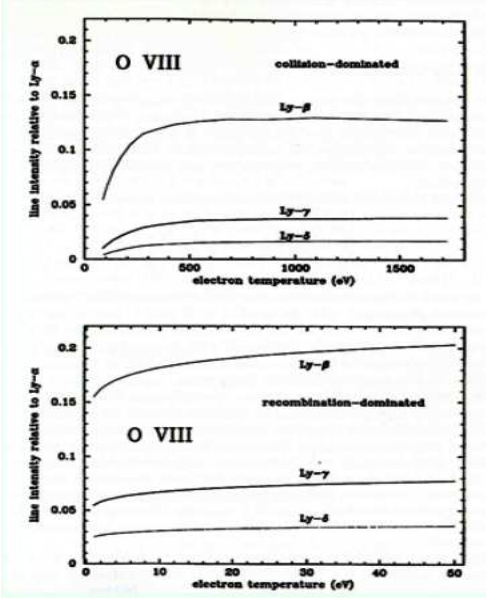

Figure 2.7 Plots of the ratio of higher series Lyman line fluxes to the Lyman α line flux as a function of the temperature in OVIII. *Top*: coronal plasmas. *Bottom*: photoionized plasma. From Kahn (2002).

decay rate and thus forbidden. These correspond to transitions from n=2 to n=1 shells. The ratios of these lines are sensitive to electron density

$$R = \frac{F}{I} \tag{2.10}$$

and to electronic temperature

$$G = \frac{I + F}{R} \tag{2.11}$$

G can be an important diagnostic to discriminate between photoionized plasmas (PI) or collisional plasma (CE). At high temperatures the collisional excitation is the dominant process, favouring the population of the $^1P_1$ level, i.e., the resonance (R or W) line. In this case G is around 1. At low temperatures the recombination (dot–dashed downward arrows in Fig. 2.8) is extremely efficient favoring the $^3P_{0,1,2}$ and $^3S_1$ population, i.e., the F (or Z) and I (or X+Y) lines.

The value of G is larger or greater to 4. This is illustrated in Fig. 2.9 that shows the dependence of G from the electronic temperature for the He–like OVII ion. An intermediate value of G, 1<G<4 implies an hybrid plasma (for example an AGN with a starburst component). Incidentally we note that Guainazzi & Bianchi (2007) propose a different criterion to discriminate between an AGN photoionizing source

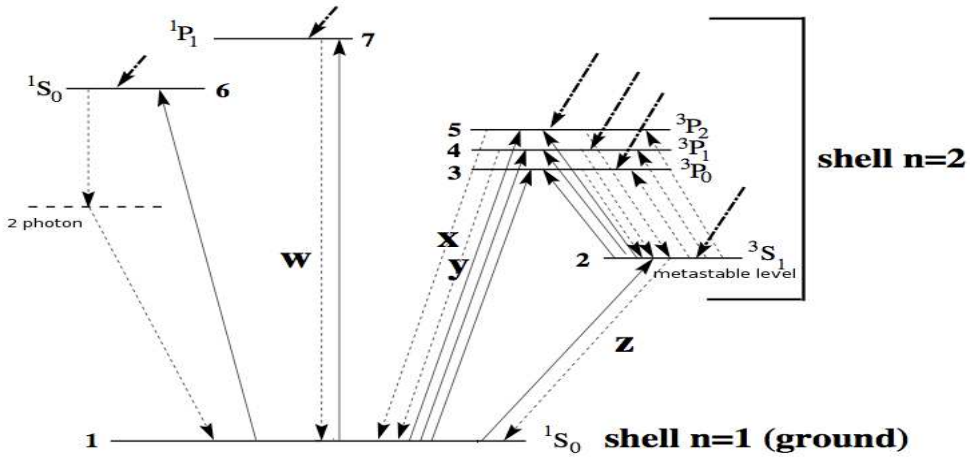

Figure 2.8 Simplified Gotrian diagram (Gabriel & Jordan 1969) for He–like triplets from Porquet & Dubau (2000). **W** is the resonant line, **X** and **Y** are the intercombination lines, **F** is the forbidden line. The *solid arrows* correspond to collision–driven transitions while the *broken arrows* correspond to radiative transitions. The broken arrow $^1S_0$ to the ground level corresponds to the 2–photon continuum. The *dot–dashed* arrows stay for recombination (radiative and dielectronic).

and a collisional gas related to a starburst, based on the intensity of the forbidden component of the OVII Heα triplet (normalized to the OVIII Lyα) coupled with the total luminosity in O lines integrated on all He– and H–like transitions (Fig. 2.10):

$$\frac{OVII(f)/OVIIILy\alpha}{L_O} \geq 1 \tag{2.12}$$

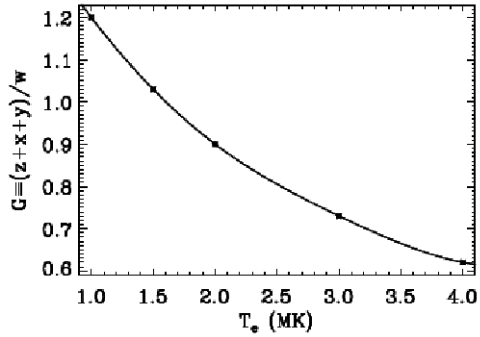

Figure 2.9 Plot representing the G ratio as a funtion of the electronic temperature T_e for n_e=10^{10} cm^{-3}. Figure from Porquet et al. (2010).

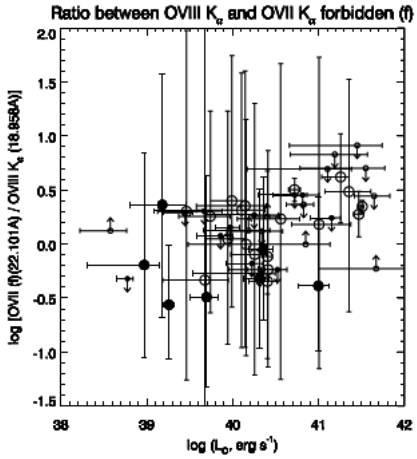

Figure 2.10 Intensity of the OVII f component normalized to the OVIII Lyα intensity against the total luminosity in O lines for the sources of the CIELO sample (from Guainazzi & Bianchi 2007). *Empty circles* are the obscured AGNs of the sample, while the *filled circles* are the controlled sample of starburst galaxies.

The R–ratio is a density diagnostic. When the density increases, collisional excitation shifts electrons from $^3S_1$ to the $^3P_{0,1,2}$ levels, implying a reduction of

the forbidden line and a R–ratio decrease. The R–ratio changes very fast over n_e decades, around a critical value n_{crit} that depends on Z. For $n_e < n_{crit}$ the R–ratio is almost constant and F is the dominant line. Above n_{crit} the $^3S_1$ level starts to be depopulated by electron impact and the R–ratio drops out rapidly. At very high densities, the intercombination line is completely dominant (Figg. 2.11 and 2.12). Caution in the pratical use of the diagnostics is however necessary. For example, some authors reported anomalous He–like G–ratios (Sako et al. 2000ab, Kinkhabwala et al. 2002) in the Seyfert 2 galaxies, MKN 3 and NGC 1068. It was suggested that photoexcitation could play an important role in intensify the resonance lines, infact after photoexcitation, radiative decay occurs directly to the ground state, but radiative cascade is also possible.

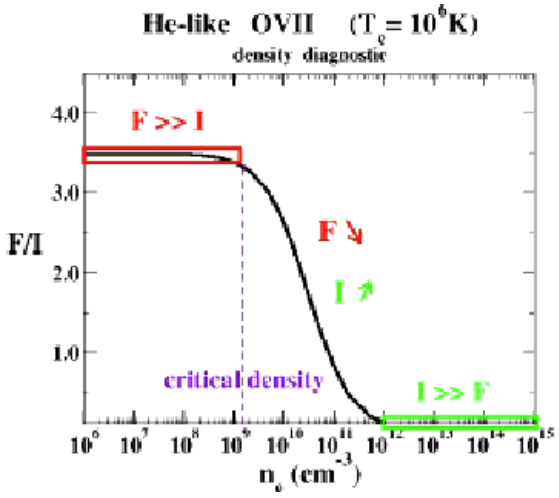

Figure 2.11 Plot the the R–ratio as a function of the electron density n_e for T_e=10^K. Calculations are from Porquet et al. (2001). Courtesy of D. Porquet.

Fig. 2.13 represents two cases: gas photoionized by the AGN alone, in which there is the contribution of photoexcitation (*left panel*), and gas photoionized by the AGN plus emission of hot collisional plasma produced in a starburst region. In the first case (photoionization plus photoexcitation) photoexcitation enhances all the resonant lines leaving unaltered the forbidden line. In the second example, collisionally ionized plasma enhances the triplet lines with more weight on the resonance feature. In both cases, the He–like triplet is not useful anymore in distin-

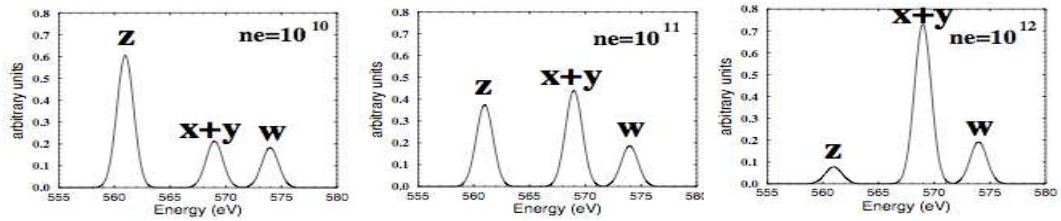

Figure 2.12 OVII theoretical spectra for three values of electron density in case of a "pure" photoionized plasma (T_e=10^5 K). Approximately this is the range where the R–ratio (F/I) is sensitive to density. Increasing the electron density the forbidden line is suppressed in favor of the intercombination line. The same trend is produced by a strong UV radiation field. Figure from Porquet & Dubau (2000).

guishing between the two plasmas, what is helpful yet is the presence of the narrow RRC as in the third box of the left panel. It is important to notice that also the enhancement of the resonant lines of higher–order series (np → 1s) is indicative of photoexcitation. Thus the narrow RRC are among the most useful diagnostics for distinguishing collisional plasmas from photoionized plasmas.

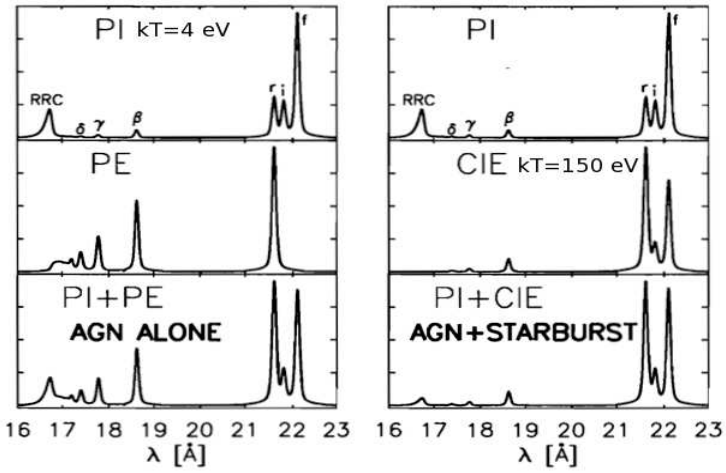

Figure 2.13 Representation of a photoionized plasma spectrum in which radiative decay following photoexcitation (*left panel*) or collisional excitation from starburst regions (*right panel*) have occurred. The final resulting spectra (third boxes of both panels) are quite similar. The He–like triplet is not helpful anymore in discriminating between the two plasmas. However in the "AGN ALONE" transitions, the RRC and the higher–order series transitions play a significant diagnostic role.

3) Iron is the most abundant high–Z element, and its K– L– and even M–shell transitions (Fig. 2.14) are very important in the overall X–ray spectrum (0.2–10 keV). For collisionally ionized plasmas, iron L–shell complexes sample a wide range in temperature (0.2–2 keV) and contribute significant line emission even when the lower–Z elements are full stripped as a result of their higher ionization potential. L–shell transitions are temperature and density sensitive. The temperature sensitivity derives from the fact that the line positions are a strong function of the charge state, meaning that the ionization structure is easily discernible and provides a constraint on the temperature distribution. The density sensitivity arises from the fact that the intermediate iron L charge state (N– and C–like) possesses a number of low lying metastable levels (n=2 → n'=2) that can be populated through collisions. In such case collisions will lead to new "seed" states for n=2 → n=3 excitations and subsequent n=3 → n=2 radiative decays.

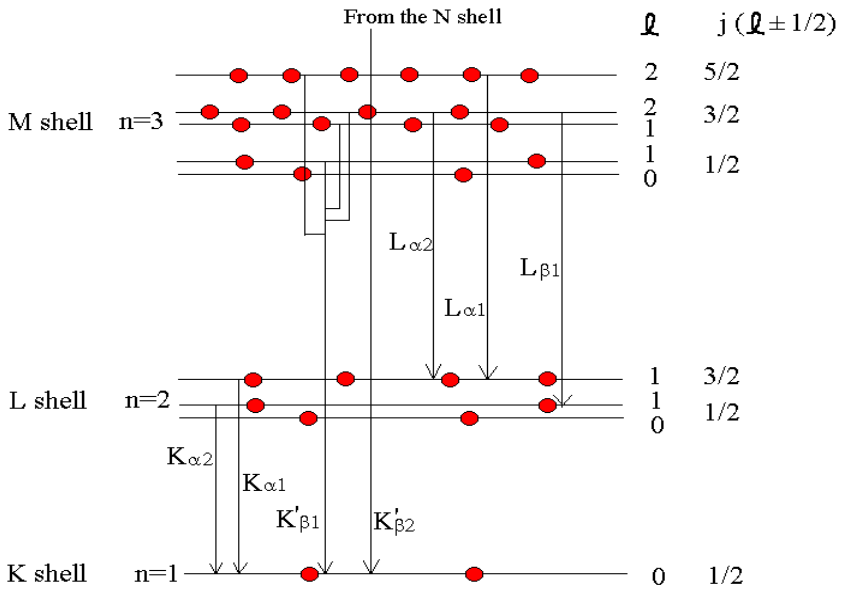

Figure 2.14 Representation of the allowed energy level and allowed electronic transitions for a generic atom. n is the principal atomic number and depends on the distance between the electron and the nucleus; l is the azimuthal atomic number and defines the orbital shape; j is the total angular momentum and generates rotations in the space. From `http://ie.lbl.gov/xray/.`

Iron is important also and in particular at higher energies (6–7 keV). Historically iron Kα was the only discrete atomic feature measurable prior to *Chandra* and *XMM–Newton*. A crucial mechanism which involves iron K emission is *fluorescence* from cold material in the vicinity of a bright X–ray continuum (see Section 2.1.1). The near–neutral iron K fluorescence line (Kα) falls at 6.4 keV and it can be distinguished from the He–like lines at 6.7 keV and the Lyman α line at 7.1 keV.

2.1.4 Absorption

Absorption features are produced by intervening matter along the line–of–sight that absorbs part of the X–rays emitted by a source. The imprinting of an absorption feature on the intrinsic continuum is determined by $e^{-\tau_{(E)}}$ where

$$\tau(E) = \sum_i N_i \sigma_i(E) \tag{2.13}$$

N_i is the column density of the various ions, and σ_i(E) represents the total photoionization cross–sections.
The transmission in a spectral line at wavelength λ is given by (Kaastra et a. 2008):

$$T(\lambda) = e^{-\tau(\lambda)} \tag{2.14}$$

with $\tau(\lambda)$=$\tau_0\phi(\lambda)$ and $\phi(\lambda)$ is the line profile. τ_0 is the opacity at the line centre λ_0 and can be expressed as:

$$\tau_0 = \frac{\alpha h \lambda f N_i}{2\sqrt{2\pi} m_e \sigma_v} \tag{2.15}$$

α is the fine structure constant, h is the Planck's constant, f is the oscillator strength, N_i is the ionic column density and finally σ_v is the velocity dispersion. It is evident that the optical depth, apart from atomic parameters, depends on the absorber properties (N_i and σ_v),
The shape of a line follows the Voigt profile, that results from the convolution of the Gaussian profile and the Lorentzian profile. The Gaussian profile accounts for thermal broadening, microturbulence and bulk motions and corresponds to pure Doppler broadening for a thermal plasma. The Lorentzian profile origins from the natural width of the line and has a narrow core and extended wings. The Voigt profile changes with the optical depth (Fig. 2.15). In the optically thin regime (low optical depth and low absorbing column) the column density can be directly derived from the depth of the line (Blustin 2004). This is not possible in the optically thick

regime because the line is saturated, and absorbs away all the continuum flux at its central wavelength.

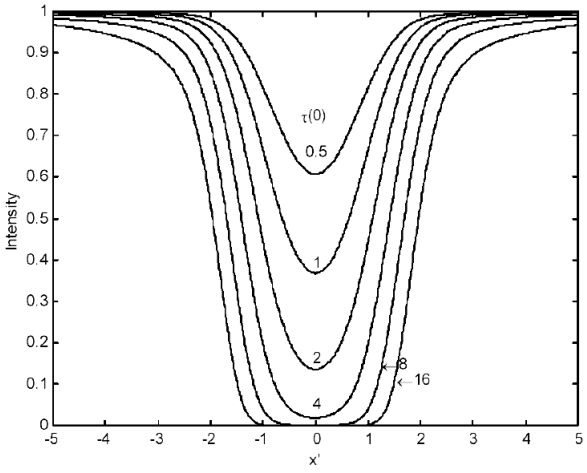

Figure 2.15 Voigt profile plotted at a range of optical depth (from Blustin 2004). x'=λ-λ_0.

The strength (or depth) of a line is measured by the equivalent width (EW) and is the area of the spectral continuum taken up by the line. It is calculated from:

$$EW = \int \frac{(F_c - F_\lambda)}{F_c} d\lambda \tag{2.16}$$

F_λ is the flux in the interested area of the line, F_c is the flux of the continuum.

Absorption lines can be of several types. There are the strong resonance lines involving the outermost atomic shells like the OVII 1s–2p at 21.6 $\mathring{A}$ and OVIII Lyα doublet at 18.97 $\mathring{A}$, or the inner–shell absorption lines. The absorption lines could be well resolved or strongly blended because neither they are produced by higher principal quantum number transitions nor the column density is very high (Kaastra et al. 2008). The iron M–shell (n=2 $\rightarrow$ 3) transitions of FeI – FeXVI are an example of strongly blended lines. They manifest themselves as a broad absorption feature around 16–17 $\mathring{A}$. This feature is hard to resolve spectroscopically and has been identified as *unresolved transition array* (UTA) mainly due to 2p–3d inner shell absorption in M–shell iron (Sako et al. 2001; Behar et al. 2001; Netzer et al. 2004). Before the advent of high–resolution grating spectrometers this structure might be identified as an OVII edge. The equivalent width (EW) and central wavelength of the UTA are potentially important diagnostics of AGN absorbers. An example of

UTA is reported in Fig. 2.16.

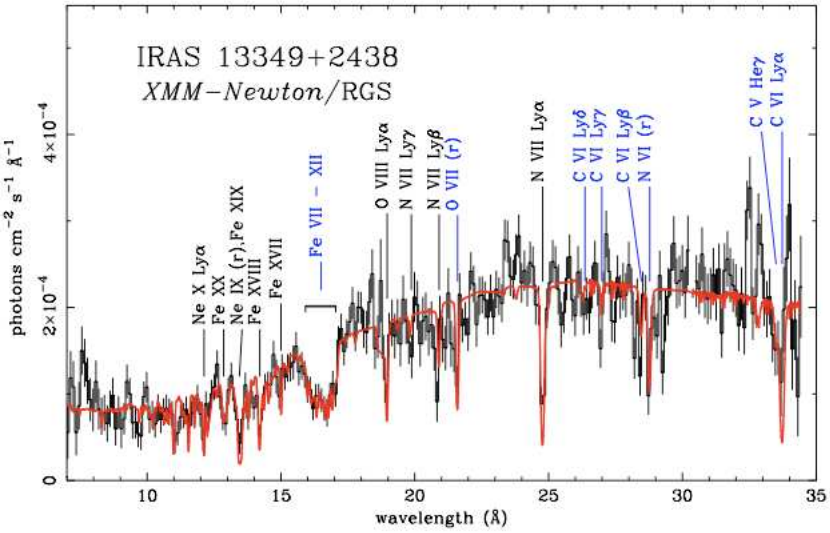

Figure 2.16 First detection of iron UTA feature, λ=16–17 $\mathring{A}$ in the spectrum of IRAS 13349+2438 (Sako et al. 2001).

3

Warm photoionized gas in emission

The spectrum observed from a photoionized medium depends on the relative orientation of the irradiating source, the irradiated medium and the observer. Fig. 3.1 represents a sketch of the two extreme cases of orientation: in the "Absorption" direction the relative soft X–ray spectrum will result in discrete line absorption (photoexcitation) plus photoelectric edge absorption (photoionization) corresponding to the *upper panel* of Fig. 3.2. This is a typical Seyfert 1 spectrum in which the central engine is not obscured by an intervening medium, i.e. the torus, and the features produced by the warm absorber (see Chapter 4) are detected.

If the orientation is in the "Reemission" direction, the X–ray intrinsic continuum is blocked by a dusty torus allowing only reprocessed radiation to be visible in the spectrum (Fig. 3.2 *bottom panel*). In this scenario all photoexcitations and photoionizations are balanced by radiative decays and recombination/radiative cascades. Seyfert 2s are characterized by similar spectra.

The detection and identification of emission lines in Seyfert 2 galaxies, thanks to high–resolution X–ray spectroscopy, has revealed large scale emitting gas ($kT \sim$ few keV), photoionized by the nuclear engine (Sako et al. 2000; Kinkhabwala et al. 2002; Bianchi et al. 2005; Pounds & Vaughan 2006; Guainazzi & Bianchi 2007). Spatially resolved studies performed with the *Chandra* telescope for at least the three brightest AGNs, NGC 1068 (Kinkhabwala et al. 2002; Brinkman et al. 2002; Ogle et al. 2003), Circinus (Sambruna et al. 2001), and Mrk 3 (Sako et al. 2000ab; Bianchi et al. 2005; Pounds & Page 2005), have pointed out that the soft X-ray emission originates in regions extended on hundreds of pc, and its dimension and morphology closely resembles that of the Narrow Line Region (NLR) as mapped by

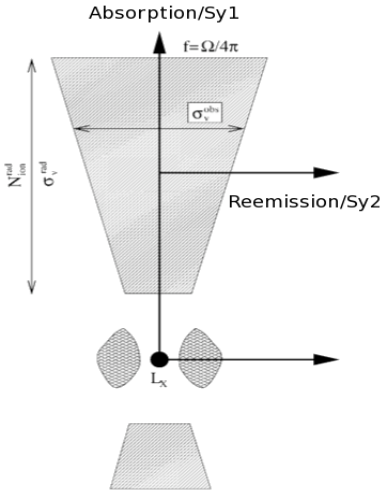

Figure 3.1 Simple sketch adapted from Kinkhabwala et al. (2002) representing the two possible orientations of an AGN with respect to the observer line–of–sight. σ_v^{rad} is the radial velocity width; N_{ion}^{rad} is the radial ionic column density and $f = \Omega/4\pi$ is the covering factor expressed in terms of the solid angle subtended by the plasma.

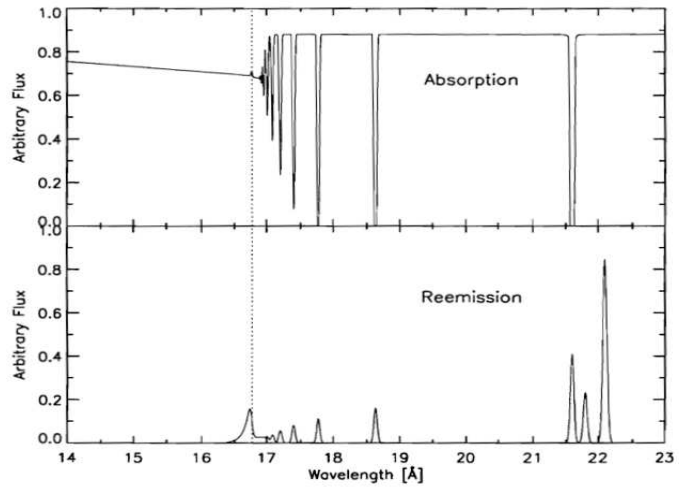

Figure 3.2 Figure from Kinkhabwala (2003) representing absorption (*top*) and reemission (*bottom*) spectra of He–like O (the dashed line indicates the photoionization threshold). This is what we would observe from the same object viewed in Seyfert 1 or Seyfert 2 directions (Unified Model). In Seyfert 1s the ionized cone (warm absorber) is seen through its absorption of the intrinsic nuclear continuum, while in Seyfert 2s the intrinsic nuclear continuum is highly absorbed by the dusty torus, thus only reprocessed emission in the ionized cone can be observed.

the optical [OIII]λ5007 emission line (e.g. Bianchi, Guainazzi & Chiaberge 2006). Concerning Radio–Loud AGNs, the attention has been addressed so far to the extraordinary phenomena related to the jets at kpc scales. The relativistic plasma produces bright hot spots interacting with the environment, excavates cavities in the intracluster medium (ICM) and upscatters microwave background photons. Nuclear and circumnuclear environment has not yet been studied with the same effort. This is not surprising since RL AGNs are intrinsically complex sources, because the relativistic jet blurres the overall picture making hard to disentangle its non-thermal emission from other kinds of radiation. For example, the X–ray spectrum of FRII radio galaxies optically classified as High Excitation Galaxies (HEG) are quite similar to Seyfert 2s. They show a heavily obscured emission (intrinsic column density $\sim 10^{23-24}$ cm^{-2}) and a soft unabsorbed tail (Belsole et al. 2006; Hardcastle et al. 2006; Evans et al. 2006). While the former component is clearly related to the bright accretion disk obscured by an edge–on oriented thick torus, the nature of the soft excess was not immediately understood. At first it was proposed that soft photons originate from the jet emerging from the top of the torus. However the discovery of photoionized emission lines in the soft X–ray spectrum of the obscured BLRG 3C 445 (Grandi et al. 2007; Sambruna et al. 2007; Reeves et al. 2010) and in the type 2 quasar 3C 234 (Piconcelli et al. 2008) weakened this hypothesis and opened a new and alternative way to interpret the soft excess.
The study of the NLRG 3C 33 (Torresi et al. 2009), that is part of this thesis, is a work in strong support to the thermal interpretation of the soft excess in radio galaxies.

3.1 Evidence of photoionized gas in the soft X–ray spectrum of 3C 33

This section describes the X-ray data analysis of the NLRG 3C 33. All the observations available in the *Chandra* and *XMM-Newton* archives have been used to investigate the X-ray spectral properties of this source. The main result is the detection in both ACIS and EPIC spectra of emission lines in the 0.5–2 keV band, that can be attributed to photoionized emitting gas. Unfortunately, due to the shortness of the *XMM–Newton* observation, and consequently to the low S/N ratio, the RGS data could not be used.

3.1.1 Introduction

3C 33 is the ideal target to investigate the nature of the soft excess. It is a genuine type II radio galaxy (L_{178}=7.5×10^{25} W Hz^{-1} sr^{-1}), optically classified as High Excitation Galaxy (HEG) and one of closest HEG in the 3CRR catalogue (Laing, Riley & Longair 1983) located at z=0.0597 (Popescu et al. 1996).
It exhibits symmetric lobes with hot spots on kpc scale (Leahy & Perley 1991), and two symmetric jets in the VLBI image (Giovannini et al. 2005). The southern jet is stronger by a factor 2 at 5 mas. Expressing the jet/counterjet ratio (J) in terms of the bulk velocity of the jet (β) and the angle between the jet and the line–of–sight (θ) (see Section 1.2.3), an inclination angle of $75° - 80°$ can be deduced. Its spatial orientation is then favorable for revealing soft X–ray emission lines, because a strong de–amplification of the jet radiation is expected. Fig. 3.3 represents the unsmoothed *Chandra* 0.3–2 keV image with 1.5 GHz radio conoturs overlaid.
Moreover 3C 33 is very luminous in the [OIII] band ($L_{[OIII]}$ ∼1.09×10^{42} erg s^{-1}) exhibiting the highest [OIII] flux of all nearby NLRGs (z<0.3) in the 3CRR sample. This is a very important observational property since the [OIII]λ5007 emission line is a powerful tracer of the NLR.

Previous nuclear observations of 3C 33 in the X–ray band date to those of the *EINSTEIN* (Fabbiano et al. 1984) and *ROSAT* (Hardcastle et al. 1998; Hardcastle et al. 1999) X–ray telescopes. *EINSTEIN* only provided an upper limit to the 0.5–3 keV luminosity, while *ROSAT*/HRI could detect the source in the soft X–ray band, although the HRI instrument onboard was not able to resolve the source.
Evans et al. (2006) analyzed the *XMM-Newton* EPIC pn data of 3C 33 showing for the first time the Seyfert 2 nature of its hard component. They modeled the soft component with an unabsorbed power law.
Taking advantage of the unprecedented imaging of *Chandra*, Kraft et al. (2007) performed a detailed spatial study of 3C 33, resolving the north and south hot–spot regions. They also studied the nuclear component with a basic model consisting of an absorbed power law plus a Fe Kα line. The soft part was fitted with a collisional gas model associated to the clearly extended structure around the unresolved hard nucleus. A similar elongation was observed in the *Hubble Space Telescope* WFPC1 and WFPC2 imaging, and was interpreted by the authors as a tracer of stellar distribution.
Large residuals between 1 and 3 keV, still present in the *Chandra* spectrum, were explained by assuming the presence of either a reflection component or a less absorbed

power law, interpreted as jet emission on parsec scale.

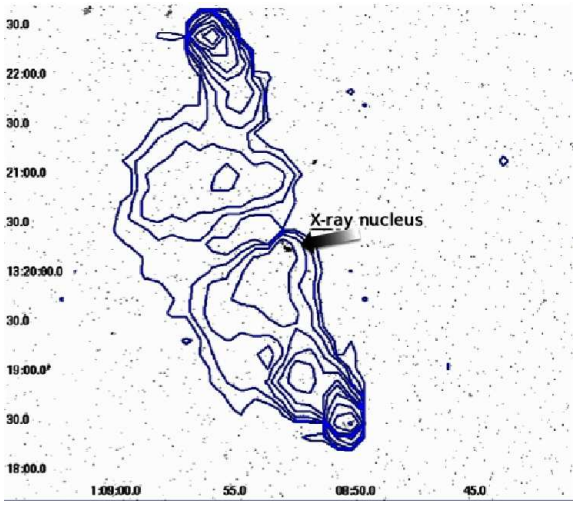

Figure 3.3 Unsmoothed *Chandra* ACIS–S image of 3C 33 in the 0.3–2.0 keV band with 1.5 GHz radio contours overlaid (from Leahy & Perley 1991). The position of the X–ray nucleus is labelled.

3.1.2 Observations and data reduction

Chandra ACIS–S observed 3C 33 twice, on 2005 November 8 (t_{exp} ∼20 ks) and on 2005 November 12 (t_{exp} ∼20 ks). Spectra and instrument responses were generated using the Chandra Interactive Analysis of Observations (CIAO) 3.4 and the Chandra Calibration Database (CALDB) 3.4.3. The source spectrum was extracted from a circular region of radius 1.5″ centered on the peak of the X–ray emission, while background counts were extracted from a 4″ radius circle within the same CCD, but outside the extended emission of the source. The *Chandra* count rate from the nucleus in both observations was ∼0.06 cts s^{-1}, implying a negligible pileup effect. In the hard band (2–8 keV), the X–ray morphology of the 3C 33 nucleus is point–like. An extended structure around the nucleus becomes evident in the soft band (0.5–2 keV), looking approximately elliptical, with a major axis of ∼ 5″, elongated in the northeast-southwest (NE-SW) axis (see also Kraft et al. 2007). A larger extraction radius for the nuclear source (r=4.5″) was also considered in order to include the extended soft X–ray emission. As expected, the statistical quality of the spectrum decreased due to the higher background. Few source counts were de-

tected in the 0.5–2 keV band from an elliptical region of 5.5″ semi–major axis and 4″ semi–minor axis (excluding the nucleus), less than 3% of the total counts in the 1.5″ region. In physical terms, most of the soft X–ray radiation comes from $\sim$ 2 kpc around the source. We then considered the smaller nuclear region in order to maximize the spectrum signal–to–noise ratio (S/N).

XMM-Newton observed 3C 33 twice, on 2004 January 4 and January 21. Both observations were checked but only the second pointing ($t_{exp} \sim 9$ ks) was analyzed, because the first one was affected by high flaring activity, which prevented the use of the RGS data.
The EPIC cameras were operating in "prime full window" mode. The data were reduced using the SAS (v. 7.1) with standard procedures.
The light curve over 10 keV was extracted to check high background periods. Time intervals characterized by a count rate higher than 1.0 cts/s in the EPIC pn, and 0.35 cts/s in the EPIC MOS were excluded. After this data cleaning, net exposures of 6.3 ks for the pn and 8.5 ks for the two MOS cameras were obtained.
The source and the background spectra were extracted from circular regions of 35″ radius. The background was taken from the same CCD that contains the source, but within a region that was not contaminated by the source itself. The source counts were $\sim$1500 and $\sim$1000 in the pn and the two combined MOS, respectively. The response matrices were created using the SAS commands RMFGEN and ARFGEN.
Events outside the 0.5–10 keV band were discarded in both the pn and MOS spectra (Kirsch 2006).
All spectral fits discussed in the next Section include absorption due to a line–of–sight Galactic column density of N_H=3.06 $\times 10^{20}$cm^{-2} (Kalberla et al. 2005).
Errors are quoted at the 90% confidence level ($\Delta\chi^2$=2.7) for one interesting parameter.
The cosmological parameters used throughout this thesis are $H_0 = 70$ km^{-1} s^{-1} Mpc^{-1}, $\Omega_m = 0.3$, $\Omega_\Lambda = 0.7$ (Spergel et al. 2007). When a different cosmology is applied it will be mentioned. For 3C 33, z=0.0597 corresponds to a luminosity distance of 263.9 Mpc, and 1″ corresponds to a physical scale of 1.14 kpc.
The spectral analysis obtained by both telescopes was performed using the XSPEC 11.3 package (Arnaud 1996).

3.1.3 Spectral analysis

The *Chandra* data were simultaneously analyzed.

The broad–band spectrum appeared quite complex. It was initially decided to fit only the 3–10 keV energy range in order to focus on the hard X–ray continuum and to exclude the soft X–ray part. At first, a photoelectrically absorbed power law plus a Gaussian line profile were applied. The restricted energy band and the limited statistics did not allow to constrain very well the spectral index (the column density and the spectral index being strongly correlated), so Γ was fixed to the value of 1.7, following Kraft et al. (2007). This choice was confirmed to be the right one by the *XMM-Newton* analysis (see below). Since the χ^2/d.o.f./=102/80 was not completely satisfactory, the presence of a reflection component, often required in obscured AGNs, e.g., Mrk 3 (Pounds & Page 2005); 3C 445 (Grandi et al. 2007; Sambruna et al. 2007), was tested. When a *pexrav* (Magdziarz & Zdziarski 1995) model was applied the value of χ^2 decreased to 82 for 79 d.o.f., providing a more accurate representation of the data (P_F=99.99%). The reflection (R=$\Omega/2\pi$) was let free to vary, while the high–energy cutoff of the incident power law was set at 160 keV (Grandi, Malaguti & Fiocchi 2006), and the elemental abundances were assumed to be of solar value. This analysis was repeated allowing Γ to vary freely. Also in this case, the addition of a reflection component improves the fit, even if the strong correlation between the reflection component, the photon index and the column density prevented an accurate constrain of these three variables.
The Fe Kα emission line is unresolved. The rest–frame energy is $E_{K\alpha}=6.38^{+0.05}_{-0.06}$ keV, the upper limit of the intrinsic width is σ <180 eV and the equivalent width is $EW_{K\alpha}=172^{+84}_{-76}$ eV (Fig. 3.6).

Once a good fit of the hard component was obtained this study was extended to the soft part (0.5–3 keV) of the spectrum. The simple extrapolation of the hard model introduced a strong soft component. In the literature, at least three different interpretations of the soft excess in obscured RL AGNs have been proposed:

i) thermal radiation from collisional gas (Kraft et al. 2007; Evans et al. 2006);

ii) non–thermal emission from the jet (Belsole et al. 2006);

iii) nuclear scattered radiation plus emission lines produced by circumnuclear photoionized gas (Bianchi & Guainazzi 2007; Grandi et al. 2007; Sambruna et al. 2007; Piconcelli et al. 2008).

All of these three possibilities were tested.
At first, the soft excess was reproduced with a thermal model (*mekal*) absorbed by the Galactic column density. This implicitly assumed that the soft excess is produced by collisional plasma (with solar abundances). The gas temperature required by the fit was $kT \sim 0.7$, and the model partially reproduced the soft excess, χ^2/d.o.f.=138/104, but the inspection of the residuals still showed excesses below 2 keV. A second *mekal* was added to verify whether a multi–temperature gas was present, but the second temperature shifted to an improbable value higher than 10 keV, and excesses were still present in the soft X–ray band (see Fig. 3.4 *left panel*). Note that if the abundances are free to vary, they become extremely low, resembling a power law. After replacing the "second" thermal emission model with a simple power law (where Γ_s is free to vary), that represents non–thermal emission, the χ^2 improved χ^2/d.o.f.=124/103, and the thermal emission was no longer required (the *mekal* model is consistent with zero). Although this was the best fit obtained so far, the model could not reproduce the soft X–ray data completely (Fig. 3.4 *right panel*).
Finally the third hypothesis was verified. A soft excess was fitted with a power law plus emission lines, as expected in case of circumnuclear photoionized gas. The soft power law slope (Γ_s) was linked to the hard one (Γ_h) in order to represent the scattered nuclear continnum. The fit (see Fig. 3.5 *left panel*) was very satisfactory χ^2/d.o.f.=103/99. A summary of the best–fit model parameters for the hard X–ray spectra is given in Table 3.1, while the detected lines and relative significance levels are listed in Table 3.2.

To obtain an independent confirmation of this result, we explored the *XMM-Newton* EPIC spectra. The pn and MOS results were reassuring. All the EPIC spectra (see Fig.3.5, *right panel*) were well fitted with the same *Chandra* best–fit model. Interestingly, the pn data even required soft lines at the same energies measured by *Chandra*.
The pn best–fit model parameters are listed in Tab. 3.3. The relative χ^2 is 37.5 for 37 d.o.f.

Table 3.1 *Chandra* ACIS–S best–fit parameters. Normalizations n are expressed in cm^{-2} s^{-1} keV^{-1}; the normalization of the iron line is expressed in photons cm^{-2} s^{-1}.

Γ	1.7^{*}
R	$2.18^{+0.48}_{-0.60}$
N_G	(3.06×10^{20}) cm^{-2}
N_H	$(5.28^{+1.04}_{-0.42}) \times 10^{23}$ cm^{-2}
n	$(1.83^{+0.51}_{-0.33}) \times 10^{-3}$
$n_{unobscured}$	$(4.48^{+3.43}_{-2.11}) \times 10^{-6}$
E_{Fe} (keV)	$6.38^{+0.05}_{-0.06}$
F_{Fe}	$(2.49^{+1.21}_{-1.11}) \times 10^{-5}$
EW (eV)	172^{+84}_{-76}
χ^2(d.o.f)	103(99)
Unabsorbed luminosity and absorbed flux	
$L_{0.5-2\ keV}$ (erg s^{-1})	$3.40\ \times10^{43}$
$L_{2-10\ keV}$ (erg s^{-1})	$7.31\ \times10^{43}$
$Flux_{0.5-2\ keV}$ (erg s^{-1} cm^{-2})	$5.75\ \times10^{-14}$
$Flux_{2-10\ keV}$ (erg s^{-1} cm^{-2})	$2.67\ \times10^{-12}$

(*) value fixed

Table 3.2 Emission lines detected in the *Chandra* ACIS–S spectrum. E_c is the centroid line energy (keV) in the source rest–frame; F is the line flux in units of 10^{-6} photons cm^{-2} s^{-1}; P_F is the significance of the fit improvement after including the Gaussian line in the model, based on the F–test.

Energy	*Intensity*	P_F	*Tentative IDs*
$0.76^{+0.02}_{-0.13}$	$2.93^{+1.16}_{-1.02}$	$> 98.9\%$	OVII RRC, Fe XVII 3s-2p
$0.93^{+0.04}_{-0.02}$	$2.51^{+0.85}_{-1.20}$	$> 99\%$	Ne IX rif
$1.30^{+0.04}_{-0.02}$	1.41 ± 0.46	$> 99.97\%$	Mg XI Heα

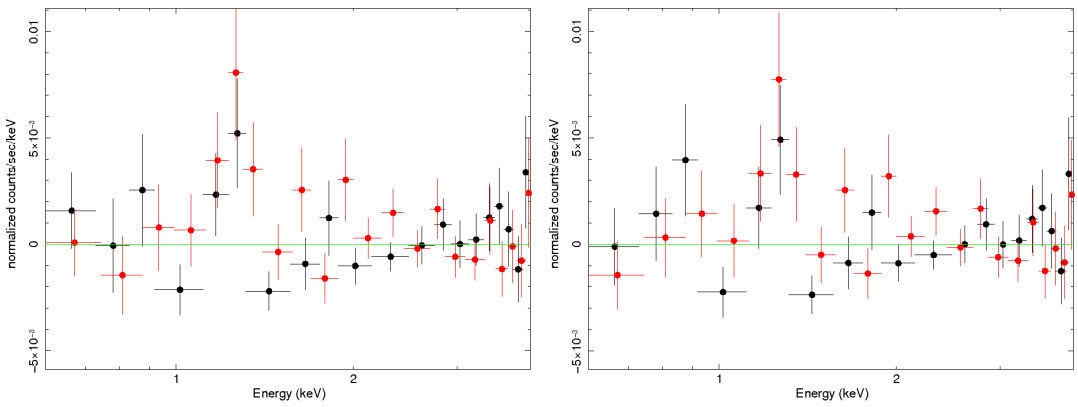

Figure 3.4 Residuals corresponding to the two different soft excess models tested: two mekal (*left panel*) and a scattered power law (*right panel*).

Table 3.3 *XMM–Newton* EPIC pn best–fit parameters. Normalizations n are expressed in cm^{-2} s^{-1} keV^{-1}; the normalization of the iron line is expressed in photons cm^{-2} s^{-1}.

Γ	$1.69^{+0.18}_{-0.10}$
R	$2.7^{+0.81}_{-0.60}$
N_G	(3.06×10^{20}) cm^{-2}
N_H	$(7.14^{+1.75}_{-1.21}) \times 10^{23}$ cm^{-2}
n	$(1.83^{+0.47}_{-0.31}) \times 10^{-3}$
$n_{unobscured}$	$(8.1^{+4.08}_{-7.28}) \times 10^{-6}$
E_{Fe} (keV)	$6.40^{+0.13}_{-0.08}$
F_{Fe}	$(3.65^{+3.93}_{-2.04}) \times 10^{-5}$
EW (eV)	206^{+199}_{-115}
χ^2(d.o.f)	37.5(37)
Unabsorbed luminosity and absorbed flux	
$L_{0.5-2\ keV}$ (erg s^{-1})	$5.12\ \times10^{41}$
$L_{2-10\ keV}$ (erg s^{-1})	7.53×10^{43}
$Flux_{0.5-2\ keV}$ (erg s^{-1} cm^{-2})	$6.30\ \times10^{-14}$
$Flux_{2-10\ keV}$ (erg s^{-1} cm^{-2})	$2.64\ \times10^{-12}$

Table 3.4 Emission lines detected in the *XMM–Newton* EPIC pn spectrum. E_c is the centroid line energy (keV) in the source rest frame; F is the line flux in units of 10^{-6} photons cm^{-2} s^{-1}; P_F is the significance of the fit improvement after including the Gaussian line in the model, based on the F–test.

Energy	*Intensity*	P_F	*Tentative IDs*
0.71±0.03	$7.89^{+2.8}_{-4.6}$	$> 99.8\%$	OVII RRC, Fe XVII 3s-2p
$0.93^{+0.03}_{-0.05}$	$5.23^{+3.1}_{-4.8}$	$> 99\%$	Ne IX rif
$1.26^{+0.04}_{-0.17}$	2.35±2.2	$> 88\%$	Mg XI Heα

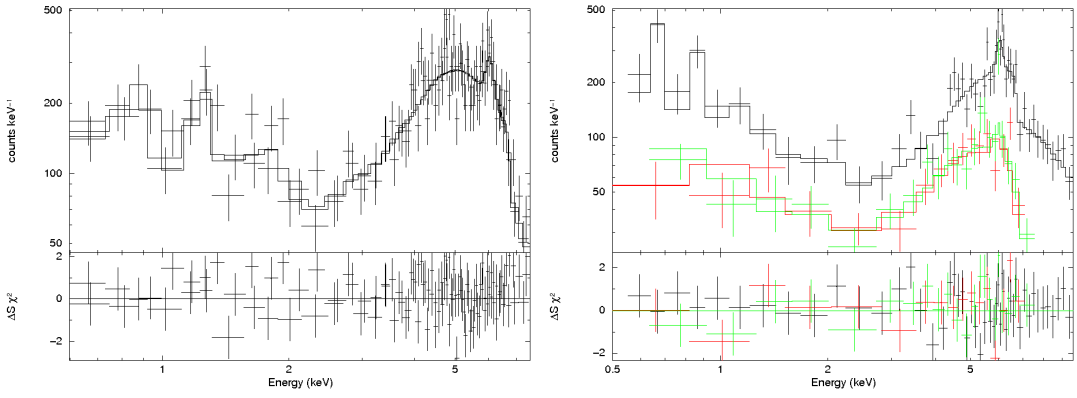

Figure 3.5 *Chandra* (*left panel*) and *XMM–Newton* (*right panel*) spectra of 3C 33. pn, MOS 1 and MOS 2 spectra are represented with *black*, *red* and *green* crosses, respectively. Residuals are in terms of standard deviations of the observed data from the model.

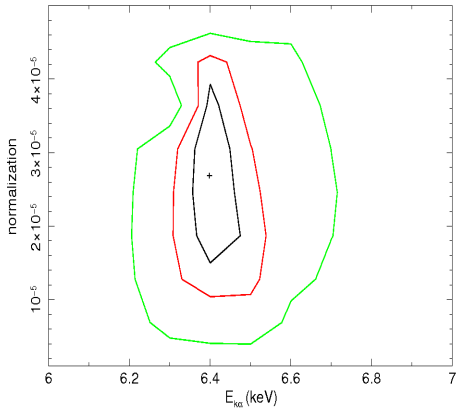

Figure 3.6 Contours plot for normalization versus centroid energy of Fe Kα line as measured in the *XMM–Newton* data. The curves define the 68%, 90% and 99% confidence intervals for two interesting parameters.

3.1.4 Results

The analysis performed on 3C 33 displays typical features produced by cold circumnuclear gas: an unresolved ($\sigma < 180$ eV) narrow iron line (EW $\simeq$ 200 eV) and a reflection component (R $\simeq$ 2) (Risaliti 2002), showing the Seyfert 2 nature of the hard spectrum of 3C 33. Both these values are consistent with the *Chandra* results of Kraft et al. 2007 (their Model 1).

The reflection component was obtained assuming an arbitrarily inclination angle of $\theta \simeq 60°$ ($\cos\theta \simeq 0.45$). However even considering a larger inclination angle, as suggested by the radio data, the value of R does not significantly change. This is not surprising as the limited statistics and the large number of parameters required by the fit. Although the reflection component is slightly higher than that expected from an homogeneous dusty torus, it is not unusual and often observed in radio–quiet obscured objects. This probably indicates the presence of a more complex inhomogeneous and structured circumnuclear absorber (Risaliti et al. 2002). In a successive paper presenting *Suzaku* data, Evans et al. (2010) did not find neither signatures of reflection nor the Compton hump above 10 keV, but only measured an upper limit to the neutral reflection fraction R<0.41. However this measure was obtained by fixing the high energy cutoff of the incident power law at 1 GeV.

The spectral analogy between Seyfert 2s and obscured radio galaxies seems to be maintained at soft X–ray energies, where the best fit model requires emission lines overimposed on a weak continuum. Lines in Tab. 3.2 and 3.4 are reliably produced by H– and He–like ions of light elements such as Oxygen and Neon, often detected in obscured AGNs, showing strong evidence of photoionized gas (Bianchi & Guainazzi 2007; Grandi et al. 2007; Sambruna et al. 2007; Piconcelli et al. 2008). Although the moderate ACIS and EPIC energy resolutions do not allow to draw strong conclusions, we stress that the centroid of the lines occurs where two strong features produced by photoionized gas are expected, i.e. the OVII (RRC) and the Ne IX triplet. Combining *Chandra*, *XMM–Newton* and *Suzaku* data (Fig. 3.7), Evans et al. (2010) found hints of He–like species of O VII and Mg XI giving support to our interpretation. Incidentally we note that the intrinsic nuclear luminosity of 3C 33 ($L_{1-1000ryd}$ $\sim$2$\times10^{44}$ erg sec^{-1}) is comparable to those observed in typical Seyfert 2s, for which the higher quality of the data allowed detailed spectral studies of the soft X–ray diagnostics (see, for example, Pounds & Page 2005; Sako et al. 2000ab). Approximate computations indicate that the energy budget of the AGN is sufficient to produce a range of values of the ionization parameter, ξ, consistent with the photoionized scenario (Kinkhabwala et al. 2002). If the soft X–ray emission is related to the Narrow Line Region (as in Seyfert 2s), assuming a minimum (R_{min} $\sim$1 pc) and a maximum (R_{max} $\sim$2 kpc, the nuclear extraction region) distance of the gas, a typical NLR electron density n_e $\sim10^3$ cm^{-3} implies logξ spanning between -2 and 4 erg cm s^{-1}.

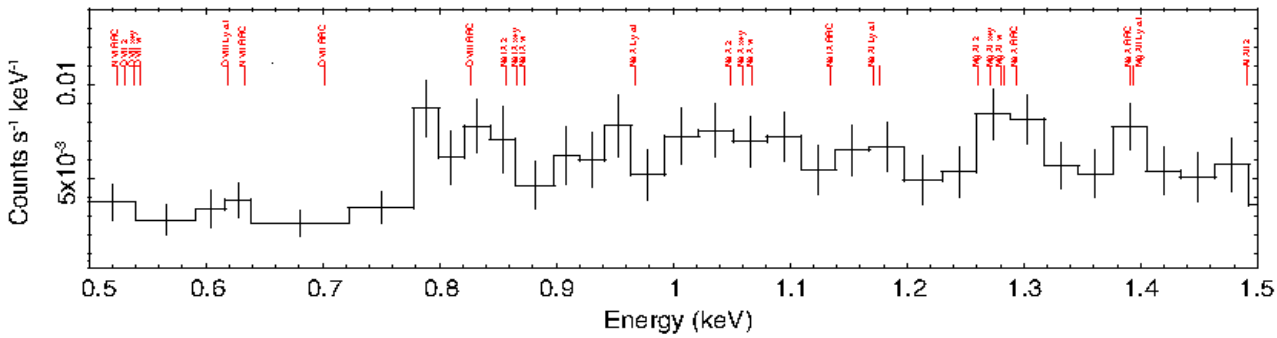

Figure 3.7 Combined *Chandra*, *XMM–Newton* and *Suzaku* spectrum of 3C 33 in the energy range 0.5–1.5 keV from Evans et al. (2010). The spectral transitions produced by the photoionized plasma in the Seyfert 2 galaxy NGC 1068 are reported as an example.

3.1.5 The origin of the soft X–ray emission

X–ray spectroscopy provides evidence for the presence of soft X–ray emission lines in the radio galaxy 3C 33.

In spite of the limited spectral power of the ACIS and EPIC cameras features that are plausibly emitted by a photoionized gas could be detected (see Tab. 3.2 and Tab. 3.4).

The analogy with Seyfert 2 galaxies is straightforward. Narrow Line Radio Galaxies would share similar continua and environments with their RQ counterparts. In Seyfert 2 galaxies the coincidence in morphology and dimension of the soft X–ray and the [OIII]λ5007 emission suggests the Narrow Line Region as the location of such gas. It is then natural to search for a similar X–ray and optical spatial correlation in 3C 33.

For this reason the narrow–band HST ACS/WFC1 optical image, centered at redshifted [OIII]λ5007 (filter FR551N), was retrieved from the Multi Mission Archive at STScI (MAST) [1] and was aligned with the *Chandra* image as described in Bianchi, Guainazzi & Chiaberge (2006).

Fig. 3.8 shows the *Chandra* soft X–ray contours (< 2 keV) superimposed on the *HST* [OIII]λ5007 image. The coincidence in extension and morphology between the

[1] `http://archive.stsci.edu/`

two emissions is impressive.

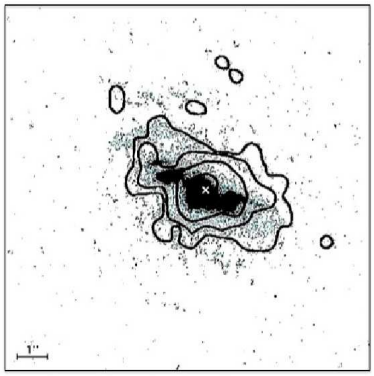

Figure 3.8 Superposition of the *Chandra* soft X-ray (<2 keV) contours on an *HST* image taken through a linear ramp filter at redshifted [OIII]λ5007. The sign "x" indicates the centre of the hard X–ray source, north is up, east to the left. The X–ray image was smoothed with a Gaussian of FWHM $\sim$ 6 pixels. The contours correspond to four logarithmic intervals in the range 1-60% of the peak flux.

Further support in favor of the photoionization scenario comes from optical spectroscopy.

Several line diagnostic diagrams have been proposed to discriminate between collisionally ionized plasma (e.g. starburst emission) and photoionized plasma irradiated by a central engine (see for example Miller et al. 2003). One of these, based on the [OIII]/Hβ and [NII]/Hα ratios (Fig. 3.9) could be used to test the nature of the gas emission of 3C 33. Using the nuclear reddening-corrected emission line luminosities reported by Koski (1978) we estimated log([OIII]/Hβ)$\sim$ 1.1 and log([NII]/Hα)$\sim$ -0.17. Such values place 3C 33 in the region populated by the photoionized AGNs.

Baum et al. (1992) performed an accurate study of the extended kpc emission–line region (EELR). They also found a large value of [OIII]/Hβ ratio that they interpreted as produced by photoionized gas with a high ionization parameter.

On the other hand, Baum & Heckman (1989) have already demonstrated that the number of photons needed to photoionize the emission–line nebula of this source equals the number of ionizing photons coming from the central engine.

In addition, on the basis of the kinematic classification of powerful radio galaxies proposed by Baum et al. (1992), 3C 33 belongs to the *rotator* class. Rotators, characterized by a systematic gradient in the velocity of the emission–line gas, are

nearly always associated with powerful radio sources ($L_{radio} \geq 10^{42}$ erg s^{-1}) having luminous high–ionization nuclear emission–line region.
The kinematic study of the gas also shows that the gas rotation axis and the radio axis are aligned within 10° (Baum et al. 1992). Moreover the rotation axis of the gas is not aligned with the stellar rotation axis (Heckman et al. 1985), disfavoring the hypothesis of a collisional (starburst) gas emission.

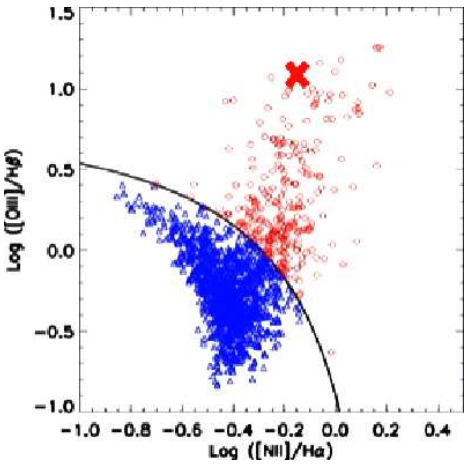

Figure 3.9 Line diagnostic diagram from Miller et al. (2003). It is used to differentiate AGNs (*red circles*) from star–forming galaxies (*blue triangles*). The solid line represents the 1σ lower limit of the model from Kewley et al. (2001). The estimated values log([OIII]/Hβ)$\sim$ 1.1 and log([NII]/Hα)$\sim$ -0.17 from Koski (1978) place 3C 33 largely in the AGN region (*red cross*).

3.1.6 Summary

The X–ray analysis of the Narrow Line Radio Galaxy 3C 33 confirms the Seyfert 2 nature of this source. In agreement with previous works the complexity of the broad–band spectrum, largely dominated by strong obscuration ($N_H \sim 10^{23}$ cm^{-2}), is confirmed.
A prominent Fe Kα line at 6.4 keV is also present. Its EW of $\sim$ 200 eV is in agreement with being produced by optically–thick circumnuclear matter (Ghisellini Haardt & Matt 1994).
The soft excess has been interpreted as emitting gas photoionized by the central engine. There are several clues favoring this hypothesis. First of all both *Chandra* and *XMM–Newton* soft X–ray spectra can be better fit with an unobscured scattered

power law plus highly ionized lines, rather than with one or more thermal components. Next, a rough estimate of the ionization parameter ξ, expected in the case that the emitting line gas is located in the NLR, is consistent with a photoionized scenario, and finally there is a remarkable spatial coincidence between the extended soft X–ray and the [OIII]λ5007 emission.

X–ray findings are also consistent with pieces of evidence coming from other wavelengths. The optical line ratios [OIII]/Hβ and [NII]/Hα put 3C 33 among the AGNs, far away from the region populated by starburst galaxies in the diagnostic plane of Miller et al. (2003). The extended kpc emission line region has a line–rich optical spectrum with large [OIII]/$H\beta$ ratio, typical of photoionized gas. Moreover the estimated photons required to photoionize the emission–line nebula (in the optical band) are provided entirely by the nuclear engine.

The kinematical properties of the extended gas of 3C 33, based on optical spectroscopy, are typical of powerful radio galaxies with high–ionization nuclear emission. The gas rotation axis and the radio axis are aligned within 10°, but the former is not aligned with the stellar rotation axis.

All together these results seem to draw a photoionized scenario for the circumnuclear environment implying that radiative processes are still at work on kpc distances and could compete with the jet kinetic power (see Chapter 5). Another important implication is that RL and RQ AGNs seem to share similar environment properties and consequently, similar accretion mechanisms can be present in high–luminosity AGNs, indipendently on the presence/absence of powerful extended jets.

4

Warm photoionized gas in absorption

4.1 Introduction

The first suggestion of an X–ray warm absorber (WA), i.e., absorption by ionized gas in our line–of–sight, was made by Halpern (1984) with the *EXOSAT* satellite on the QSO MR2251–158. It is now well established that at least half of all Seyfert 1s is characterized by photoionized warm absorption (Blustin et a. 2005; McKernan et al. 2007). High–resolution spectroscopic data (RGS, HETG, LETG) dramatically improved our knowledge of WAs. The application of detailed photoionized codes (see next Section) revealed that quite often the gas is stratified, with a wide range in ionization parameter ξ (see Chapter 2) and column densities, ranging between 10^{20-23} cm^{-2}, with velocities of the order of a few hundreds to thousands km s^{-1} (Blustin et al. 2005; McKernan et al. 2007). Where these winds originate and are powered is still an open question. Several regions at different distances from the central engine, like the NLR, the obscuring torus and the accretion disk have been proposed as a possible location for the gas (Crenshaw et al. 2003; Krolik & Kriss 2001; Proga & Kallman 2004).

As discussed in Chapter 5, soft X–ray WAs in Seyferts have kinetic luminosities that account for less than 1% the bolometric luminosity (Blustin et al. 2005). Therefore, it seems that they are not playing a fundamental role in the general picture of the AGN feedback. The situation changes when extreme WAs are considered. These

outflows can reach velocities of ∼0.1c–0.3c, and consequently their kinetic luminosities can compete with the accretion luminosities. Such winds could represent a driving mechanism for the feedback processes (Gofford et al. 2011 and references therein).

If the presence of X–ray absorbing gas is well established in Seyfert 1s, for RL AGNs the investigation of the nuclear environment through high–resolution spectroscopy has just started. Therefore, detections of WAs in type 1 objects, i.e., BLRGs, are still a handful. BLRGs are complex objects. The Doppler amplification of the jet emission can play a key role in dimming the spectral features. For example, RGs are known to have weaker Compton reflection signatures and weaker Fe Kα lines when compared to Seyfert 1s (Grandi, Malaguti & Fiocchi 2006 and references therein). Up to now, controversial hints of WAs have been observed in the past in a handful of RL sources: 3C 382 and 3C 390.3 with *ASCA* (Reynolds 1997); 3C 351 with *ROSAT* PSPC (Nicastro et al. 1999); 4C+74.26 with the *XMM–Newton* EPIC cameras (Ballantyne 2005).
It is unclear whether winds can form and/or survive in the nuclear regions of RL AGNs, where large amounts of the gravitational power is funneled into relativistic collimated plasma. Addressing this point is fundamental to clarify the physical link among accretion flows, winds and jet, and the influence that each of these components can have on the host galaxy.

4.2 Warm absorber modelling

To understand the physical properties of a warm absorbing gas, plasma codes that calculate the output spectrum from a cloud of photoionized gas, are required. There are several plasma codes available, such as XSTAR [1], SPEX [2], CLOUDY [3], Titan [4], Mocassin [5].
In this thesis I concentrate on XSTAR and SPEX. In particular, the first one is used to model the 3C 382 WA, while the latter is employed in fitting 3C 390.3 and 3C 120 RGS spectra.

[1] http://heasarc.nasa.gov/lheasoft/xstar/xstar.html
[2] http://www.sron.nl/spex
[3] http://www.nublado.org
[4] http://Vo.obspm.fr/simulation
[5] http://hea-www.harvard.edu/ bercolano

XSTAR (Bautista & Kallman 2001) calculates the physical conditions and spectra of photoionized gases. basically, it computes the effects of a spherical gas shell surrounding a central source of radiation that re–radiates it in other portions of the spectrum. The output grids contain absorption, emission and continuum spectra.

SPEX (Kaastra, Mewe & Nieuwenhuijzen 1996) is a fitting package for X–ray spectral analysis, particularly suited for high–resolution spectroscopy. To fit the photoionized absorption I use the *xabs* component, which calculates the transmission of a slab of material where all ionic column densities are tied through a photoionization model. The ionization parameter, ξ, and the column density, N_H, are free parameters, but, in addition, also the outflow velocity, the abundance and covering factor can be potentially free parameters.

4.3 First evidence of a warm absorber in the BLRG 3C 382

4.3.1 Introduction

3C 382 is a nearby radio galaxy (z=0.0579), with lobe-dominated FRII radio morphology. It exhibits a long jet extending north–east of the core for 1.68' and two radio lobes, with a total extension of 3' (Black et al. 1992).
At optical wavelengths 3C 382 shows strong and broad lines (FWZI>25,000 km s^{-1}), which are variable on timescales of months to years. An *Hubble Space Telescope (HST)* WFPC2 image showed that this source is an elliptical galaxy strongly dominated by an unresolved nucleus (Martel et al. 1999). The optical emission of this source is clearly photoionized as can be inferred from the de-reddened line ratios, i.e., log[OIII]/Hβ=0.90 and log[NII]/Hα=0.17 (Buttiglione et al. 2009), compared with the diagnostic diagrams of Miller et al. (2003) (Fig.4.1).
In the X–ray band 3C 382 is a bright source ($F_{2-10keV} \sim 3\times10^{-11}$ erg cm^{-2} s^{-1}). The 2–10 keV spectrum is well fitted with a single power law; when the fit is extrapolated to lower energies a strong soft–excess is observed (Prieto 2000; Grandi et al. 2001). *ROSAT/HRI* observations revealed extended X–ray (0.2–2.4 keV) emission around 3C 382 (Prieto 2000), that was confirmed by the spatial resolved study of Gliozzi et al. (2007). However, as discussed by Grandi et al. (2001) and Gliozzi et al. (2007) the extended thermal emission cannot account for the observed soft–excess, which must be instead of nuclear origin.

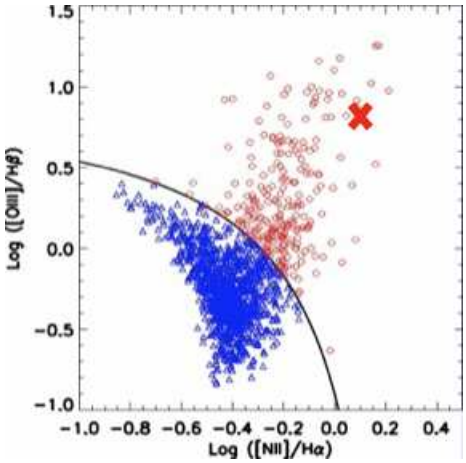

Figure 4.1 Line diagnostic diagram from Miller et al. (2003) already reproted in Section 3.1.5. The *red cross* refers to 3C 382, whose optical emission is clearly photoionized as inferred from the de–reddened line ratios log[OIII]/Hβ=0.90 and log[NII]/Hα=0.17.

4.3.2 Observation and data reduction

3C 382 was observed by *XMM-Newton* on 2008 April 8 (OBSID: 0506120101) for about 40 ks. The data from EPIC (Strüder et al. 2001), RGS (den Herder et al. 2001) and Optical Monitor (OM, Mason et al. 2001) instruments were operating. The aim is searching for warm absorber features, thus only the RGS data (6–38 $\AA$) have been analyzed. Data were processed with the task *rgsproc* of the SAS 8.0.0, which combines the event lists from all RGS CCD, produces source and background spectra using standard extraction regions, and generates response matrices. The background is estimated taking into account events from a region spatially offset from the source.

4.3.3 RGS data analysis

The first–order unbinned spectra from the two RGS cameras were simultaneously fitted in XSPEC using the C-statistic (Cash 1979). The quoted errors correspond to 90% confidence level (ΔC=2.71) for one interesting parameter.

The 6–35 $\AA$ (0.35–2 keV) continuum is well fitted by a single absorbed power law with $\Gamma = 2.25 \pm 0.18$ (C=5264 for 4636 d.o.f.). A quite steep power law is not unexpected in this source known to have a strong soft excess. It was investigated whether an extended thermal component (APEC) is required by the data, as sug-

Table 4.1 Soft X-ray absorption and emission lines detected in the RGS spectrum of 3C 382. Columns: (1) Identification of the transition; (2) 3C 382 rest–frame wavelength (in $\mathring{A}$); (3) Laboratory wavelength (in $\mathring{A}$); (4) Emission–line intensity; (5) Equivalent width (in m$\mathring{A}$); (6) ΔC.

Transition	λ(rest)	λ(lab)	Flux	EW$^{(a)}$	ΔC $^{(b)}$
-	($\mathring{A}$)	($\mathring{A}$)	(10^{-5}photons cm^{-2} s^{-1})	(m$\mathring{A}$)	-
NeX	12.07	12.13	-	67^{+34}_{-30}	ΔC=7
FeXX	12.78	12.82	-	43^{+31}_{-30}	ΔC=8
OVIII Lyα	18.90	18.97	-	24^{+12}_{-10}	ΔC=11
OVIII Lyα(em)	18.99	18.97	$4.70^{+3.86}_{-3.32}$	-23^{+16}_{-18}	ΔC=6

(a) Errors are at the 90% confidence level for one interesting parameter.
(b) Improvement in the C-statistic (Cash 1979) for adding a Gaussian line with two free parameters to a power law model.

gested by the *Chandra* analysis. The fit did not improve significantly, nor did the shape of the residuals (C=5261), therefore it is not included.

At first a phenomenological approach was adopted. The spectra were divided into a number of regions containing about the same number of bins each (100). An accurate inspection of every single region was performed. Where the spectra showed a particularly evident absorption feature, a Gaussian profile with 0–width and a negative normalization was added to the model. Only lines yielding an improvement in the fit higher than ΔC>5 (corresponding to $> 95\%$ for two interesting parameters) were taken into account. For these structures the equivalent width was estimated and the corresponding atomic transition identified through several atomic databases such as CHIANTI (Dere et al. 1997; Landi et al. 2006), ATOMDB WebGUIDE [6] and NIST [7]. The parameters of the most prominent lines are reported in Table 4.1 and the phenomenological fit is shown in Fig.4.2. Two other absorption lines probably corresponding to FeXXI/MgXI and SIV/NVII transitions, although observed, are not reported in Table 4.1 because of their marginal detection (ΔC =5). None of the detected features is due to local (Galactic) absorption.

Finally, an emission line identified as OVIII Lyα was clearly detected with ΔC=6 (see Table 4.1). Emission features are often observed in sources showing signatures of warm absorber (Blustin et al. 2002; Turner et al. 2004).

Once the presence of absorption lines was ascertained via the phenomenological analysis, the next step was to study the physical properties of the gas using a self consistent modeling of the spectrum. Extensive simulations were carried out using the photoionization code XSTAR (v2.1ln9). The output was a grid of models (afterwards simply called XSTAR model) that can be fitted to the data in XSPEC. Each model in the grid represents a photoionized spectrum characterized by a particular value of the column density and the ionization parameter. The explored parameter range is N_H=[10^{18}, 10^{23}] and logξ=[-3, 3]. A simple spherical geometry for the illuminated gas (covering factor =1), solar abundances (Grevesse & Sauval 1998) , and an illuminating continuum from 1 to 1000 Rydbergs derived from the intrinsic spectral energy distribution SED of the source (Fig.4.3 and Tab. 5.1) were assumed. The turbulent velocity of the gas was set to v_{turb}=100 km s^{-1}, as the limited RGS statistics did not allow to constrain the intrinsic width of the absorption features.

The XSTAR model obtained from these simulations was applied as an XSPEC multiplicative component to the power law and fitted to the data. The fit signifi-

[6] http://cxc.harvard.edu/atomdb/WebGUIDE/index.html
[7] http://physics.nist.gov

cantly improved (ΔC=160), as XSTAR can take into account any possible absorption feature in the spectrum. Note that the photon index is completely consistent with the one obtained from a power law only fit. The presence of a highly ionized gas phase is confirmed, indeed the the best fit required a high ionization parameter logξ=$2.69^{+0.05}_{-0.03}$ erg cm s^{-1} and a column density N$_H$=$3.19^{+1.15}_{-0.79}$ $\times 10^{22}$ cm^{-2}. The robustness of these results is attested by the N$_H$- logξ confidence contours (68% 90% 99%) shown in Fig.4.4. It was attempted to estimate the gas outflow velocities by measuring the line shifts between theoretical and observed values of the energy centroid allowing the redshift parameter (z) of the XSTAR model to vary. Reasonable outflow speeds of the order of -1200^{+180}_{-200} km s^{-1} were found, consistent with typical outflow velocities in Seyfert 1s (Blustin et al. 2002; Blustin et al. 2005) when the absorption gas is seen along the line–of–sight. Incidentally, the phenomenogical identifications proposed in Table 4.1 are confirmed by the XSTAR model (see Fig.4.5).

The energy centroid of the OVIII Lyα emission line does not require any blueshift (although with large uncertainties). However it may suggest that, contrary to the absorption lines observed along the line–of–sight, the emission comes from an extended region around the source, maybe a shell, expanding in all directions.

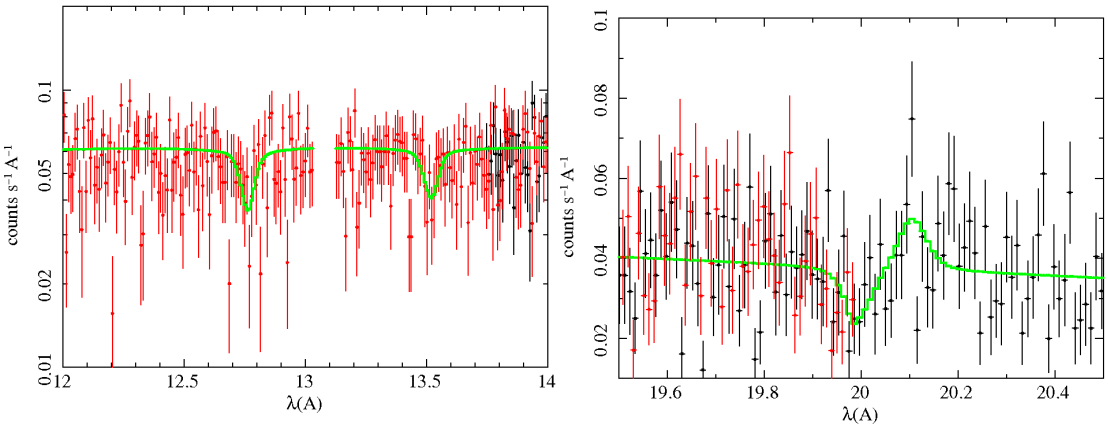

Figure 4.2 Zoom of the 3C 382 RGS observed–frame spectra (*black*: RGS1; *red*: RGS2), in wavelength ranges, around the detected absorption and emission lines. The identified lines are: NeX–FeXX (*left panel*), OVIII Lyα in emission and absorption (*right panel*). The *green* line is the best fit phenomenological model (see Table 4.1).

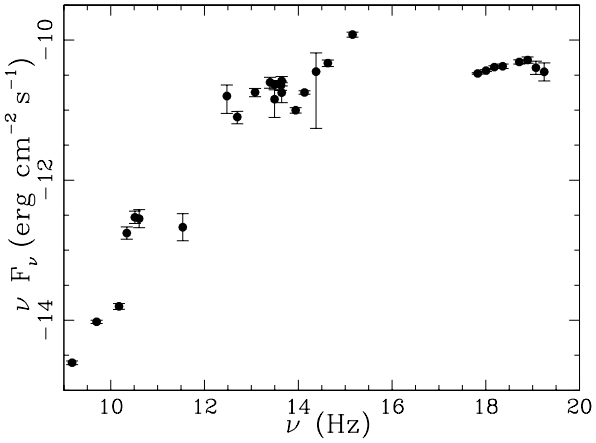

Figure 4.3 Radio to X–ray spectral energy distribution of 3C 382. Data are from literature (Rudnick et al. 1986; Knapp et al. 1990; Klavel et al. 2000; Lilly & Longair 1982; Chiaberge et al. 2000; Chiaberge et al. 2002; Grandi et al. 2001; Quillen et al. 2003; Ramos Almeida et al. 2007; Hinshaw et al. 2007). Optical and UV measurements de–reddened with the extinction curve of Cardelli et al. (1989). The visual extinction is deduced by the Galactic column density, assuming the gas–to–dust ratio from Shull et al. (1985).

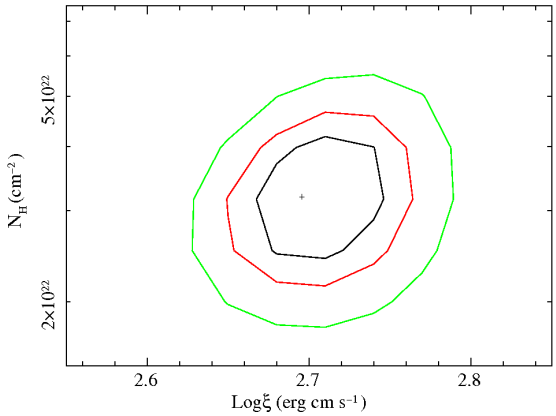

Figure 4.4 Contour plots for column density and ionization parameter values of the 3C 382 warm absorber as obtained with the XSTAR model. The curves define the 68%, 90% and 99% confidence intervals for two interesting parameters.

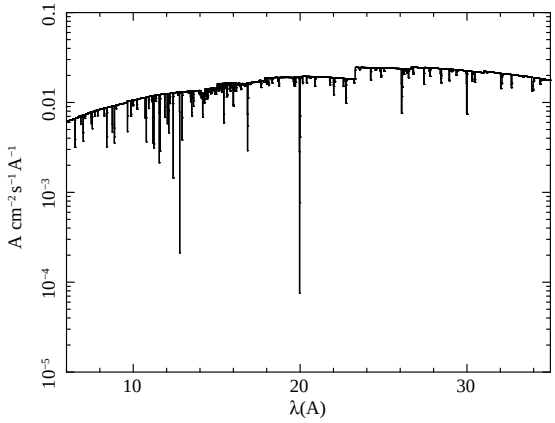

Figure 4.5 Best fit rest–frame XSTAR model of 3C 382 in the overall RGS band (6–35 $\mathring{A}$) corresponding to N_H=$3.19^{+1.15}_{-0.79}$ $\times 10^{22}$ cm^{-2} and logξ=$2.69^{+0.05}_{-0.03}$ erg cm s^{-1}.

4.3.4 Localization of the warm absorber

In order to localize the warm absorber the minimum and maximum distance for the gas were estimated following Blustin et al. (2005). The minimum distance of the WA (r_{min}) from the central engine is measured from:

$$R \geq \frac{2GM}{v_{out}}^2 \tag{4.1}$$

where M is the black hole mass and v_{out} is the measured outflow speed. The maximum distance can be estimated assuming that most of the mass of the absorber is concentrated in a thin layer ΔR where ΔR/R$\leq$1. Being N_H a function of the density n(R) of the material at ionization parameter ξ, of its volume filling factor (here assumed equal to 1) and ΔR:

$$N_H \sim n(R)\Delta R C_v \tag{4.2}$$

that combined with the expression of the ionization parameter gives

$$\frac{\Delta R}{R} \sim \frac{\xi R N_H}{L_{ion}} \tag{4.3}$$

Therefore if ΔR/R$\leq$1

$$R \leq \frac{L_{ion}}{\xi N_{H_1}} \tag{4.4}$$

The BLR radius can be calculated as (Ghisellini & Tavecchio 2008):

$$R_{BLR} = 10^{17} L_{disk,45}^{1/2} \mathrm{cm} \tag{4.5}$$

and the torus radius as (Cleary et al. 2007):

$$R_{torus} = 2.5 \times 10^{18} L_{disk,45}^{1/2} \mathrm{cm} \tag{4.6}$$

For 3C 382 it was possible to estimate the location of the gas between 10 and 60 pc. Given the BLR and torus radii as R_{BLR} $\simeq$0.06 pc and R_{torus} $\simeq$1.5 pc if $L_{disk} \sim L_{ion}$ (see Table 5.2), these results suggest that the bulk of the highly ionized absorption gas, detected in 3C 382, is located beyond the torus, most likely in the NLR. Interestingly, this is also the probable location of the photoionized emitting gas observed in 3C 33 (Chapter 3). However, the estimation of the maximum distance of the absorber depends also on the volume filling factor, thus for smaller values of C_v the distance of the gas reduces (see Chapter 5). A re–analysis of the HETG data of 3C 382 (Reeves et al. 2009) confirmed these results.

4.3.5 Summary

The high–resolution analysis of the BLRG 3C 382 has revealed that relativistic collimated plasma and slower outflows of photoionized gas can coexist in the same object. The outflowing gas is found in a hot phase as attested by the derived ionization parameter logξ=2.69 erg cm s^{-1} deduced from XSTAR simulations. Most of the light elements are indeed completely ionized, and the strongest absorption features correspond to H–like elements and L–shell iron states. In Seyfert 1s warm absorbers are complex and multi–phase, often indicating that layers of gas at different ionization states are part of the same outflow (Blustin et al. 2005). In the present case, only one zone of hot gas was observed, without apparent traces of a colder component. Nonetheless, the physical conditions of the gas in 3C 382 warm absorber are quite similar to those measured in the highest ionized absorber in their radio–quiet counterparts (NGC 4051, Krongold et al. 2007; Mkr 279, Costantini et al. 2007; IRAS13349+2438, Sako et al. 2001). Taking into account the short exposure time and the very simple assumptions in the XSTAR model, the result appears encouraging. It is worth noting that setting v_{turb} to an *a priori* fixed value could potentially overpredict the column density if the real turbulent velocity is larger. Interestingly, also the EWs of the absorption lines detected in 3C 382 are

consistent with those generally measured in Seyfert 1s (Yaqoob et al. 2003; Turner et al. 2004). This similarity suggests a negligible jet contribution to the soft X–ray spectrum, although the large uncertainties in EW prevent more quantitative statements from being made.

4.4 Warm Absorbers in other BLRGs

4.4.1 Introduction

After the results of 3C 382, that confirm for the first time the presence of absorption features in a RL AGN, I turned my attention to other BLRGs. The aim was to check if warm absorbers are typical stuctures of RL AGNs as it occurs Seyfert 1s. In particular I focussed on 3C 390.3 and 3C 120, the only two BLRGs with available data in the public archives, with exposure time long enough (t_{exp} ∼50 ks) to allow the analysis of the RGS spectra.

3C 390.3 (z=0.0561; Hewitt & Burbidge 1991) is a classical double–lobed FRII radio galaxy (Pearson & Readhead 1988). It is one of the closest radio sources whose core exhibits superluminal motion in the pc–scale jet (Alef et al. 1996). From the apparent velocity of 3.5c and the core dominance, Giovannini et al. (2001) estimated a jet inclination angle $30° < \theta < 35°$ with β ∼0.96–0.99. Double–peaked emission lines characterize the otpical and UV spectra of the source (Eracleous & Halpern 1994; Zheng 1996; Wamsteker et al. 1997), while the UV bump is weak or even absent (Wamsteker et al. 1997). 3C 390.3 is known to be variable in the X–ray band, with variations in both soft and hard band on timescale of weeks to months (Leighly & O'Brien 1997; Gliozzi et al. 2003). All previous X–ray telescopes observed this source. While in the hard X–ray band there is a general agreement on the presence of an iron line and reflection hump (Grandi et al. 1999; Sambruna et al. 2009), the modelization of the soft X–ray band is controversial. *Einstein–IPC* (Kruper et al. 1990) and *BeppoSAX* (Grandi et al. 1999) required an excess of column density. *EXOSAT* claimed the presence of a soft excess (Ghosh & Sondararajaperumal 1991) while Reynolds (1997) found hints of warm absorption in the *ASCA* data, successively confirmed by the detection of an absorption edge at 0.65 keV (Sambruna et al. 1999). Recently Sambruna et al. (2009) observed an emission line in the RGS spectrum associated with O VII forbidden possibly produced in the NLR.

3C 120 (z=0.033; Burbidge 1967) is classified as a FRI exhibiting a one–sided jet (Seielstad et al. 1979; Walker et al. 1987; Harris et al. 2004). The apparent transverse velocity of the jet v_{app}=5.3c, as obtained by the VLBA observation (Lister et al. 2009), implies an upper limit for the inclination angle of 21°. The optical spectrum of 3C 120 is typical of Seyfert 1 galaxies, with strong and broad emission lines, quite unusual for FRI radio sources. Reverbation mapping constrains the black hole mass to be $5.5^{+3.1}_{-2.3}\times10^7$ $M_\odot$ (Peterson et al. 2004). At UV wavelenghts, 3C 120 has a typical AGN spectrum with a strong blue bump and strong emission lines signature of a standard optically–thick geometrically–thin accretion disk (Maraschi et al. 1991). The hard X–ray spectrum is characterized by a slightly broadened iron line (EW∼100 eV) at 6.4 keV, a weak ionized line at 6.9 keV (Yaqoob & Padmanabhan 2004; Kataoka et al. 2007) and Compton reflection $\Omega/2\pi$∼0.4–0.5 (Eracleous et al. 2000; Zdziarski & Grandi 2001; Gliozzi et al. 2003; Ballantyne et al. 2004). The soft X–ray band of 3C 120 has been observed by the grating instruments onboard *Chandra* and *XMM–Newton*. In the *Chandra* High Energy Transmission Gratings (HETGs) spectrum an O VIII Lyα absorption line blueshifted by ∼ -5500 km s^{-1} was observed (McKernan et al. 2003). This feature was not revealed by the *XMM–Newton*/RGS (Ogle et al. 2005) that on the contrary shows a slighlty redshifted O VIII emission structure.

4.4.2 Data analysis

3C 390.3 was observed by *XMM–Newton*/RGS (den Herder et al. 2001) on 2004 October 8–9 for a total exposure of 50 ks and on October 17 for 20 ks.

3C 120 was pointed twice, on 2002 September 6 for 12 ks and on 2003 August 26 for 130 ks. In order to have a good S/N ratio, here only the second and longer observation is considered. The RGS1 and RGS2 spectra were extracted using the SAS V9.0 task *rgsproc*, which combines the event lists from all RGS CCD, produces source and background spectra using a region spatially offset from that containing the source, and generates response matrices. The resulting spectra were analyzed using the fitting package SPEX. The Galactic absorption was modeled with the SPEX HOT component. For all spectral models Solar elemental abundances were adopted (Anders & Grevesse 1989). For each source the proper line–of–sight Galactic column density was considered, N_H=3.5×10^{20} cm^{-2} and N_H=1.1×10^{21} cm^{-2} for 3C 390.3 and 3C 120, respectively (Kalberla et al. 2005). A slightly different cosmology was

applied in this case: H_0=71 km s^{-1} Mpc^{-1}, Ω_m=0.27, Ω_Λ=0.73 (Komatsu et al. 2009). For these values, 1" corresponds to 1.07 kpc and 0.650 kpc at the redshift of 3C 390.3 and 3C 120, respectively.
The absorption/emission features were searched for following the same procedure adopted for 3C 382, i.e.:

1. a phenomenological approach, consisting in the inspection of the (data–model/error) residuals after having fitted the continuum;

2. a physical approach, fitting the absorption features with the *xabs* model in SPEX. *xabs* calculates the transmission through a gas layer. Free parameters in this model are the outflow velocity ($v_{\rm out}$), the total hydrogen column density ($N_{\rm H}$) and the ionization parameter ξ (see Section 4.1). In the model the column densities of different ions are linked through an ionization balance, which is precalculated using Cloudy (Ferland et al. 1998). The ionization balance is dependent on the spectral energy distribution (SED) of the source. The SED for both 3C 120 and 3C 390.3 has been constructed starting from the broad band EPIC spectrum, which was fitted using an absorbed phenomenological model. For 3C 120 a broken power law was used to describe the data ($\Gamma_1 = 2.04$, $\Gamma_2 = 1.75$ with a break at 2.5 keV). A simple power law was sufficient for 3C 390.3 ($\Gamma = 1.77$). For the purpose of contructing the SED, both continua were then unabsorbed, to obtain the true ionizing X–ray flux. For the optical/UV part of the SED the optical monitor (Mason et al. 2001) measurements were used for both 3C 120 (V and UVW1 filters) and 3C 390.3 (U, UVW1, UVM2 and UVW2 filters). The optical fluxes have been dereddened using the extinction curves of Cardelli et al. (1989), knowing the optical extinction A_V. This has been calculated following Bohlin et al. (1978) formula: $N_{\rm H} \sim A_V = 1.9 \times 10^{21}\,{\rm cm}^{-2}$ (for $R_V = 3.1$). The low energy tail of the SED (infra–red to radio) was taken as described in the standard SED used in Cloudy (Mathews & Ferland 1987).

4.4.3 3C 390.3 results

At first the continuum of both observations was modeled with a power law ($\Gamma \sim 1.9$) plus a neutral absorber ($N_H \sim 2.5 \times 10^{20}{\rm cm}^{-2}$) in addition to the Galactic one (C/d.o.f.=583/406). Although during the second pointing (Oct. 17), the source flux was about 14% lower, the spectral parameters are completely consistent. A careful

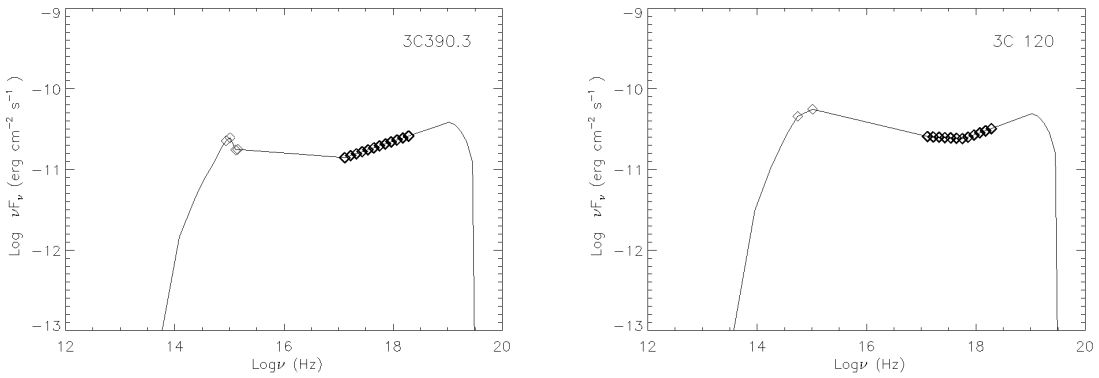

Figure 4.6 Spectral energy distributions (SEDs) of 3C 390.3 and 3C 120, constructed from the *XMM–Newton* data in the optical–UV–to–X–ray band, and from the standard AGN radio–IR continuum included in CLOUDY.

inspection of the residuals revealed photon deficits in the regions of NeX (12.134 $\mathring{A}$), FeXX (12.901 $\mathring{A}$), OVIII Lyα (18.969 $\mathring{A}$) and NVI (24.898 $\mathring{A}$). An example of an absorbed structure is shown in Fig.4.7. In order to confirm the WA detection and constrain the physical properties of the WA, the *xabs* component was added to the continuum model. The column density of the ionized absorber N_{H1}, the ionization parameter ξ, the velocity of the gas were let free to vary. The velocity dispersion between different blend components is fixed to the default value v=100 km s^{-1}. The covering fraction parameter (f_{cov}) is fixed to the default value equal to 1. The fit significantly improves with the addition of the warm absorber with respect to the power law alone (ΔC=18 and 11 for 3 additional d.o.f.) (see Table 4.2 and Fig. 4.8).

Although one–phase absorption model well describes the data, we also tested a stratified gas possibility. Actually, the inclusion of a second absorber, with a higher ionization parameter ($\xi \approx 3$) and column density ($N_{H2} \approx 1.5 \times 10^{21}$ cm^{-2}) seems to better reproduce the shape of the most prominent features. However, the statistical improvement of the fit is not significant. Finally positive residuals around 23.5 $\mathring{A}$ (observed–frame) can be noted in both data sets (Fig.4.9). In agreement with Sambruna et al. (2009), a narrow gaussian component at the theoretical wavelength of the OVII forbidden line (Table 4.3) is a good parametrization of this emission feature.

Table 4.2 Best–fitting parameters for both 3C 390.3 observations.

Obs.	Γ	N_H	N_{H1}	Logξ	v_{out}	ΔC
	-	(10^{20}cm^{-2})	(10^{20}cm^{-2})	(erg cm s^{-1})	(km s^{-1})	-
Oct. 8	1.89±0.05	2.5±0.2	$5.5^{+2.0}_{-1.7}$	$2.08^{+0.12}_{-0.07}$	<600	18
Oct. 17	1.96±0.02	3.1±0.62	$3.7^{+2.9}_{-1.9}$	$1.98^{+0.2}_{-0.08}$	<1000	11

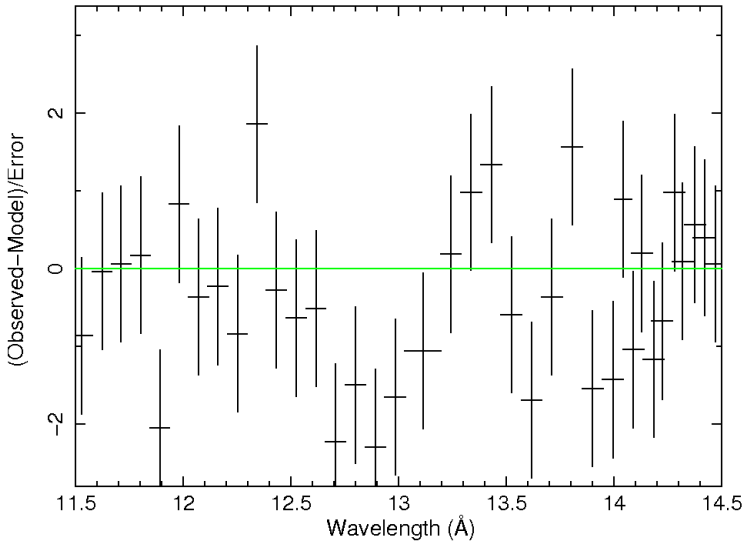

Figure 4.7 3C 390.3 residuals in a zoomed region around NeX, FeXX lines after fitting the first observation (Oct. 8) with a power law plus a neutral absorber in addition to the Galactic one.

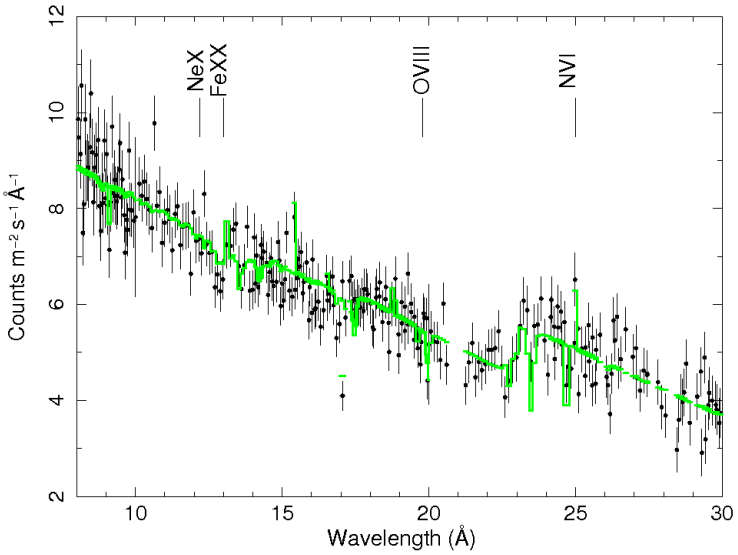

Figure 4.8 Best–fit SPEX modelling for the RGS spectrum of 3C 390.3.

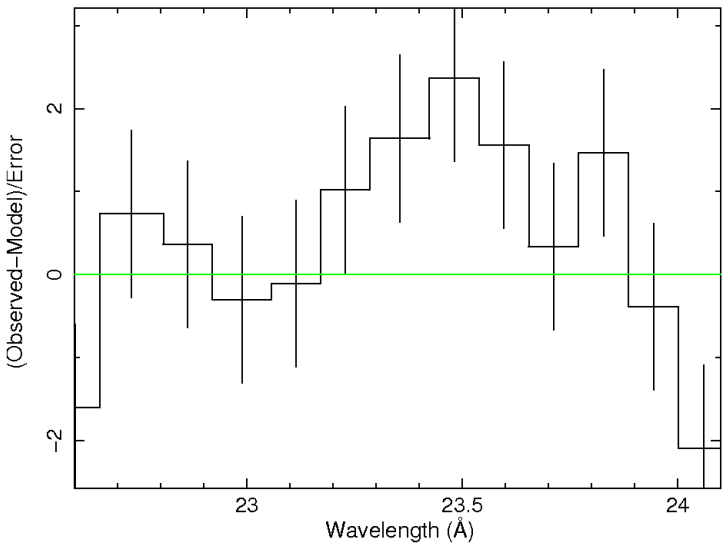

Figure 4.9 3C 390.3 residuals for the OVII forbidden line.

Table 4.3 3C 390.3 OVII(f) emission line parameters for the two epochs.

Obs.	Line	λ ($\AA$)	Flux (10^{-4} ph cm^{-2} s^{-1})	FWHM ($\AA$)	ΔC
Oct. 8	OVII(f)	22.101	$0.56^{+0.68}_{-0.26}$	$0.51^{+0.47}_{-0.23}$	13
Oct. 17	OVII(f)	22.101	$0.64^{+0.82}_{-0.24}$	$0.33^{+0.21}_{-0.12}$	17

4.4.4 3C 120 results

The soft X–ray continuum of 3C 120 is very complex. An RGS fit with a simple power law absorbed by two neutral absorbers (one local and the other one at the source rest–frame) is not a satisfying representation of the data (C/d.o.f.=803/328). The spectral shape of the continuum seems to be curved, as suggested by negative residuals around 23–26 $\AA$ that is the region where O I edge is expected. It is excluded that this spectral bending can be attributed to a warm absorber. The *xabs* model is not statistically required by the data and left the residuals invariant. Following Ogle et al. (2005) the oxygen abundance of the local absorber was allowed to vary. The fit greatly improves (C/d.o.f.=562/327) and the oxygen abundance drops to $A_{(O)}$=0.53±0.07.

However an inspection of the residuals still reveals emission features in the range 17–20 $\AA$ (Fig.4.10). These structures can be fitted with two gaussian lines at the wavelength corresponding to the rest–frame positions of Fe XVI L–shell and O VIII Lyα (see Table 4.4), providing a further improvement of the fit (C/d.o.f.=449/324). To ascertain the nature of the gas emission a single temperature collisional model, CIE (Collisional Ionization Equilibrium) in SPEX, was tested instead of two single lines. A thermal component with kT=$0.37^{+0.09}_{-0.06}$ cannot completely take into account the emission features requiring the addition of a Gaussian line in the Fe XVI L–shell energy range. The final fit (Table 4.4) is slightly better than the previous one. Although it is difficult to establish the exact nature of the emitting gas, it can be excluded that only a single temperature collisional component is sufficient to reproduce the soft excess in 3C 120.

Table 4.4 3C 120 fit parameters for the two models tested. For model 1 C/d.o.f.=449/324, for model 2 C/d.o.f.=440/324.

	Model 1	Model 2
Γ	2.32±0.04	2.32±0.04
N_H	$8.8^{+0.5}_{-0.6}$	8.8±0.7
$A_{(O)}$	0.53±0.07	$0.38^{+0.07}_{-0.08}$
$\lambda(\mathring{A})$	16.892	16.892
Flux[a]	$0.66^{+0.04}_{-0.2}$	$0.38^{+0.07}_{-0.05}$
FWHM($\mathring{A}$)	$0.27^{+0.13}_{-0.15}$	$0.13^{+0.18}_{-0.07}$
$\lambda(\mathring{A})$	18.969	–
Flux[a]	$0.18^{+0.09}_{-0.08}$	–
FWHM($\mathring{A}$)	$0.13^{+0.18}_{-0}$	–
kT(keV)	–	$0.37^{+0.09}_{-0.06}$

(a) in 10^{-4} ph cm^{-2} s^{-1}

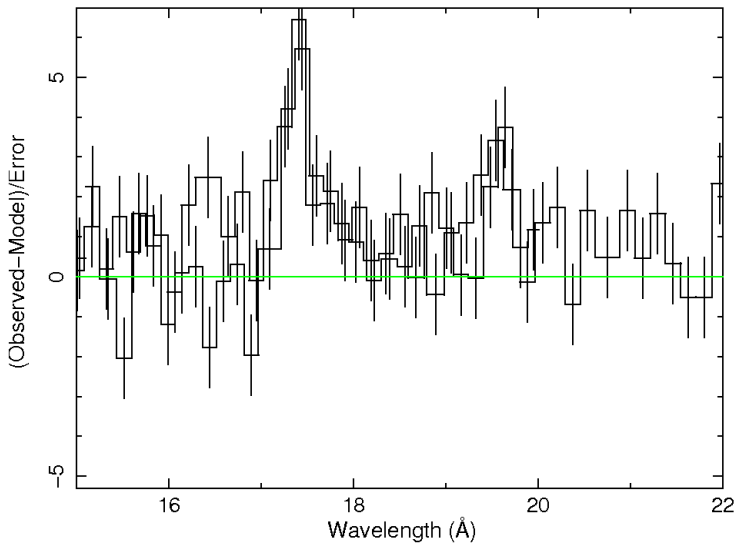

Figure 4.10 3C 120 residuals after fitting the RGS data with a power law plus two neutral absorbers, with the oxygen abundance of the neutral absorber free to vary.

5

A small sample of Broad Line Radio Galaxies

High–resolution data were collected from literature in an effort to build a sample of BLRGs sources. It consists of four sources: 3C 390.3, 3C 120, 3C 382 and 3C 445. 3C 445 is included because Reeves et al. (2010) claimed the *Chandra*/LETG detection of an outflowing and clumpy accretion disk wind, in addition to the soft X–ray emission lines.
Although small in size, the sample can help in characterizing the physical properties of the absorbing gas in AGNs able to produce powerful relativistic outflow.

The main properties of each object are reported in Table 5.1, where the redshift, the jet inclination angles, the black hole masses, the ionizing luminosities between 1—1000 Ry, and the radio luminosity at 151 MHz in units of W Hz^{-1} sr^{-1} are listed.

5.1 Warm Absorber Physical Properties

In Table 5.2 the column density, the ionization parameter, the outflow velocity, the mimimum and maximum radii of the WA are reported for each source of the sample. In order to establish the location of the emitting/absorbing region, the BLR and the torus distances are also listed (see Section 4.5 for the description of how the distances are estimated).

As expected, the absorption lines due to photoionization and photoexcitation

Table 5.1 Summary of the BLRGs properties.

	z	i (degrees)	$\log M_{BH}$[a] ($M_\odot$)	L_{ion}[b] (erg s^{-1})	L_{151MHz} (W Hz^{-1} sr^{-1})	Ref.
3C 445	0.05623	≤ 60[c]	8.33	44.47	25.23	Reeves et al. (2010)
3C 390.3	0.0561	30–35[d]	8.55	44.85	25.53	This thesis
3C 382	0.0579	35–45[d]	9.06	45.27	25.17	Torresi et al. (2010)
3C 120	0.033	≤ 21[e]	7.42	44.96	25.04	This thesis

(a) Taken from Grandi et al. (2006).
(b) L_{ion} directly measured from the proper SED of each source, except for 3C 445 taken from Reeves et al (2010).
(c) Estimate from the radio jet/counterjet ratio (Grandi et al. 2007).
(d) Estimate from the radio band (Giovannini et al. 2001).
(e) Upper limit of the inclination angle obtained by using the larger apparent transverse velocity v=5.3c (Gomez et al. 2001).

processes are preferentially observed in RGs seen at small inclination angles (i.e., 3C 382 and 3C 390.3). On the contrary, the emission lines, produced by the inverse processes, are dominant in 3C 445 (Grandi et al. 2007; Reeves et al. 2010), the only source with the jet pointed away from the observer. Note that no WA could be detected in 3C 120, the BLRG in the sample with the smallest inclination angle (i<21°) and the only one with a γ–ray counterpart discovered by *Fermi* (see Section 1.3.1). Despite of the small sample of available objects, there is evidence that the physical conditions and location of the warm gas are not always the same. The deduced high velocity ($v_{out}\sim10^4$ km s^{-1}), high column density ($N_H>10^{23}$ cm^{-2}) and low ionization parameter logξ=1.4 erg cm s^{-1} of the wind in 3C 445 indicate a probable origin in the disk (Reeves et al. 2010). On the contrary, the ionization parameters of 3C 382 and 3C 390.3 are higher, the outflows are slower and probably nearby the torus, far from the central engine. It is worth noting that the outflows have been detected with different instruments. In particular, the fast wind has been discovered analyzing the hard part of the spectrum (E>6 keV) with very long LETG exposure (200 ks). The high energy features are elusive and are not always detected. For example, a so strong edge at 7 keV in the spectrum of 3C 445 was not successively observed by *Suzaku* (Braito et al. 2011). The occasional occurrence of these events could explain the difficulty in catching them. Conversely, the presence of slow outflows in the soft X–ray band (E<2 keV) is well ascertained. This seems to suggest that, a different perspective of the same WA phenomenon can be obtained looking at different regions of the spectrum with different instruments. Hints of the multi–phase nature of the WA was also provided by the RGS analysis of 3C 390.3, where an indication of a dual absorber was found in the longer observation. This further suggests that the availability of high–resolution spectra with a high S/N ratio is mandatory to explore the complexity of the gas.

5.2 Warm Absorber Energetics in BLRGs

Table 5.3 reports the inflow and outflow mass rate ($\dot{M}_{acc}$, $\dot{M}_{out}$), the kinetic luminosity of the outflow ($\dot{E}_{out}$) and of the jet (P_{jet}), and the accretion luminosity that we assume $L_{bol}=L_{acc}=\eta\dot{M}c^2$. The mass accretion rate $\dot{M}_{acc}$ was calculated for η=0.1.

The mass outflow rate estimates how much mass is carried out through the wind, and can be expressed as:

Table 5.2 For each source the warm absorber parameters, i.e., $\log N_{H_1}$, $\log\xi$, v_{out}, together with the estimated minimum (r_{min}) and maximum (r_{max}) distance of the WA in pc, the distance of the BLR (r_{BLR}) and of the torus (r_{torus}) from the central engine, respectively, are reported.

	$\log N_H$ (cm^{-2})	$\log \xi$ (erg cm s^{-1})	v_{out} (km s^{-1})	r_{min} pc	r_{max} pc	r_{BLR} pc	r_{torus} pc
3C 445	23.3	1.4	10^4	0.01	-	0.02	0.45
3C 390.3	20.7	2.08	$<$600	$\geq$9	$\leq$450	0.02	0.7
3C 382	22.5	2.69	1000	$\geq$10	$\leq$60	0.06	1.5
3C 120	-	-	-	-	-	0.03	0.8

$$\dot{M}_{out} \sim \frac{1.23 m_p L_{ion} v C_v \Omega}{\xi} \tag{5.1}$$

The solid angle of the outflow is set to the value Ω=2.1, considering that ∼33% of the radio galaxies belonging to the 3CR sample with z≤1.5 are BLRGs (Buttiglione 2009), and assuming that at least 50% of the objects possess an outflow as in Seyfert 1s. The volume filling factor C_v being unknown, it was kept equal to 1. This implicitly assumes an upper limit for the $\dot{M}_{out}$.
The kinetic energy is the power released in the circumnuclear environment through the outflow and is expressed by:

$$\dot{E}_{out} = \frac{\dot{M}_{out} v_{out}^2}{2} \tag{5.2}$$

where v_{out} is the blueshift velocity measured for the warm absorber.

P_{jet} is calculated according to the formula of Shankar et al. (2008) adapted from Willott et al. (1999):

$$P_{jet} = 3 \times 10^{45} f^{3/2} L_{151}^{6/7} erg\ s^{-1} \tag{5.3}$$

L_{151} is the observed radio luminosity at 151 MHz, in units of 10^{28} W Hz^{-1} sr^{-1}. The factor f accounts for systematic underestimates of the true jet power. An average value <f>=15 is required for "*heavy*" jets with a dominant protonic component (Hardcastle et al. 2007) .

A comparison among the quantities reported in Tab. 5.3 suggests at least two considerations:

- the kinetic luminosity related to the slow outflows is always a negligible fraction (<1%) of both bolometric luminosity and jet kinetic power;
- if the kinetic power of the ejecting material (jets) is directly linked to the rest–mass energy of the accreting matter, i.e., the kinetic power is extracted at some time from the accretion energy, thus P_{jet} can be expressed as $P_{jet}=\eta_{jet}\dot{M}c^2$ (Shankar et al. 2008). η_{jet} expresses the fraction of accretion power that is transferred into kinetic output, i.e., it is a measure of the jet extraction efficiency. Assuming η=0.1 (typical value of standard accretion disks), η_{jet} ranges between 0.01–0.06. The gravitational power is preferentially converted in radiation rather than in kinetical power.

Table 5.3 For each BLRG we give the mass outflow rate ($\dot{M}_{out}$), the kinetic luminosity of the outflow ($\dot{E}_{out}$), the bolometric luminosity (L_{bol}; erg s^{-1}), the mass accretion rate ($\dot{M}_{acc}$) assuming η=0.1, the kinetic power of the jet (P_{jet}; erg s^{-1}) and the η_j=(P_{jet}/L_{bol})η .

	Log$\dot{M}_{out}$ ($M_\odot$ yr^{-1})	log$\dot{E}_{out}$ (erg s^{-1})	log L_{acc} (erg s^{-1})	$\dot{M}_{acc}$ ($M_\odot$ yr^{-1})	log P_{jet} (erg s^{-1})	η_j
3C 445	2.9 C_v	46.4	45.10	2[a]	44.88	0.06
3C 390.3	1.40 C_v	41.66	45.65	0.77	45.12	0.03
3C 382	1.41 C_v	41.91	45.84	1.2	44.81	0.01
3C 120	-	-	45.34	0.66	44.71	0.02

(a) The value from R10 is rescaled assuming η=0.1.

It should be noted that the kinetic power associated to the wind was neglected. $\dot{E}_{out}$ is unimportant if compared to P_{jet} when the slower outfows are considered. However, if accretion disk winds will be confirmed in BLRGs, the kinetic power of the fast outflow could become the dominant component in the energy budget, unless assuming these winds transients and/or with a covering factor (C_v) extremely small.

5.3 Comparison between radio–loud and radio–quiet WAs

In this Section I compare the BLRGs with a sample of 14 type 1 Radio Quiet AGNs (Seyferts, NLSy, and NLSyQSOs). The WAs in these objects were well studied and their properties discussed in Blustin et al. (2005).

In order to match the assumptions adopted for BLRGs, the mass outflow rates and the related kinetic powers of the RQ objects are rescaled to a volume filling factor equal to 1. The small (and of no consequence) difference between the solid

angle of BLRGs (Ω=2.1) and Seyferts/QSOs (Ω=1.6) was kept, because estimated on the basis of similar considerations. Fixing $C_v = 1$, the mass outflow rates of RQ AGNs are obviously shifted to very large (and implausible) values, with respect to those reported in Table 4 of Blustin et al. (2005). They exceed the mass accretion rates even above one order of magnitude. As shown in Fig. 5.1 (*left panel*), for BLRGs the same considerations can be drawn. In other words, the large $\dot{M}_{out}$ implies that the distribution of photoionized gas is not uniform. Indeed assuming that the same amount of matter is accreted and ejected in the form of a wind from the nuclear region, the BLRG volume filling factor should be as small as $\sim$0.01.

As already noted in the previous Section, the kinetic luminosity associated to the winds is negligible with respect to the radiative luminosity in BLRGs. Interestingly this is also true for Seyfert 1s. Note that C_v=1 provides an upper limit on the mass outflow rate estimate and, as a consequence, on the outflow kinetic luminosity (Fig. 5.1 *right panel*). There are three sources, PG 1211+143, PG 0844+349 and 3C 445, for which $\dot{E}_{out} \geq L_{bol}$. In these QSOs as well as in 3C 445 the winds have velocities of several thousands km s^{-1} and are probably directly connected to the disk (Pounds et al. 2003a,b; Reeves et al. 2010). Again it is worth noting that similar fast outflows would trasfer a large amount of mass and energy. In particular in radio galaxies, $\dot{E}_{out}$ would compete with the jet in transferring momentum to the circumnuclear environment. The jet could still prevail the wind only if very small covering factors and/or short–living phenomena are invoked.

In order to investigate the role of the jet in powerful radio sources the mass outflow rate was plotted as a function of the radio–loudness (rl). We adopted a radio–loudness defined as:

$$rl = Log(\frac{L_{1.4GHz}}{L_{2-10keV}}) \tag{5.4}$$

being the 1.4 GHz radio fluxes of type 1 RQ AGNs considered here already available in literature (Blustin & Fabian 2009).

Combining the RL and RQ information, it appears evident that both $\dot{M}_{out}$ and $\dot{E}_{out}$ increas with rl (Fig.5.2). A nonparametric statistic test results in a Pearson correlation coefficient of rs$\sim$0.7, with a significance value of 3×10^{-3} and 4×10^{-2}, for $\dot{M}_{out}$ and $\dot{E}_{out}$, respectively. The probability of correlation is larger than 95% in both cases (the sources with accretion disk winds i.e., PG 1211+143 and 3C 445 are not considered in the calculation). We notice that neither the ionizing luminosity (L_{ion}) nor the ionization parameter (ξ), the main factors involved in the estimate of $\dot{M}_{out}$, are correlated with rl. The significance of the correlation is 0.1 and 0.8 for

L_{ion} and ξ, respectively.

If confirmed by a larger set of data, two different scenarios could be invoked to explain these results:
(i) the gas distribution tends to preferentially clump together when the system is less perturbated by a strong radio source (jet ?). In this case, a mass outflow rate strongly dependent on the volume filling factor, could explain the correlation;
(ii) alternatively, if the geometry of the gas is similar in both RQ and RL objects, the $\dot{E}_{out}$ vs rl trend could imply that a larger amount of mass is dragged out from the nuclear region when the mechanism responsible for the radio emission is more efficient.

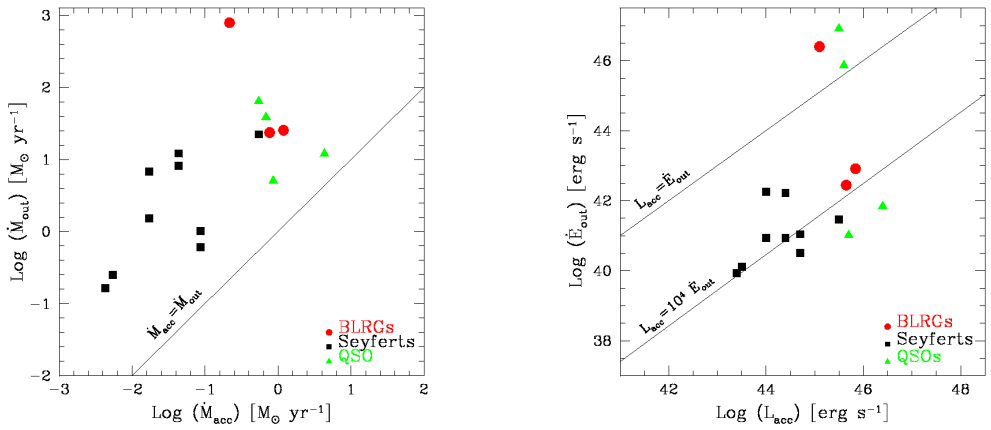

Figure 5.1 *Left panel*: mass outflow rate $\dot{M}_{out}$ plotted against the mass accretion rate $\dot{M}_{acc}$. *Right panel*: kinetic luminosity associated with the outflow ($\dot{E}_{out}$) plotted against the accretion luminosity (L_{acc}). The **red circles** are BLRGs; the **black squares** are Seyfert 1s and the **green triangles** are QSOs.

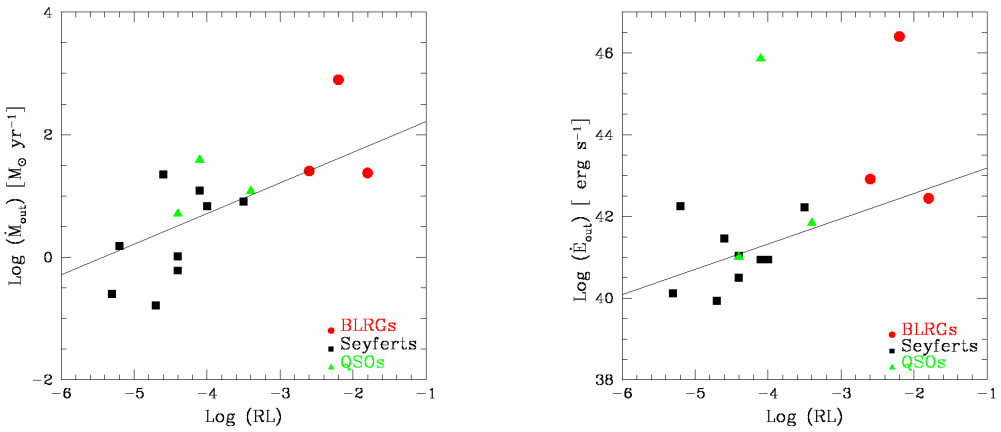

Figure 5.2 *Left panel*: mass outflow rate $\dot{M}_{out}$ plotted against the radio loudness (rl=$L_{1.4GHz}/L_{2-10keV}$). *Right panel*: kinetic luminosity associated with the outflow ($\dot{E}_{out}$) plotted against rl. The **red circles** are BLRGs; the **black squares** are Seyfert 1s and the **green triangles** are QSOs.

6

Discussion and Conclusions

One of the main debated astrophysical problem is the role of AGN feedback in the formation and evolution of galaxies. According to popular AGN/galaxy co–evolutionary scenarios, once central supermassive black holes reach masses $>10^7$–10^8 $M_\odot$, the AGN can heat the ISM inhibiting accretion and star formation. AGN/environment interaction can be split in two broad categories: the radiative mode, including ionization, heating, and radiation pressure (e.g. Ciotti &Ostriker 2007) and the mechanical mode via winds and jets (e.g. Ciotti, Ostriker, &Proga 2009; Shin, Ostriker, & Ciotti 2010).

This thesis presents a study of the circumnuclear environment of powerful radio galaxies (3C 33, 3C 382, 3C 390.3 and 3C 120), drawing some observational conclusions on the interplay among the nuclear engine and the surrounding medium. The investigation is based on high–resolution spectroscopy, a relatively new technique that offers the unique possibility to explore in detail the gaseous environment of AGNs. Unlike RQ AGNs, the application of this technique on RL sources has just started.

The detection of emission lines, very similar to those observed in Seyfert 2s, in the soft X–ray spectrum of the obscured BLRG 3C 445 (Grandi et al. 2007) opened a new window of investigation. The soft excess could be explained as emission from photoionized gas rather than jet radiation (as proposed by other authors), suggesting that in RL AGNs radiative mechanisms are at work also on kpc scales. This thesis provides further and new evidences of the presence of warm gas in RL AGNs, showing that slow outflowing gas can survive in environments where relativistic collimated plasma (jet) propagates.

In particular:

- The analysis of all the data of 3C 33, available in the *XMM–Newton* and *Chandra* archives, allowed the detection of soft emission lines, similar to those observed in Seyfert 2 galaxies (Guainazzi & Bianchi 2007). Moreover it was shown that this gas is positioned in the NLR, as attested by the perfect overlapping between the *Chandra* soft X–ray contours and the [OIII]λ5007 image (Fig.3.8).

- Unambiguously signatures of warm gas were observed, for the first time, in two BLRGs, namely 3C 382 and 3C 390.3. The *XMM-Newton*/RGS spectra revealed the presence of a gas (logξ=2.08–2.69), outflowing at velocities around 10^{2-3} km s^{-1}, probably located in the NLR (Chapter 4).

These results show that, like in Seyfert galaxies (Kinkhabwala et al. 2002), absorption and emission processes in RL AGNs can occur in the same plasma. Depending on the line–of–sight, different features can be revealed. Indeed the absorption lines due to photoionization and photoexcitation processes are preferentially observed in BLRGs, while the emission lines, produced by the inverse processes, are detected in sources with wide viewing angles (for example 3C 33). Interesting enough, no WA is detected in 3C 120, the BLRG with the smallest inclination angle (i<21°) and the only in the sample with a γ–ray counterpart recently discovered by *Fermi*.

In this thesis it is also shown that:

- The warm gas is probably clumped. Indeed, assuming a volume filling factor equal to 1, the mass outflow rates are implausible and much higher than the mass accretion rates. $\dot{M}_{out}$ and $\dot{M}_{acc}$ become comparable when C_v is as small as 0.01.

- The warm absorber detected in 3C 390.3 and 3C 382 is slow and probably related to the torus. Therefore, even considering upper limits on the mass outflow rate (if C_v=1), the kinetic luminosity related to the NLR outflow is always a negligible fraction (<1%) of both bolometric luminosity and jet kinetic power. It is however possible that the location of the ionized outflow is not unique. Recently it has been proposed that a very fast (v_{out}=10^4 km s^{-1}) winds, similar to those detected in the RQ PG 1211+143 and PG 0844+349, is also present in 3C 445. In these QSOs as well as in 3C 445 the winds have velocities of several thousands km s^{-1} and are probably directly connected

to the disk (Pounds et al. 2003a,b; Reeves et al. 2010). It should be noted that similar fast outflows would carry a huge amount of mass and energy. In particular in radio galaxies, $\dot{E}_{out}$ would compete with the jet in transferring momentum to the circumnuclear environment (unless very small covering factors and/or transient phenomena are invoked).

Aware of the limited number of BLRGs for which WA information is available, a first comparison between the RL and RQ properties is proposed in this thesis. The conclusions are:

- Unlike RL AGNs, Seyfert 1 warm absorbers are typically structured and outflowing at velocities ranging from a few to hundreds km s^{-1} (Blustin et al. 2005). The average number of modelled phases is two, but it seems that better quality data would require a larger number of phases. However as pointed out by Blustin et al. (2005), the number of phases itself is not a fundamental parameter to understand the ionization structure, but is more likely a function of the today's instrumentation and data quality.

- In both RQ and RL objects, the mass outflow rates exceed the mass accretion rate, as expected if the warm gas distribution is not uniform (i.e., a volume filling factor $\ll 1$).

- The kinetic luminosity related to the slow outflow is always negligible with respect to the accretion luminosity, independently on the radio power of the AGN.

- The mass outflow rate and kinetic luminosity seem to increase with the radio loudness (Fig. 5.2). Brighter radio sources have larger values of mass outflow rates. Two possible interpretations are suggested here:
  i) as the E_{out} is dependent on C_v, warm gas fills larger volumes in stronger radio sources, or ii) if the gas distribution is similar in both RL and RQ objects, the presence of intense radio emission (jets?) favors the escape of a larger amount of mass in the form of wind.

6.1 Future perspectives

The application of high–resolution spectroscopy on RL AGNs is just begun if compared with the amount of observations and results obtained for RQ AGNs so far.

Now we know that the circumnuclear environment of radio galaxies is similar to that of Seyferts, at least on kpc scales. However there are still many open questions:

- is there any link between accretion and ejection ?
- is there any link between winds and jets ?
- how do the outflows really influence the host galaxy?
- how long do they last? Are they short–living phenomena or not?
- are they really present only in a part of AGNs (50% in Seyfert 1s, 50% (?) in BLRGs), or could they be ubiquitous but not oriented along out line–of–sight (Elvis et al. 2000), or with a turbulent velocity or column density too low to be observed with today' s instrumentation (Blustin et al. 2005)

The next generation X–ray satellites (IXO and Astro–H) will answer these questions. As an example, we show the excellent quality spectra of 3C 33 and 3C 382 that will be obtained with IXO in very short (10 ksec) exposures (Fig. 6.1 and 6.2). This simple exercise shows the great potentiality of IXO. Its huge sensitivity will permit to exploit all the spectroscopical diagnostics (see Chapter 2), essentials to understand the physical, geometrical and kinematic properties of warm absorbers in local radio galaxies. More important, these measurements will be extended to a very large sample of radio–loud sources located at different redshifts, allowing to follow how feedback works in the galaxy evolution.

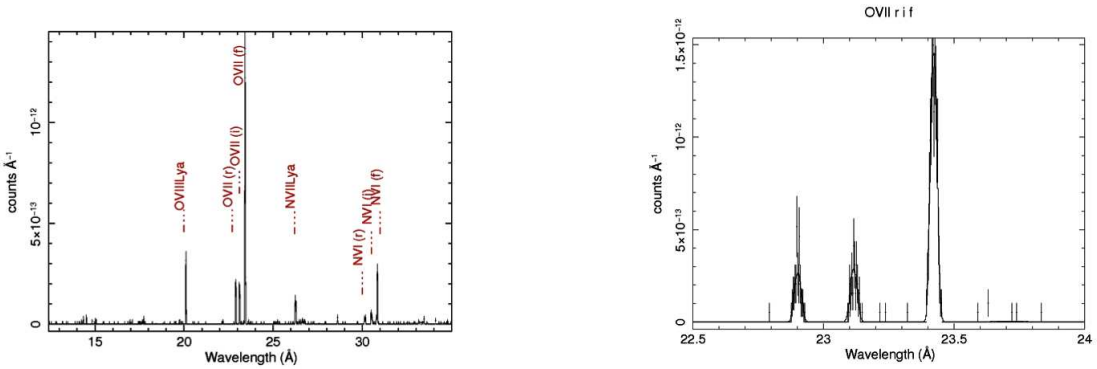

Figure 6.1 10 ks XGS simulation of 3C 33. *Left panel* shows the overall 0.3–2 keV band, the *right panel* is a zoom of the OVII He–like triplet. The simulation was performed using the core–glass response matrix available at `http://constellation-x.nasa.gov/science/responseMatrices.html#hxi`.

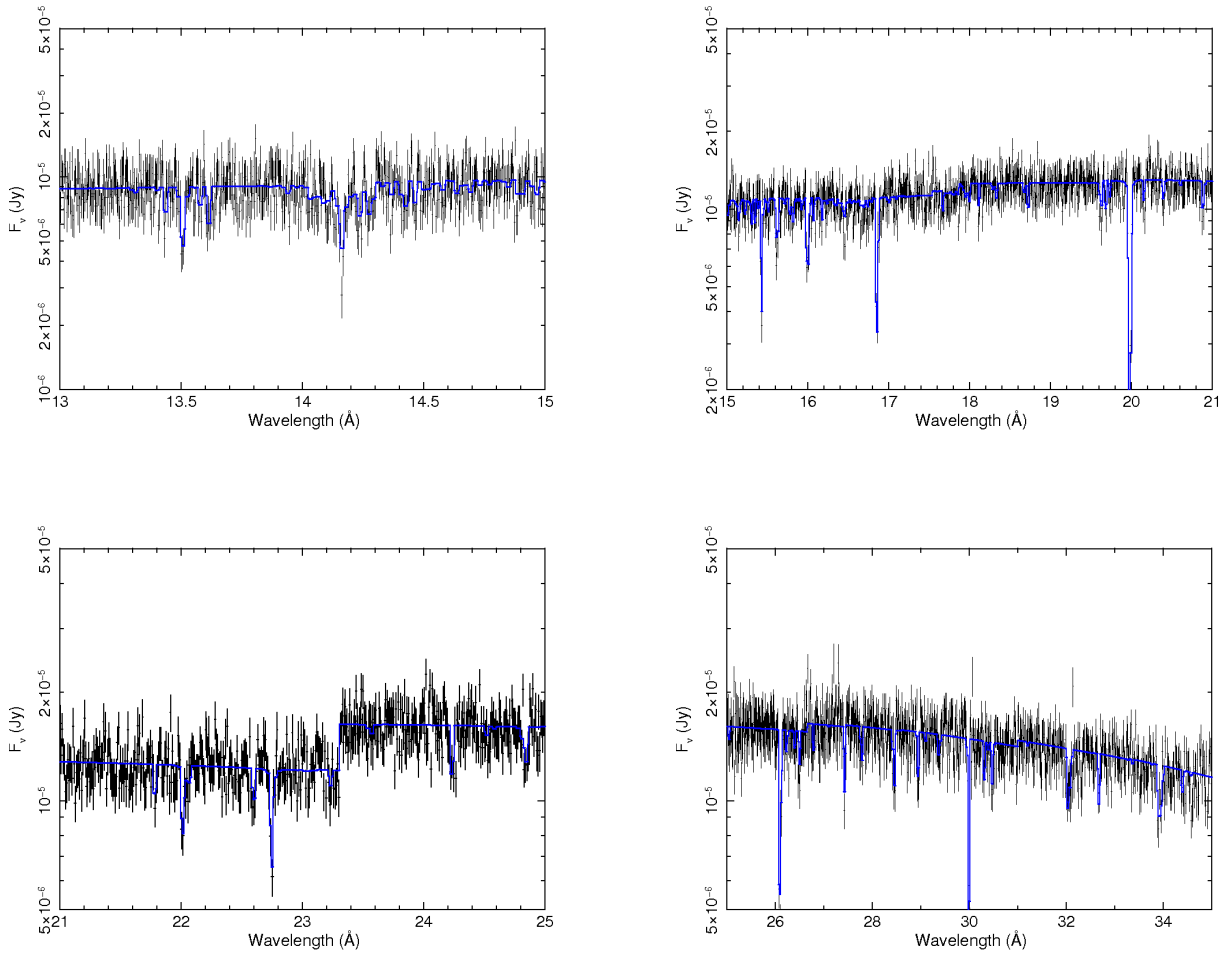

Figure 6.2 10 ks XGS simulation of the absorption features seen by *XMM–Newton* in 3C 382.

A

The XMM–Newton observatory

A.1 Basic characteristics

The *XMM–Newton* [1] (X–ray Multi Mirror) observatory (Jansen et al. 2001) was launched in December 1999 and it is dedicated to the exploration of the X–ray Universe in the 0.15–15 keV band. Its orbit is highly eccentric (Fig.A.1) between 7000 km (perigee) and 114000 km (apogee) and it has an inclination of about 40° with respect to the ecliptic. The orbital period is of about 48 hours, thus it is possible to perform uninterrupted observations as long as 150 ks (∼40 hours). Thanks to the six scientific instruments carried onboard, which work simultaneously, *XMM–Newton* allows to explore the X–ray and optical/UV bands at the same time. The scientific instruments are (Fig.A.2):

1. the **EPIC** (European Photon Imaging Cameras): three CCD cameras for X–ray imaging and moderate resolution (E/ΔE∼20–50) spectroscopy placed at the foci of the three X–ray telescopes: two MOS (Metal Oxyde Semiconductor) cameras (Turner et a. 2001), and one pn camera (Strüder et al. 2001).

2. the **RGS** (Reflection Grating Spectrometers) (den Herder et al. 2001): two identical spectrometers dedicated to high resolution X–ray spectroscopy, that are working in the 0.33–2.5 keV (5–38 $\AA$) energy band. The two instruments are made by dispersion gratings placed on the light path of the two MOS cameras.

[1] `http://xmm.esac.esa.int`

3. the **OM** (Optical Monitor) (Mason et al. 2001): optical/UV telescope with an aperture of ∼30 cm, for imaging and grism spectroscopy.

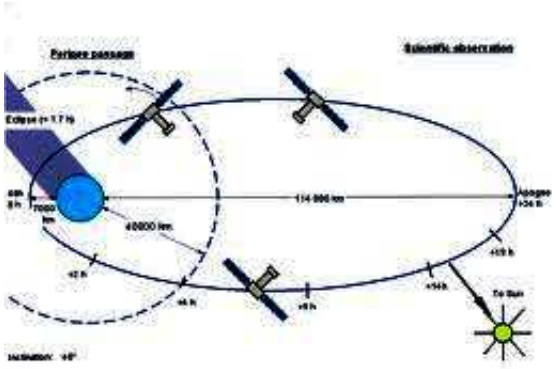

Figure A.1 Representation of the highly elliptical orbit of the *XMM–Newton* satellite.

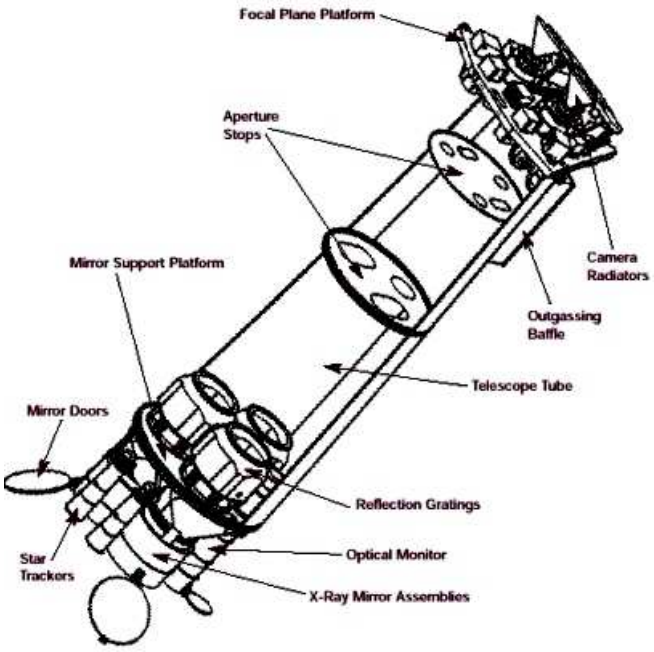

Figure A.2 Sketch of the *XMM–Newton* payload. At the bottom left there are the mirror modules, two of which are equipped with Reflection Grating Arrays. At the bottom right there are the focal X–ray instruments, the EPIC MOS and EPIC pn. Obscured by the lower mirror module is the OM.

Table A.1 summarizes the *XMM–Newton* general characteristics. The high sensitivity, medium (E/ΔE∼20–50) and high (E/ΔE∼200–800) energy resolution, good angular resolution, simultaneous and independent operation of all detectors, large uninterrupted observation windows for up 40 hours and the simultaneous observation in the X–ray and optical/UV band make *XMM–Newton* a very powerful instrument, as can be deduced from Table A.2, where its parameters are compared with the most important X–ray satellites.

Table A.1 *XMM–Newton* general characteristics.

Instrument	**EPIC pn**	**EPIC MOS**	**RGS**	**OM**
Bandpass	0.15–15 keV	0.15–12 keV	0.35–2.5 keV	180–600 nm
Sensitivity[a]	$\sim 10^{-14}$	$\sim 10^{-14}$	$\sim 8 \times 10^{-5}$	20.7 mag
Field of view(FOV)	$30'$	$30'$	$\sim 5'$	$17'$
PSF(FWHM/HEW)[b]	$6''/15''$	$5''/14''$	–	$1.4'' - 1.9''$
Pixel size	150 μm ($4.1''$)	40 μm ($1.1''$)	81 μm (9×10^{-3} Å)	$\sim 0.48''$
Timing resolution[c]	0.03 ms	1.5 ms	16 ms	0.5 s
Spectral resolution	$\sim$ 80 eV[d]	$\sim$ 70 eV[d]	0.04/0.025 $\AA$[e]	350[f]

(a) In the 0.15–15 keV energy band, in units of erg s^{-1} cm^{-2}.
(b) FWHM/HEW, where the half energy width (HEW) represents the integration radius at which corresponds an encircled energy of 50%.
(c) Refers to the fastest data acquisition mode of each instrument.
(d) At 1 keV; at the energy of 6.4 keV it is ≈150 eV for both EPIC cameras.
(e) At 1 keV it corresponds to a resolution of 3.2 eV.
(f) Resolving power in terms of $\lambda/\Delta\lambda$.

Table A.2 Comparison between *XMM–Newton* and other X–ray satellites.

Satellite	**Energy range [keV]**	**FOV [′]**	**FWHM [″]**	**A$_e$**[a] **[cm^2]**[a]	**Orbital period [hr]**
XMM–Newton	**0.15–15**	**30**	**6**	**4650**	**40**[b]
Chandra	0.1–10	30	0.2	800	50
ROSAT	0.1–2.4	38[c]	3.5	400	1.3[d]
ASCA	0.5–10	24	73	350	0.9[d]
RXTE	2–250	–	–	6500[e]	1.5
				800[f]	
BeppoSax	0.1–300	37[g]	9.7[h]	22[h]	1.6
		56[i]	75[l]	150[l]	
Integral	2–10000	16°[m]	2°	500	72
		9°[n]	12′	2600(CdTe)	
				3100(CsI)	
Swift (XRT)	0.2–10	23.6	5	135[a]	0.01–>24
Suzaku (XIS)	0.2–12	17	2’	340[a]	1.6

(a) @1.5 keV.
(b) Orbital visibility above 46,000 km.
(c) HRI.
(d) Low orbit with Earth occultation.
(e) PCA.
(f) HEXTE.
(g) LECS.
(h) @0.28 keV.
(i) MECS.
(l) @6 keV.
(m) SPI–Fully coded.
(n) IBIS–Fully coded.

A.2 The X–ray telescopes

XMM–Newton carries three grazing incidence Wolter type 1 X–ray telescopes (Fig.A.3), each with 58 concentric mirror shells. At the foci of the three telescopes there are the EPIC cameras and the RGS instruments (see Section A.4). Co–aligned with the X–ray telescopes is the OM.

This optical design provides to *XMM–Newton* the highest effective area of any X–ray mission so far, that is 4650 cm^2 at 1.5 keV and ∼3000 cm^2 at 6 keV (see Table A.2). Fig.A.4 shows the effective area of the individual X–ray instruments on *XMM–Newton*. As shown in Section A.3 the effective areas of the two MOS cameras are lower than that of the pn, because only part of the incoming radiation (∼44%) falls onto these detectors, while the other part falls onto the RGS as it is shown in Fig.A.5. An important critical parameter for a detector is its ability in focussing photons. This parameter is measured through the shape and dimension of the point spread function (PSF). The PSF describes how the light coming from a pointlike source is distributed on the detector. The PSF FWHM of the *XMM–Newton* telescopes is about 6". The PSF integrated in two dimensions as a function of the distance from the central peak, gives the fractional encircled energy, that is the amount of energy within a certain radius (see Fig.A.6, A.7).

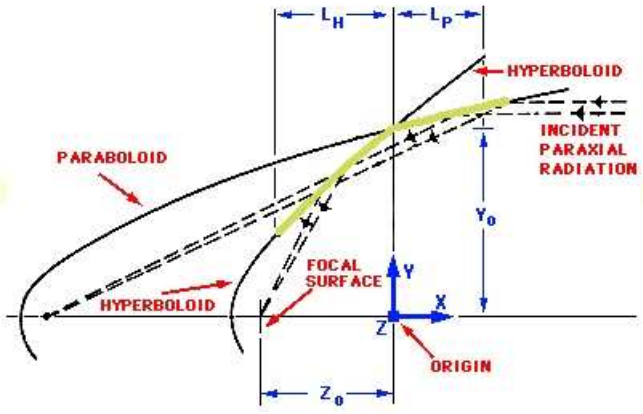

Figure A.3 Optical system of image reflection adopted for X–ray telescopes. The primary mirror is a paraboloid, while the secondary mirror is hyperboloid.

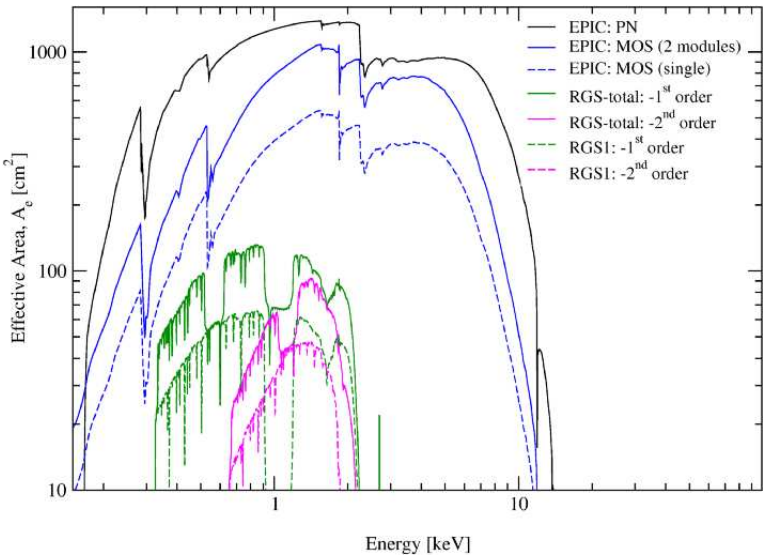

Figure A.4 Effective area of the different instruments onboard *XMM–Newton*: EPIC pn (*black*), EPIC MOS (*blue*) and RGS (*purple and green*).

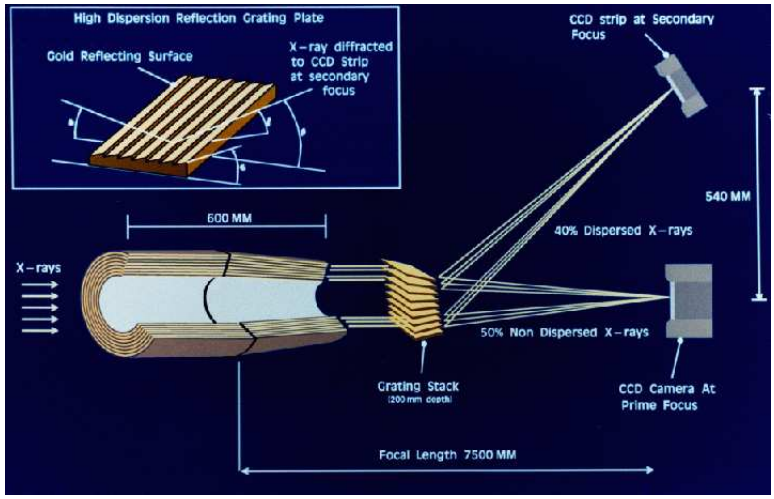

Figure A.5 Ray trace of *XMM–Newton* RGS and MOS (from `http://xmm.esac.esa.int`).

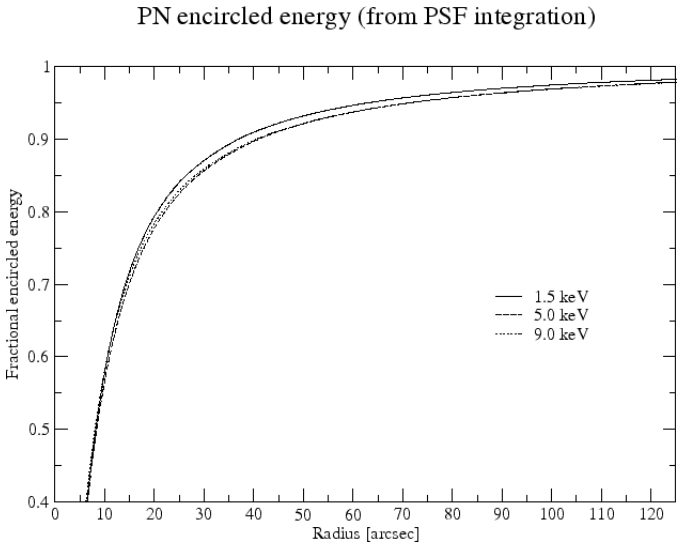

Figure A.6 Fraction encircled energy for the EPIC pn detector plotted as a function of the extraction radius (in arcsec). The curve is energy dependent, with a slight change going from 1.5 keV up to 5 keV and 9 keV.

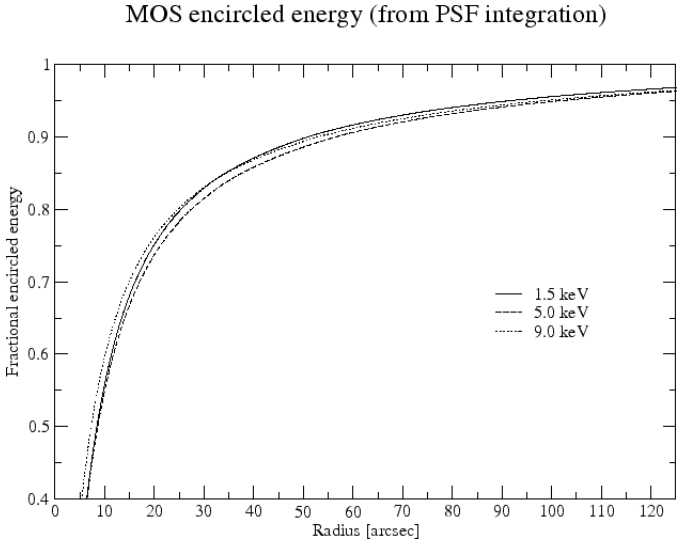

Figure A.7 Fraction encircled energy for the EPIC MOS cameras plotted as a function of the extraction radius (in arcsec).

A.3 The EPIC cameras

The three EPIC cameras offer the possibility to accumulate high statistics images and spectra. Their FOV is ∼30' and the angular resolution is around 6" FWHM (Fig.A.8). The two MOS are front–illuminated CCD cameras suited at the prime foci of two of the X–ray telescopes, while the pn is a back–illuminated CCD camera at the prime foci of the third mirror assembly.

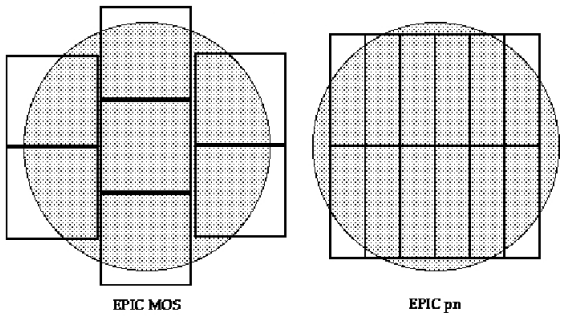

Figure A.8 Field of view (shaded circle) and arrangement of the CCDs on the focal plane of the two different EPIC cameras. *Left*: MOS and *right*: pn.

The EPIC cameras allow several modes of data acquisition (Table A.3). The main differences between the observing modes are due to the field of view and the readout time (e.g., the brightest sources generally require short readout time).

1. "full frame" and "extended full frame" mode (this is avalilable only for the pn): all the pixels of all the CCDs are read, meaning that the entire the field of view is observed;

2. "partial window": in "large window" mode (pn) only half of the FOV is read, while in "small window" mode only a piece of one CCD is used;

3. "timing": in this mode, imaging is made only in one dimension (x axis). Data are collapsed into a one–dimensional row to be read out at high speed.

Table A.3 Field of view and time resolution for different observing modes of the EPIC pn and EPIC MOS cameras.

EPIC pn (1 pixel=4.1″)	**FOV** (pixel)	**Temporal resolution** (ms)
Full frame	376×384	73.4
Extended full frame	376×384	200
Large window	198×384	48
Small window	63×64	6
Timing[a]	64×200	0.03
Burst[b]	64×20	0.007
EPIC MOS (1 pixel=1.1″)	**FOV** (pixel)	**Temporal resolution** (s)
Full frame	600×600	2.6
Large window	300×300	0.9
Small window	100×100	0.3
Timing[a]	100×600	1.5×10^{-3}

(a) In this mode the read–out cycle of the chips is reduced because the events detected on diffrent pixels are integrated along only one spatial coordinate.
(b) A special flavour of the timing mode of the EPIC pn camera which offers very high time resolution, but has a very low duty cycle of 3%.

A.4 The RGS

The RGS instruments provide the high–resolution spectroscopic capability of *XMM–Newton*, thanks to the energy resolution E/ΔE∼200–800. Reflection gratings obeys the following diffraction relation:

$$cos\beta = cos\alpha + \frac{m\lambda}{\delta} \tag{A.1}$$

where λ is the radiation wavelength, d is the distance of the gratings, and m is the spectral order.
The RGS is composed by two elements:

- the Reflection Grating Arrays (RGA): 182 identical diffraction gratings (Fig.A.9), with dimensions 10×20 cm each. The RGAs are positioned behind the two X–ray telescopes which focus onto the EPIC MOS cameras, and disperse about 40% of the incident X–rays from each telescope onto the RFC;
- the RGS Focal Camera (RFC): two CCD strips located at secondary foci (Fig. A.10).

The RGS works in the 5–38 $\mathring{A}$ (or 0.33–2.5 keV) waveband. The FWHM resolution in the first dispersion order is 0.06 $\mathring{A}$, and about half of this value in the second order. The systematic uncertainty in the wavelength scale is ±8m$\mathring{A}$. The effective areas of the two RGS instruments as a function of wavelength and energy, for both spectral orders, are plotted in Fig. A.11. The RGS1 CCD7 and the RGS2 CCD4 failed in the operation, thus the wavelength ranges 10.4–14.0 $\mathring{A}$ in RGS1 and 20.1–23.9 $\mathring{A}$ in the RGS2 are unavailable.

A.5 The OM

The OM is a 30 cm optical/UV telescope, sensitive over the range 180–600 nm, with ∼17' FOV. The OM has 7 optical and UV filters as well as an optical and a UV grism (Fig.A.12).

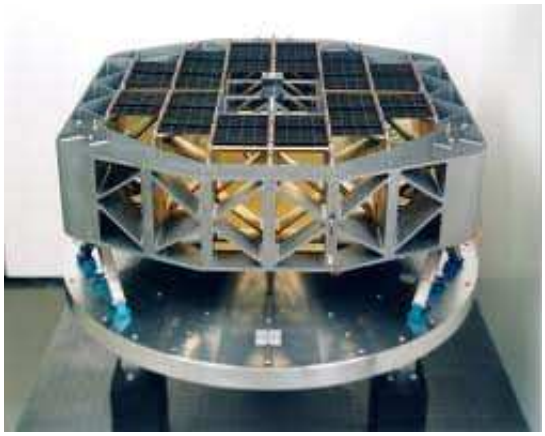

Figure A.9 The Reflection Grating Array (image from `http://xmm.esac.esa.int`)
.

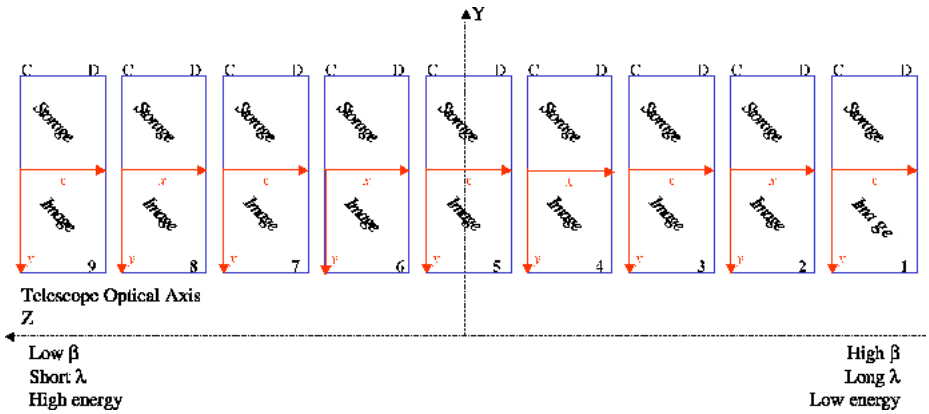

Figure A.10 Representation of the RGS Focal Camera. The RFC is composed by 9 CCDs. Half of each CCD is illuminated, the other half is left as storage area. The dispersion direction is along the Z axis.

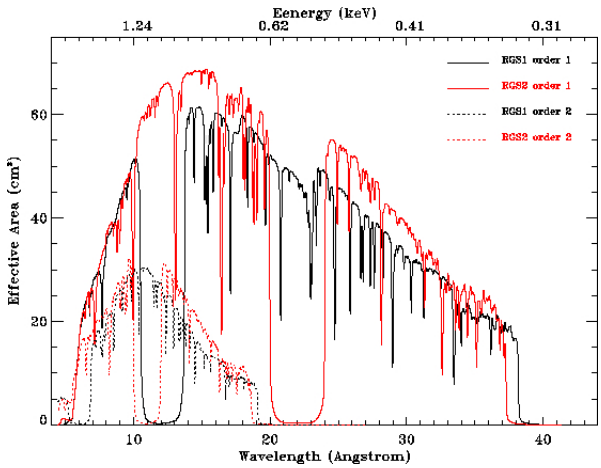

Figure A.11 RGS effective area for both first and second order, as a function of λ and energy.

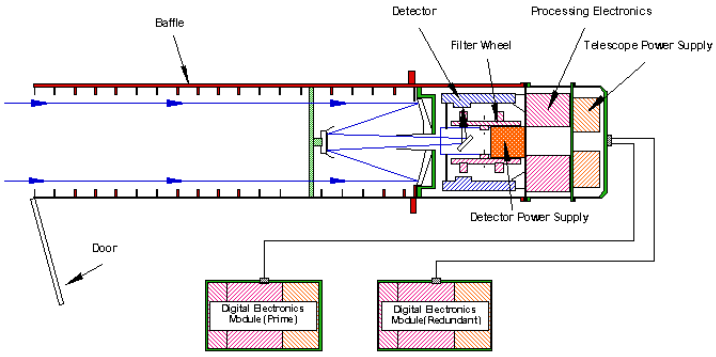

Figure A.12 Schematic representation of the OM telescope. Image from `www.esa.int`.

B

The Chandra X–ray observatory

The *Chandra* X–ray observatory [1] (Fig. B.1), the second satellite capable of high–resolution X–ray spectroscopy, was launched on July 1999.

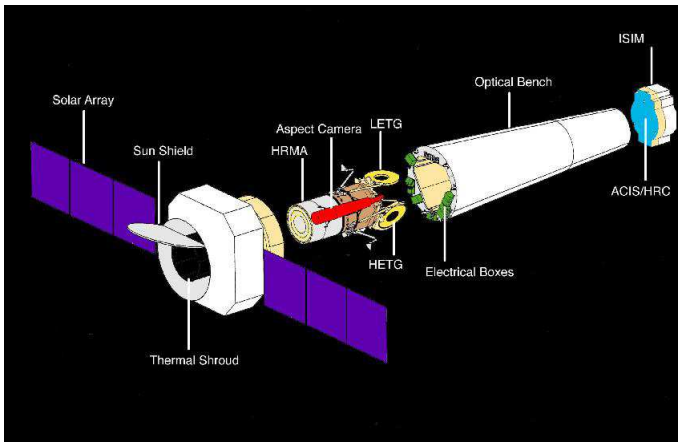

Figure B.1 Schematic representation and description of the *Chandra* satellite. Figure from `http://chandra.harvard.edu/resources/illustrations/`.

It has a single focusing telescope based on a Wolter type 1 grazing incidence X–ray mirrors pairs (the High Resolution Mirror Array or HRMA). The mirrors are combined with 4 science instruments: two focal plane instruments, ACIS and HRC, and two grating spectrometers, HETG and LETG [2]. Unlike *XMM–Newton* they do not work simultaneously.

[1] `http://cxc.harvard.edu`
[2] `http://chandra.harvard.edu/about/science_instruments.html`

1. The HRC (High Resolution Camera) is positioned at the end of the beam path and detects X–rays reflected from an assembly of 8 mirrors. The primary components of the HRC are two micro–channel plates (MCP; Fig. B.2). When combined with the *Chandra* mirrors the HRC can make images that reveal detail as small as one–half an arcsec.

2. The ACIS (Advanced CCD Imaging Spectrometer) is the other focal plane instrument. It is an array of CCD which makes X–ray images and at the same time measures the energy of each incoming X–ray. In this way ACIS allows the imaging of objects in the particular energy range in which a single element emits. As shown in Tab. A.2 the PSF FWHM of $0.2''$ makes *Chandra* an excellent satellite for spatially resolved studies.

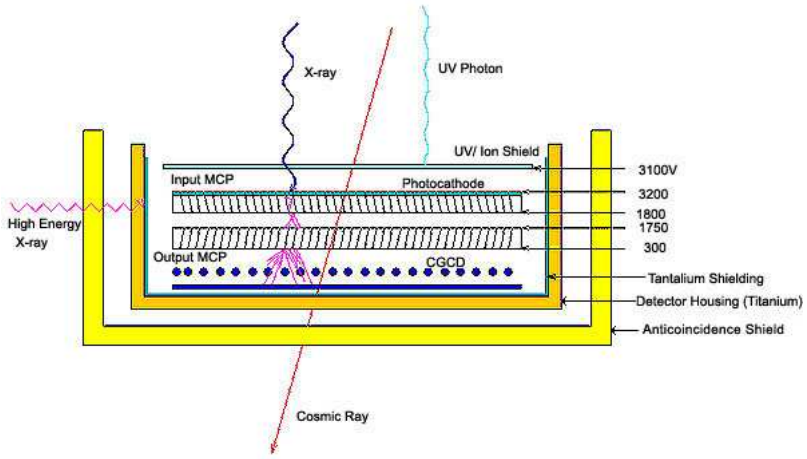

Figure B.2 Representation of the High Resolution Camera (HRC) onboard *Chandra*. From `http://chandra.harvard.edu/graphics/resources/illustrations/`.

3. The Low Energy Transimission Grating Spectrometer (LETG) array (Fig. B.4): is a single line grating that works in the 0.08–2keV energy band. It is composed by 540 individual grating elements mounted onto a toroidal ring structure with a diameter of 110 cm. It can reach a spectral resolving power of more than 1000. The LETGS consists of three elements: the HRMA of four nested paraboloid–hyperboloid grazing incidence mirror pairs, the LETG, and a dedicated position-sensitive detector in the focal plane.

4. The High Energy Transmission Gratings (HETG) (Canizares et al. 2005)

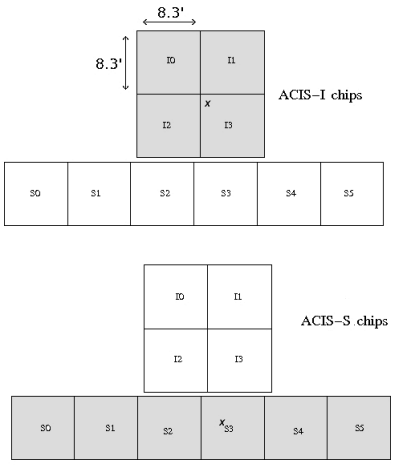

Figure B.3 ACIS instruments layout showing the imaging (ACIS–I) and spectroscopic (ACIS–S) array. Chips S1 and S3 are back–illuminated, while all the other chips are front–illuminated. From `http://cxc.harvard.edu/cal/Acis/`.

array (Fig.B.5): are designed to work in the 0.4–10 keV band. They consists of 336 gold gratings facets mounted on an assembly that can be swung into position behind the *Chandra* mirrors. The inner two rings are the high–energy grating, or HEG, while the outer two rings are the medium–energy grating, or MEG.

Both are transmission gratings etched in gold, and obey the relation:

$$\frac{m\lambda}{d} = sin\theta \tag{B.1}$$

The major differences between the grating spectrometers of *Chandra* and *XMM–Newton*, apart from being transmission gratings and reflection gratings, respectively, concerns the effective area and spectral resolution. As shown in Fig. B.6, which compares the gratings effective areas of both satellites, the RGS has a much higher effective area, but the spectral resolutions of the *Chandra* spectrometers are higher than the RGS (Fig. B.7), basically because the *Chandra* X–ray optics have a higher angular resolution (Paerels and Kahn, 2003).

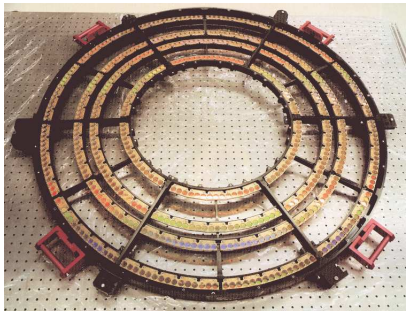

Figure B.4 The Low Energy Trasmission Grating (LETG) onboard *Chandra*. Figure from `http://www.mpe.mpg.de/xray/wave/rosat/gallery/calendar/1997/apr.php`.

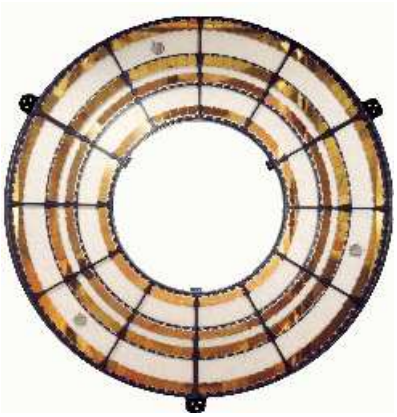

Figure B.5 The High Energy Transmission Gratings (HETGs) onboard *Chandra*. Figure from `http://space.mit.edu/HETG/hetg_info.html`.

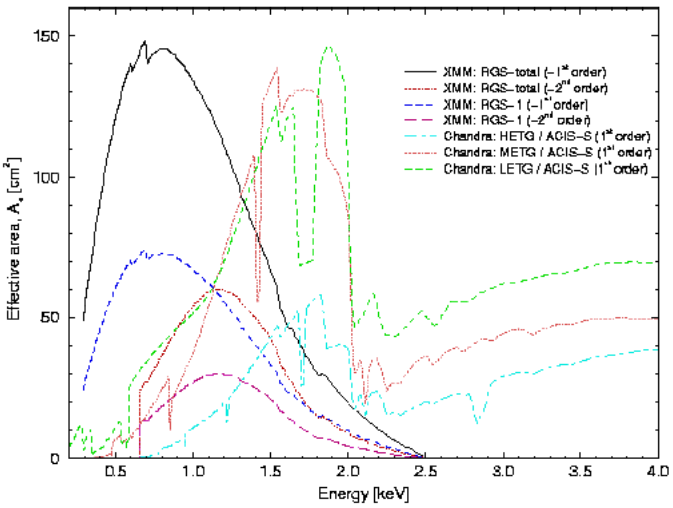

Figure B.6 Comparison of the effective areas of the grating spectrometers on *Chandra* and *XMM–Newton*. From Blustin 2004, Ph.D. Thesis.

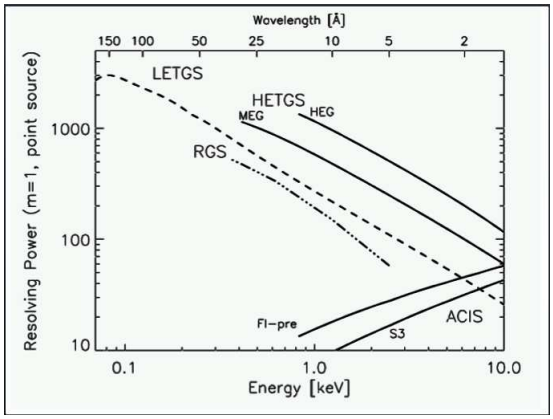

Figure B.7 Comparison of the resolving powers of the grating spectrometers on *Chandra* and *XMM–Newton*, in the first dispersion order (m=1). From Dewey 2001.

C

The IXO satellite

The *International X–ray Observatory*/IXO [1, 2] (Fig. C.1) is a joint effort of NASA, ESA and JAXA. Its launch is programmed for 2021.

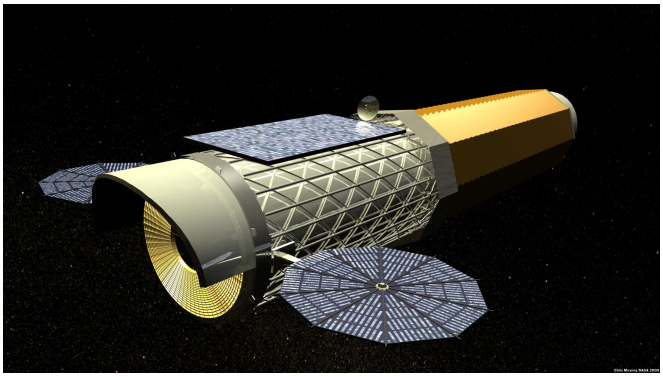

Figure C.1 The *IXO* satellite.

IXO will incorporate a single large X–ray mirror assembly (3 m^2 collecting area and 5″ angular resolution) and an extendible optical bench with a focal length of 20 m and a suite of focal plane instruments (Fig. C.2):

[1] http://sci.esa.int/science-e/www/object/index.cfm?fobjectid=42271
[2] http://ixo.gsfc.nasa.gov/

- the X–ray Microcalorimeter Spectrometer (XMS), provides high–spectral resolution, non–dispersive imaging spectroscopy over the energy range 0.3–7 keV;

- the Wield Field Imager (WFI), is an imaging X–ray spectrometer with a large FOV (18' × 18') and provides images and spectra in the 0.1–15 keV energy band. The Hard X–ray imager (HXI), mounted directly behind the WFI in the same instrument extends the energy coverage to 40 keV, working simultaneously with the WFI;

- the X–ray grating spectrometer (XGS) is a wavelength–dispersive spectrometer that will provide high spectral resolution in the 0.3–1 keV band. The XGS will have a spectral resolving power of $\lambda/\Delta\lambda$=3000 and effective area larger than 1000 cm^2 across its operating band (Fig. C.3). The high–resolution spectrosocpy is achieved through an array of wavelength–dispersive diffraction gratings with a fine pitch of 5000 lines/mm or more.

- the High Timing Resolution Spectrometer (HTRS) will perform high precision timing measurements of brigth X–ray sources. It can observe sources with fluxes 10^6 cts/s in the 0.3–10 keV energy band without performance degradation, and provides moderate spectral resolution of 150 eV FWHM at 6 keV.

- the X–ray Polarimeter (XPOL) is an imaging polarimeter with polarization sensitivity of 1% for a source with $F_{2-10keV}$= 1 mCrab in 10^5 sec of exposure.

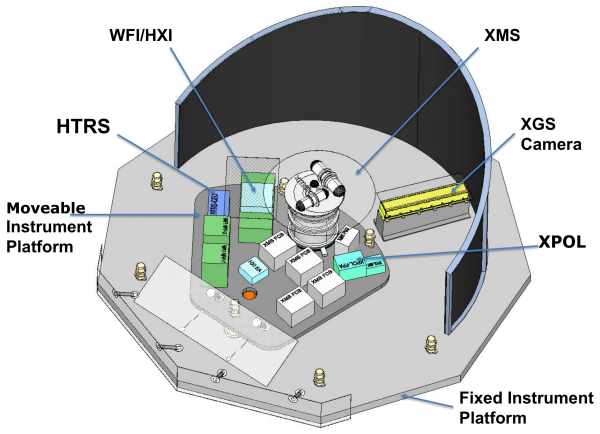

Figure C.2 *IXO* instrument module. Credit: NASA.

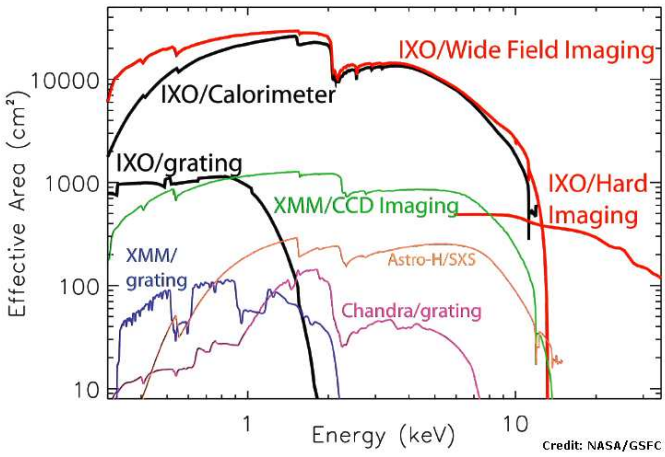

Figure C.3 Effective area of *IXO* mirror and instruments.

Acknowledgements

I am sincerely grateful to my supervisor Paola Grandi for the continuous support, enthusiasm, brilliant and insightful suggestions, and for the significant effort she has put in this project. I am also indebted to her for always encouraging me to do my best.

I would like to thank Prof. Giorgio Palumbo for his enthusiastic guidance, he is a reference of scientific passion and professionality.

A special thank to Matteo Guainazzi for giving me the opportunity to work a few months at ESAC (among many difficulties!). It was really a pleasure to collaborate with him.

I am grateful to all the collaborators I have worked with during these three years, I have learned a lot from fruitful interactions with them.

A big thank goes to my office–mates Valentina for being above all a good friend, and Barbara for keeping the atmosphere light and providing me lots of chocolate bars during the writing up of my thesis.

Thanks to all the people working at the IASF institute in Bologna, past and present, for providing a very friendly and enjoyable atmosphere. In particular thanks to Adriano, Matteo and Enrico for technical assistance whenever my computer crashed, and to Elisabetta, Pietro, Lorenzo and Giulia. Thanks to my "Spanish" friend Enrica for the wonderful time spent in Madrid, and to Cristina for being the perfect flatmate.

Thanks to Filippo for the many entertaining discussions drinking a glass of good wine.

Special big big thanks to Chiara, Monica, Lucia, Michela, Francesca, Letizia, Sara, Maura, Antonella, Marta for being the best friends one could ever have.

Thanks from the deepest of my heart to my parents Sergio and Lorella, my sister Veronica and the other half of my sky Vito for their love and regardless support.

Part I

Bibliography

Abdo, A.A., et al. 2010a, ApJS, 188, 405
Abdo, A.A., et al. 2010b, ApJ, 715, 429
Abdo, A.A., et al. 2010c, ApJ, 720, 912
Abdo, A.A., et al. 2010d, Science, 328, 725
Abramowicz, M.A., Chen, X., Kato, S., Lasota, J.-P., Regev, O. 1995, ApJ, 438, 37
Aharonian, F. et al. 2003, A&A, 403, L1
Aharonian, F. et al. 2009, ApJ, 695, L40
Alef, W., Wu, S. Y., Preuss, E., Kellermann, K. I., Qiu, Y. H. 1996, A&A, 308, 376
Anders, E., Grevesse, N. 1989, GeCoA, 53, 197
Antonucci, R.R.J., Miller J.S., 1985, ApJ, 297, 621
Antonucci, R.R.J., 1993, ARA&A, 31, 473
Antonucci, R.R.J., Hurt T., Kinney A., 1994, Nature, 371, 313
Antonucci, R.R.J. 2011, arXiv:1101.0837v1
Arnaud, K. A. 1996, XSPEC: the first ten years, in Astronomical Data Analysis Software and Systems V, ed. G. H. Jacoby, & J. Barnes, ASP Conf. Ser., 101, 17
Atwood, W. B., et al. 2009, ApJ, 697, 1071
Ballantyne, D.R., Fabian, A.C., Iwasawa, K. 2004, MNRAS, 354, 839
Ballantyne, D.R. 2005, MNRAS, 362, 1183 Balmaverde, B., Capetti, A., Grandi, P. 2006, A&A, 451, 35
Baum, S.A., Heckman, T. 1989, ApJ, 336, 680
Baum, S.A. 1992, *Clusters and Superclusters of Galaxies*, ed. A.C. Fabian (Cambridge:CUP), p.171
Baum, S.A., Heckman, T.M., Van Breugel, W. 1992, ApJ, 389, 208
Bautista, M.A., & Kallman, T.R. 2001, ApJS, 134, 139
Behar, E., Sako, M., Kahn, S.M. 2001, ApJ, 563, 497
Belsole, E., Worrall, D.M., Hardcastle, M.J. 2006, MNRAS, 366, 339
Bennett, A.S. 1962, MNRAS, 125, 75
Bianchi, S., Miniutti, G., Fabian, A.C., et al. 2005, MNRAS, 360, 380
Bianchi, S., Guainazzi, M., & Chiaberge, M. 2006, A&A, 448, 499
Black, A.R.S., Baum, S.A., Leahy, J.P., Perley, R.A., Riley, J.M., Scheuer, P.A.G. 1992, MNRAS, 256, 186
Blandford, R.D., & Begelman, M. 1999, MNRAS, 303, L1
Blustin, A. J., Branduardi-Raymont, G., Behar, E., et al., 2002, A&A, 392, 453
Blustin, A.J. 2004, Ph.D. Thesis, AA (MSSL–UCL)
Blustin A. J., Page M. J., Fuerst S. V., Branduardi-Raymont G., Ashton C. E., 2005, A&A, 431, 111

Blustin, A.J., Fabian, A.C. 2009, MNRAS, 396, 1732
Bohlin, R.C., Savage, B.D., & Drake, J.F. 1978, ApJ, 224, 132
Braito, V., Reeves, J.N., Sambruna, R.M., Gofford, J. 2011, MNRAS, arXiv1102.5234
Brinkman, A.C., Kaastra, J.S., van der Meer, R.L.J., Kinkhabwala, A., Behar, E., Kahn, S.M., Paerels, F.B.S., Sako, M. 2002, A&A, 396, 761
Burbidge, E.M., 1967, ApJ, 149, L51
Burgess, A.M., Hunstead, R. W. 2006a, AJ, 131, 100
Burgess, A.M., Hunstead, R. W. 2006b, AJ, 131, 114
Buttiglione, S., Capetti, A., Celotti, A., Axon, D.J., Chiaberge, M., et al. 2009, A&A, 495, 1033
Canizares et al. 2005, PASP, 117, 1144
Cardelli, J.A., Klayton, G.C., Mathis, J.S., 1989, ApJ, 345, 254
Cash W., 1979, ApJ, 228, 939
Chiaberge, M., Capetti, A. & Celotti, A. 2000, A&A 355, 873
Chiaberge, M., Macchetto, F.D., Sparks, W.B. et al. 2002, ApJ, 571, 247
Ciotti, L., Ostriker, J.P. 2007, ApJ, 665, 1038
Ciotti, L., Ostriker, J.P., Proga, D. 2009, ApJ, 699, 89
Cleary, K., Lawrence, C.R., Marshall, J.A., Hao, L., Meier, D. 2007, ApJ, 660, 117
Costantini, E., Kaastra, J.S., Arav, N., Kriss, G.A., Steenbrugge, K.C., et al. 2007, A&A, 461, 121
Crenshaw, D.M., Kraemer, S.B., George, I.M. 2003, ARA&A, 41, 117
den Herder J.W., Brinkmann A.C., Kahn S.M., Branduardi–Raymont G., et al., 2001, A&A, 365, 7
Dere, et al. 1997, AASS, 125, 149
Donato, D., Sambruna, R.M., & Gliozzi, M. 2004, ApJ, 617, 915
Eracleous, M., & Halpern, J. P. 1998, ApJ, 505, 577
Eracleous, M., Sambruna, R.M., Mushotzky, R.F. 2000, ApJ, 537, 654
Evans, D.A., Hardcastle, M.J., Croston, J.H., Worrall, D.M., Birkinshaw, M. 2005, MNRAS, 359, 363
Evans, D.A., Worrall, D.M., Hardcastle, M.J., Kraft, R.P., Birkinshaw, M. 2006, ApJ, 642, 96
Evans, D. A., Reeves, J. N., Hardcastle, M. J., Kraft, R. P., Lee, J. C., Virani, S. N. 2010, ApJ, 710, 859
Fabbiano, G., Miller, L., Trinchieri, G., Longair, M., Elvis, M. 1984, ApJ, 277, 115
Fanaroff, B. L., Riley, J. M. 1974, MNRAS, 167, 31

Ferland, G.J., Korista, K.T., Verner, D.A., Ferguson, J.W., Kingdon, J.B., & Verner, E.M. 1998, PASP, 110, 761
Ferrarese, L., Merritt, D. 2000, ApJ, 539, L9
Floyd, D.J.E., Kukula, M.J., Dunlop, J.S., McLure, R.J., Miller, L., Percival, W.J., Baum, S.A., O'Dea, C.P. 2004, MNRAS, 355, 196
Friedman, H., Lichtman, S.W., Byram, E.T. 1951, Phys. Rev., 83, 1025
Gabriel A.H., Jordan C., 1969, MNRAS, 145, 241
Gallimore, J.F., Baum, S.A., O'Dea, C.P. 1997, Nature, 388, 852
Gebhardt, K., et al. 2000, ApJ, 539, L13
Ghisellini, G., Haardt, F., & Matt, G. 1994, MNRAS, 267, 743
Ghisellini, G., Celotti, A. 2001, MNRAS, 327, 739
Ghisellini, G., Tavecchio, F., Chiaberge, M. 2005, A&A, 432, 401
Ghisellini, G. & Tavecchio, F. 2008, MNRAS, 387, 1669
Ghosh, K. K., Sondararajaperumal, S. 1991, AJ, 102, 1298
Giacconi, R., Gursky, H., Paolini, F., & Rossi, B.B. 1962, PRL, 9, 439
Gierliński, M., & Done, C., 2004, MNRAS, 349, 7
Giovannini, G., Feretti, L., Gregorini, L., Parma, P. 1988, A&A, 199, 73
Giovannini, G., Cotton, W. D., Feretti, L., Lara, L., Venturi, T. 2001, ApJ, 552, 508
Giovannini, G., Taylor, G.B., Feretti, L., Cooton, W.D., Lara, L., Venturi, T. 2005, ApJ, 618, 635
Giroletti, M. 2008, ASPC, 386, 176
Gliozzi, M., Sambruna, R.M., Eracleous, M. 2003, ApJ, 584, 176
Gliozzi, M., Sambruna, R. M., Eracleous, M., & Yaqoob, T. 2007, ApJ, 664, 88
Gofford, J., Reeves, J.N., Turner, T.J., Tombesi, F., Braito V., et al. 2011, MNRAS, arXiv1103.0661
Gomez, J., Marscher, A.P., Alberdi, A., et al. 2001, ApJ, 561, L161
Grandi, P., Guainazzi, M., Haardt, F., Maraschi, L., Massaro, E., Matt, G., Piro, L., Urry, C. M. 1999, A&A, 343, 33
Grandi, P., Maraschi, L., Urry, C.M., & Matt, G. 2001, ApJ, 556, 35
Grandi, P., Malaguti, G., & Fiocchi, M. 2006, ApJ, 642, 113
Grandi, P., Guainazzi, M., Cappi, M., Ponti, G., 2007, MNRAS, L85
Grevesse, N., & Sauval, A. J. 1998, Space Sci. Rev., 85, 161
Guainazzi M., Bianchi S., 2007, MNRAS, 374, 1290
Haardt, F., Maraschi, L., 1991, ApJ, 380, 51
Haardt, F., Maraschi, L., 1993, ApJ, 413, 507

Haardt, F., Maraschi, L., Ghisellini, G., 1994, ApJ, 432, 95
Halpern, J.P. 1984, ApJ, 281, 90
Hardcastle, M.J., Birkinshaw, M., & Worrall, D.M. 1998, MNRAS, 294, 615
Hardcastle M.J., Worrall D.M., 1999, MNRAS, 309, 969H
Hardcastle, M.J., Evans, D.A., Croston, J.H. 2006, MNRAS, 370, 1893
Hardcastle, M.J., Evans, D.A., Croston, J.H., 2007, MNRAS, 376, 1849
Harris, D.E., Mossman, A.E., Walker, R.C. 2004, ApJ, 615, 161
Harris, D.E., & Krawczynski, H. 2006, ARAA, 44, 463
Hartman, R.C., et al. 1999, ApJS, 123, 79
Heckman, T.M. 1980, A&A, 87, 152
Heckman, T.M., Carty, T.J., Bothun, G.D. 1985, ApJ, 288, 122H
Heckman, T.M., Smith E.P., Baum S.A., et al., 1986, ApJ, 311, 526
Hewitt, A., Burbidge, G. 1991, ApJS, 75, 297
Ho, L.C. 2008, ARA&A, 46, 475
Ichimaru, S. 1977, ApJ, 214, 840
Jackson, N., Rawlings, S. 1997, MNRAS, 286, 241
Jaffe, W., Ford, H.C., Ferrarese, L., van den Bosch, F., O'Connell, R.W. 1993, Nature, 364, 213
Jansen, F., Lumb, D., Altieri, B., Clavel, J., Ehle, M., Erd, C., Gabriel, C., Guainazzi, M., et al. 2001, A&A, 365, 1
Kaastra, J.S. 1992, An X–Ray Spectral Code for Optically Thin Plasmas, Internal SRON–Leiden Report, updated version 2.0
Kaastra, J. S., Mewe, R., Nieuwenhuijzen, H., 1996, in Yamashita, K.,Watanabe, T., eds, UV and X–Ray Spectroscopy of Astrophysical and Laboratory Plasmas. Universal Academy Press, Tokyo, p. 411
Kaastra, J.S., Paerels, F.B.S., Durret, F., Schindler, S., Richter, P. 2008, Space Science Reviews, Volume 134, Issue 1-4, pp. 155-190
Kahn, S.M. 2002, "Soft X–Ray Spectroscopy of Astrophysical Plasmas", Columbia University
Kahn, S.M., Behar, E., Kinkhabwala, A., & Savin, D.W. 2002, Royal Society of London Philosophical Transactions Series A, 360, 1923
Kalberla, P.M.W., Burton, W.B., Hartmann, D., Arnal, E.M., Bajaja, E., Morras, R., & Pöppel, W.G.L. 2005, A&A, 440, 775
Kataoka, J., Stawarz, L. 2005, ApJ, 2005, 622, 797
Kataoka, J., Reeves, J.N., Iwasawa, K., et al. 2007, PASJ, 59, 279
Kellermann, K.I., Sramek, R., Schmidt, M., Shaffer, D.B., Green, R. 1989, AJ, 98,

1195
Kewley, L.J., Dopita, M.A., Sutherland, R.S., Heisler, C.A., Trevena, J. 2001, ApJ, 556, 121
Kinkhabwala, A., Sako, M., Behar, E., Kahn, S.M., Paerels, F., Brinkman, A.C., Kaastra, J.S., Gu, M.F., Liedhal, D.A. 2002, ApJ, 575, 732
Kinkhabwala, A., 2003, Ph.D. Thesis, AA (Columbia University)
Kirsch, M. 2006, "EPIC status calibration and data analysis", XMM-SOC-CAL-TN-0018, Issue 2.5
Klavel, J., Schulz, B., Altieri, B., Barr, P., et al. 2000, A&A, 357, 839
Klöckner, H.-R., Baan, W.A., Garrett, M.A. 2003, Nature, 421, 821
Knapp, G.R., Bies, W.E., Van Gorkom, J.H. 1990, AJ, 99, 476
Komatsu, E., et al. 2009, ApJS, 180, 330
Koski, A.T. 1978, ApJ, 223, 56
Kraft, R.P., Birkinshaw, M., Hardcastle, M.J., Evans, D.A., Croston, J.H., Worrall, D.M., Murray, S.S. 2007, ApJ, 659, 1008
Krolik, J.H., & Kriss, G.A. 2001, ApJ, 561, 684
Krongold, Y., Nicastro, F., Elvis, M., et al. 2007, ApJ, 659, 1022
Kruper, J. S., Canizares, C. R., Urry, C. M. 1990, ApJS, 74, 347
Laing, R.A., Riley, J.M., Longair, M.S. 1983, MNRAS, 204, 151
Landi et al. 2006, ApJSS, 162, 261
Leahy, J.P., Perley, R.A. 1991, ApJ, 102, 2
Leighly, K. M., O'Brien, P. T. 1997, ApJ, 481, 15
Liedahl, D.A., Osterehled, A.L., Goldstein, W.H. 1995, ApJL, 438, 115
Liedahl, D.A., & Paerels, F. 1996, ApJL, 468, L33
Lightman A.P., White T.R., 1988, ApJ, 335, 57
Lilly, S.J., Longair, M.S. 1982, MNRAS, 199, 1053
Lister, M. L., Cohen, M. H., Homan, D. C., Kadler, M., Kellermann, K. I., Kovalev, Y. Y., Ros, E., Savolainen, T., Zensus, J. A. 2009, AJ, 138, 1874
Magdziarz, P., Zdziarski, A.A. 1995, MNRAS, 273, 837
Magorrian, J., Tremaine, S., Richstone, D., Bender, R., et al. 1998, AJ, 115, 2285
Mahadevan, R., Narayan, R., Krolik, J. 1997, ApJ, 486, 268
Maraschi, L., Chiappetti, L., Falomo, R., et al. 1991, ApJ, 368, 138
Marchesini, D., Celotti, A., Ferrarese, L. 2004, MNRAS, 351, 733
Mariotti, M., et al. 2010, ATel#2916
Martel, A. R., et al. 1999, ApJS, 122, 81
Mason, K.O., Breevedl, A., Much, R. 2001, A&A, 365, L36

Mathews, W.G., & Ferland, G.J. 1987, ApJ, 323, 456
McKernan, B., Yaqoob, T., Mushotzki, R.F., Ian, M.G., Turner, T.J. 2003, ApJ, 598, L83
McKernan, B., Yaqoob, T., Reynolds, C.S. 2007, MNRAS, 379, 1359
Mewe, R., Gronenschild, E.H.B.M., van den Oord, G.H.J.1985, A&AS, 62, 157
Mewe, R., Lemen, J.R., van den Oord, G.H.J. 1986, A&AS, 65, 511
Migliori, G., Grandi, P., Palumbo, G.G.C., Brunetti, G., Stanghellini, C. 2007, ApJ, 668, 203
Migliori, G., Grandi, P., Torresi, E., Dermer, C., Finke, J., Celotti, A., Mukherjee, R., Errando, M., Gargano, F., Giordano, F., Giroletti, M. 2011, submitted to A&A
Miller, C.J., Robert, C.N., Gómez, P.L., Hopkins, A.M., Bernardi, M. 2003, ApJ, 597, 142
Mukherjee, R., Halpern, J., Mirabal, N., Gotthelf, E. V. 2002, ApJ, 574, 693
Muxlow, T.W.B., Garrington, S.T. 1991, "Beams and Jets in Astrophysics" , edited by P.H. Hughes, Cambridge Astrophysics Series, p55
Narayan, R., Yi, I. 1994, ApJ, 428, 13
Narayan, R., Yi, I. 1995, ApJ, 452, 710
Netzer, H. 1996, ApJ, 473, 781
Netzer, H. 2004, ApJ, 604, 551
Nicastro, F., Fiore, F., Perola, G. C., Elvis, M., O'Dea, C.P. 1998, PASP, 110, 493
OÒea, C.P. 1998, PASP, 110, 493
Ogle, P.M., Brookings, T., Canizares, C.R., Lee, J.C., Marshall, H.L. 2003, A&A, 402, 849
Ogle, P.M., Davis, S.W., Antonucci, R.R.J., et al. 2005, ApJ, 618, 139
Paerels, F.B.S., & Kahn, S.M. 2003, ARA&A, 41, 291
Pearson, T. J., Readhead, A. C. S. 1988, ApJ, 328, 114
Perley, R. A., Dreher, J. W., Cowan, J. J. 1984, ApJ, 285, 35
Peterson, B. M., 1997, "An Introduction to Active Galactic Nuclei", Cambridge, UK: Cambridge Univ. Press
Peterson, B. M., Ferrarese, L., Gilbert, K. M., et al., 2004, ApJ, 613, 682
Popescu, C.C., Hopp, U., Hagen, H.J., Elsaesser, H. 1996, A&AS, 116, 43
Porquet, D., Dubau, J. 2000, A&AS, 143, 495
Porquet D., Mewe, R., Dubau, J., Raassen, A.J.J., Kaastra, J.S. 2001, A&A, 376, 1113
Porquet, D., Dubau, J., Grosso, N. 2010, Space Science Reviews
Pounds, K.A., King, A.R., Page, K.L., O'Brien, P.T. 2003a, MNRAS, 346, 1025

Pounds, K.A., Reeves, J.N., King, A.R. 2003b, MNRAS, 345, 705
Pounds, K.A., & Page, K.L. 2005, MNRAS, 360, 1123
Pounds, K.A., & Vaughan, S. 2006, MNRAS, 368, 707
Prestage, R.M., Peacock, J.A. 1988, MNRAS, 230, 131
Prieto, M.A. 2000, MNRAS, 316, 442
Proga, D., & Kallman, T.R. 2004, ApJ, 616, 688
Quillen, A.C., Almog, Jessica, Ukita, Mihoko 2003, AJ, 126, 2677
Ramos Almeida, C., Perez Garcia, A.M., Acosta-Pulido, J.A. and Rodriguez Espinosa, J.M. 2007, AJ, 134, 2006
Raymond, J.C., Smith, B.W. 1977, ApJS, 35, 419
Rees, M.J . 1984, ARA&A, 22, 471
Reeves, J. N., Sambruna, R.M., Braito, V., Eracleous, M. 2009, ApJ, 702, 187
Reeves, J. N., Gofford, J., Braito, V., Sambruna, R. 2010, ApJ, 725, 803
Reynolds C. S., 1997, MNRAS, 286, 513
Risaliti, G. 2002, A&A, 386, 679
Rybicki, G., Lightman, A.P. 1979, Radiative Processes in Astrophysics, New York, Wiley–Interscience, 393 pp.
Rudnick, L., Jones, T.W., Fiedler, R. 1986, AJ, 91, 1111
Sako, M., Kahn, S.M., Paerels, F., et al. 2000a, ApJ, 543, L115
Sako, M., Kahn, S.M., Paerels, F., Liedahl, D.A. 2000b, ApJ, 542, 648 Sako, M., Kahn, S.M., Behar, E., Kaastra, J.S., Brinkman, A.C., Boller, T., et al. 2001, A&A, 365, L168
Salpeter, E.E., 1964, ApJ, 140, 796
Sambruna R.M., Eracleous M., Mushotzky R.F. 1999, ApJ, 526, 60
Sambruna, R.M., Netzer, H., Kaspi, S., et al. 2001, ApJ, 546L, 13S
Sambruna R.M., Reeves J.N., Braito V., 2007, ApJ, 665, 1030
Sambruna, R. M., Reeves, J. N., Braito, V., Lewis, K. T., Eracleous, M., et al. 2009, ApJ, 700, 1473
Sanders, D. B., Phinney, E. S., Neugebauer, G., Soifer, B. T., Matthews, K. 1989, ApJ, 347, 29
Santos–Lleo, M., Schartel, N., Tananbaum, H., Tucker, W., Weisskopf, M.C. 2010, arXiv1003.1961
Scheuer, P.A.G., Readhead, A.C.S. 1979, Nature, 277, 182
Seielstad, G.A., Cohen, M.H., Linfield, R.P., et al. 1979, ApJ, 229, 53
Shakura N. I., Sunyaev R., 1973, A&A, 24, 337
Shankar, F., Cavaliere, A., Cirasuolo, M., & Maraschi, L. 2008, ApJ, 676, 131

Shin, M.–S.; Ostriker, J.P., Ciotti, L. 2010, ApJ, arXiv1003.1108
Shull, J.M., Van Steenberg, M.E. 1985, ApJ, 294, 599
Smith, R.K., Brickhouse, N.S., Liedahl, D.A.; Raymond, J.C. 2001, ApJ, 556, 91
Spergel, D.N., et al. 2007, ApJS, 170, 377
Spinrad, H., Marr, J., Aguilar, L., Djorgovski, S. 1985, PASP, 97, 932
Strüder, L., Briel, U., Dennerl, K., et al., 2001, A&A, 365, 18
Tadhunter, C.N., Morganti, R., Robinson, A., Dickson, R., Villar-Martin, M., Fosbury, R.A.E. 1998, MNRAS, 298, 1035
Tadhunter, C. 2008, New Astronomy Reviews, 52, 227
Tarter, C., Tucker, W.H., and Salpeter, E. 1969, ApJ, 156, 943
Terashima, Y., & Wilson, A.S. 2003, ApJ, 583, 145
Torresi, E., Grandi, P., Guainazzi, M., Palumbo, G.G.C., Ponti, G., Bianchi, S. 2009, A&A, 498, 61
Torresi, E., Grandi, P., Longinotti, A. L., Guainazzi, M., Palumbo, G. G. C., Tombesi, F., Nucita, A. 2010, MNRAS, 401L, 10
Tremaine, S., et al. 2002, ApJ, 574, 740
Turner, A.K., Fabian, A.C., Lee, J.C., Vaughan, S. 2004, MNRAS, 353, 319
Turner, M.J.L., Abbey, A., Arnaud, M., Balasini, M., Barbera, M., Belsole, E., Bennie, P. J., Bernard, J. P., Bignami, G.F., et al. 2001, A&A, 365, 27
Urry M.C., Padovani P., 1995, PASP, 107, 803
Walker, R.C., Benson, J.M., Unwin, S.C. 1987, ApJ, 316, 546
Wamsteker, W., Wang, T.-G., Schartel, N., Vio, R. 1997, MNRAS, 288, 225
Willott, C.J., Rawlings, S., Blundell, K.M., & Lacy, M. 1999, MNRAS, 309, 1017
Wilson, A.S., Young, A.J., Shopbell, P.L. 2001, ASP Conference Series, Vol. 250, editors R.A. Laing & K.M. Blundell
Wu, W., Clayton, G.C.; Gordon, K.D., Misselt, K.A., Smith, T.L., Calzetti, D. 2002, ApJS, 143, 377
Yee, H.K.C., Oke, J.B. 1981, ApJ, 248, 472
Yaqoob, T., McKernan, B., Kraemer, S.B., et al. 2003, ApJ, 582, 105
Yaqoob, T, Padmanabhan, U. 2004, ApJ, 604, 63
Zeldovich, Ya.B. 1964, Soviet Physics – Doklady, 9, 195
Zdziarski, A.A., Grandi, P. 2001, ApJ, 551, 18
Zheng, W. 1996, AJ, 111, 1498

Publications

The following list reports the papers related to this thesis and written from the work made during the three years of Ph.D. They correspond to part of chapters1, 3 and 4 of this thesis.

1. "*3C 33: another case of photoionized soft X–ray emission in radio galaxies*"; **Torresi, E.**, Grandi, P., Guainazzi, M., Palumbo, G.G.C., Ponti, G., Bianchi, S. 2009, A&A, 498, 61

2. "*First high–resolution detection of a warm absorber in the Broad Line Radio Galaxy 3C 382*"; **Torresi, E.**, Grandi, P., Longinotti, A.L., Guainazzi, M., Palumbo, G.G.C., Tombesi, F., Nucita, A. 2010, MNRAS Letters, 401, 10

3. "*Warm Absorber energetics in Broad Line Radio Galaxies*"; **Torresi, E.**, Grandi, P., Costantini, E., Palumbo, G.G.C. 2011, submitted to MNRAS

4. "*Fermi Large Area Telescope observations of Misaligned AGN*"; Abdo et al. 2010, ApJ, 720, 912: Contact authors: P. Grandi, G. Malaguti, G. Tosti, C. Monte

5. "*Implications for the jet structure from multiwavelength observations of NGC 6251*"; Migliori, G., Grandi, P., **Torresi, E.**, Dermer, C., Finke, J., Celotti, A., Mukherjee, R., Errando, M., Gargano, F., Giordano, F., Giroletti, M. 2011, submitted to A&A